Dynamics of Seasonally-Varying Tropical Convergence Zones

Thesis by
Ho-Hsuan Wei

In Partial Fulfillment of the Requirements for the
Degree of
Doctor of Philosophy

CALIFORNIA INSTITUTE OF TECHNOLOGY
Pasadena, California

2018
Defended May 29, 2018

Ho-Hsuan Wei
ORCID: 0000-0002-6201-9810

ACKNOWLEDGEMENTS

First of all, I would like to thank my advisor Simona Bordoni. Simona is such a wonderful advisor and an amazing role model. She is caring, patient, intelligent, passionate, and empathetic. She has spent lots of time meeting with me, encouraged me when I met some difficulties in my research, and given me advice both in research and life. She also supports me to go to conferences and summer schools, which provides me chances to interact with many people. I really enjoy working with her and I learn a lot from her both on research and life. I am very lucky to have her as my advisor.

I also want to thank my committee members, Andy Thompson, Andy Ingersoll, Joao Teixeira, and Tapio Schneider. They provided many different suggestions and support during the past years. I especially want to thank Tapio for joining my committee in the last year. I also want to thank John Seinfeld for advising my second project in my first year and Chun-Chieh for leading me at the early stage of my research life before I came to Caltech.

During the time in Caltech, Simona's research group has always been one of the biggest supports. I want to thank Joan, Nicole, Salvatore, Spencer for being the reliable postdocs in the group and giving me many supports and pieces of advice. Jinqiang was my TA for multiple classes who taught me a lot and also shared with me lots of advice during my Ph.D. Jennifer and Anne, who are also my conference roommates, answered many of my research questions, even after they left Caltech. I also want to thank the younger group members, Ana, Katrina, and Siraput. It is very nice to have you in the last few years of my Ph.D.

In ESE (or Linde+Robinson), I want to thank many excellent students and postdocs throughout the years: Sally, Qiong, Robb, Toby, Zhihong, Da, Hank, Becky, Alex, Xiaozhou, Giuliana, Zach, Kyle, Colleen, Yair, Anna, Lenka, Andrew, Ayah, Georgy, Mar, Zhan, Yuanlong, Sang, Dan, John, Chanel, Liyin, and many more. I took classes with them, discussed research with them, joined different activities with them, had lunch with them, and/or shared the office with them. I would like to thank Toby especially. He met with me almost every time he came back for visit and gave me many comments on my work. I really enjoy discussing with him. I also want to thank Xiaozhou who discusses with me a lot and we always encourage each other. In the end, I want to thank Sally, who is the most important friend I made at

Caltech. She is there for almost all of my important events. She encourages me a lot, practices English with me, and comforts me when I am anxious. I really enjoy chatting with her while having lunch and walking back home together.

Besides people from the department, I also want to thank the friends I meet in the Association of Caltech Taiwanese. I enjoy going grocery shopping with them occasionally, while I can chat with different friends and learn different things from them. I also enjoy the events they hold in different holidays. I want to thank my previous roommate HwangFu, who supported me and made me feel warm when going home. I also want to thank the Taiwanese friends who play badminton with me almost every weekend. The volleybobo team, with people both from Caltech and from LA area, is one of the most important groups of friends during my time here. I really enjoy hanging out with you. Here I want to especially thank Yi-Chun. She gave me many suggestions before I came to Caltech, helped me a lot during my early phase of Ph.D., and became one of my closest friends since then.

I also have many friends studying similar fields in the US and back in Taiwan. We met in the conferences and talked through the internet. They have encouraged me, given me suggestions, and helped me with my research questions remotely. Thanks to DPF, Yi Lu, Chia-Ying, Jan-Huey, CYM, CHL, Bor-Ting, little Phy, snw, Ting-Chen, Yi-Hsuan, pumpkin, and many more. I especially want to thank CYM for chatting with me about my endless problems and Bor-Ting and little Phy for giving me many supports near the end of my Ph.D.

I want to thank all of my family members, who support me from Taiwan. Special thanks go to my older uncle and grandmom. I miss you. I want to thank my sister and brother, who are there for me and accompany my parents back home. I also want to thank my parents-in-law and sister-in-law, who always care a lot about our health and happiness. Most importantly, I would like to thank my parents. They are always there supporting me. I really cannot be here without them.

In the end, I would like to thank my husband, Chia-Wei. In order to spend time with me, he drove between Pasadena and Irvine for around 70000 miles during the past six years (with terrible traffic). He is the one who supports me when I am extremely depressed and anxious and the one who shares my happiness with me. I cannot do this without him.

ABSTRACT

In the tropics, rain tends to be organized along concentrated rain bands, with the Intertropical Convergence Zone (ITCZ) over the ocean and monsoonal convergence zones over tropical land masses being particularly prominent features affecting hundreds of millions of people. What fundamentally controls the spatial and temporal distribution of these tropical rainbands remains an outstanding question in the literature. This thesis aims to enhance our understanding of the dynamics of seasonally migrating convergence zones over the ocean and in the South Asian monsoon region.

First, we explore to what extent energetic arguments that have provided insight into the position and shifts of the annual and zonal mean ITCZ can also be applied on shorter timescales. Idealized aquaplanet simulations show that the energy flux equator (EFE) always leads the ITCZ, leading to a breakdown of the commonly assumed anti-correlation between the ITCZ position and the cross-equatorial energy transport. At times during which the EFE and the ITCZ reside on opposite sides of the equator, the required energy transport is in fact achieved by the Hadley cell, in which the ITCZ is embedded, changing its vertical structure into one of negative gross moist stability. One way in which this is accomplished is through the development of a shallow return flow at levels near minimum moist static energy. While the relationship between the EFE and the ITCZ in the observed seasonal cycle is more complex than what is seen in the idealized simulations, the development of bottom-heavy circulations is a common feature both in the zonal mean and in individual longitudinal sectors at times when the EFE and the ITCZ are in opposite hemispheres.

In the last chapter of this thesis, we explore changes in the South Asian monsoon as topography over Africa is removed in the full-physics GFDL AM2.1 GCM. Against expectations, the removal of the African topography is accompanied by a strengthening of the precipitation over India despite a weakening of the Somali jet. This counter-intuitive precipitation increase is associated with the development of a lower-level cyclonic wind anomaly, and associated meridional moisture flux convergence, over the Indian peninsula. Potential vorticity (PV) budget analyses following air parcel trajectories show that this cyclonic anomaly arises because, in the absence of the blocking effect of the African topography, air particles that reach the Arabian Sea originate at higher latitude and hence have a higher background planetary vorticity.

PUBLISHED CONTENT AND CONTRIBUTIONS

Ho-Hsuan Wei and Simona Bordoni (2016), On the Role of the African Topography in the South Asian Monsoon. *Journal of the Atmospheric Sciences*, 73(8): 3197–3212. DOI: 10.1175/JAS-D-15-0182.1 ©American Meteorological Society. Used with permission.

Both authors participated in the conception of the project and the writing of the manuscript. Ho-Hsuan Wei conducted simulations and analyzed the data.

Ho-Hsuan Wei and Simona Bordoni (2018), Energetic Constraints on the ITCZ Position in Idealized Simulations with a Seasonal Cycle. *Journal of Advances in Modeling Earth Systems*. Accepted Author Manuscript. DOI: 10.1029/2018MS001313

Both authors participated in the conception of the project and the writing of the manuscript. Ho-Hsuan Wei conducted simulations and analyzed the data.

Aiko Voigt, Michela Biasutti, Jacob Scheff, Jürgen Bader, Simona Bordoni, Francis Codron, Ross D Dixon, Jeffrey Jonas, Sarah M Kang, Nicholas P Klingaman, Ruby Leung, Jian Lu, Brian Mapes, Elizabeth A Maroon, Sonali McDermid, Jong-yeon Park, Romain Roehrig, Brian E J Rose, Gary L Russell, Jeongbin Seo, Thomas Toniazzo, Ho-Hsuan Wei, Masakazu Yoshimori, and Lucas R Vargas Zeppetello (2016), The tropical rain belts with an annual cycle and a continent model intercomparison project: TRACMIP. *Journal of Advances in Modeling Earth Systems*, 8, 1868–1891. DOI: 10.1002/2016MS000748

Ho-Hsuan Wei conducted the perturbed simulations with the gray radiation model ("CALTECH").

TABLE OF CONTENTS

LIST OF ILLUSTRATIONS

Number *Page*

LIST OF TABLES

Chapter 1

INTRODUCTION

Motivation

Most of the Earth's precipitation falls in the tropics, the latitudinal band within 30 degrees north and south of the equator. Mechanisms controlling the spatial and temporal distribution of large-scale tropical rain bands, including the oceanic intertropical convergence zone (ITCZ) and its excursions into summer tropical continents in association with monsoons, remain an open question and a major challenge for the climate sciences. Tropical and subtropical regions, with increasing populations and rapidly growing economies, heavily rely on rainfall and are extremely susceptible to rainfall changes under global warming. Yet, predictions remain highly uncertain on all timescales, emphasizing the need for improved understanding.

In the past decade, significant advances have been made in our theoretical understanding of controls on tropical precipitation. An emerging framework has emphasized the atmospheric energy balance as possibly more fundamental than the traditional surface energetic perspective to understand how the zonally-averaged ITCZ responds to radiative and surface flux perturbations. In particular, this framework allows for the explanation of shifts in the ITCZ position in response to higher latitude thermal forcing as part of the anomalous meridional energy flux needed to restore energy balance, without the need to invoke changes in tropical SSTs. More specifically, for an hemispherically asymmetric energetic perturbation in the extratropics (for instance arising from changes in surface albedo, clouds and aerosols), the atmospheric general circulation will restore energy balance by transporting energy from the hemisphere with net energy input to the hemisphere with net energy deficit, resulting in a non-zero cross-equatorial energy transport (e.g., Frierson and Hwang, 2012; Hwang et al., 2013; Kang et al., 2009, 2008). Given that in the tropics most of the energy transport is effected by the Hadley circulation, the required anomalous cross-equatorial energy transport will be accomplished through shifts in the Hadley cell's ascending branch and ITCZ in the relatively warmed hemisphere, under the assumption that the effective energy stratification remains positive.

While these energetic arguments have been shown to provide important insight into the response of the annual and zonal mean ITCZ (e.g., Bischoff and Schneider, 2014;

Donohoe et al., 2013; Frierson and Hwang, 2012; Hwang et al., 2013; Kang et al., 2009, 2008), relatively little work has explored their implications on timescales shorter than seasonal (e.g., Adam et al., 2016a,b; Chiang and Friedman, 2012; Donohoe et al., 2013). This dissertation work tries to fill this existing gap in the literature by exploring the applicability of the energetic framework to seasonal ITCZ migrations. We begin by performing and analyzing idealized aquaplanet simulations that lack any zonal asymmetry, as they allow for the study of fundamental mechanisms in a model of minimal complexity (Chapter 2). The relevance of these mechanisms is then explored in observations with reanalysis data (Chapter 3).

Understanding seasonal excursions of the zonal mean ITCZ, however, does not reveal the full complexity of tropical precipitation variability. In fact, tropical precipitation is highly zonally asymmetric. While for instance, seasonal variations over the oceanic regions are quite muted both in precipitation intensity and location, they are much more dramatic over tropical continents, where rain bands can migrate up to $15-20$ degrees from the equator into the summer hemisphere (e.g., Schneider et al., 2014; Waliser and Gautier, 1993). It is now understood that these seasonal migrations of tropical convergence zones into the summertime tropical continents are associated with the development of monsoonal circulations in those regions. Monsoonal circulations have been progressively understood as zonally localized energetically-direct cross-equatorial Hadley circulations (e.g., Bordoni and Schneider, 2008; Gadgil, 2003), rather than sea breeze circulations driven by land-sea thermal contrast (e.g., Meehl, 1994; Webster, 1987; Wu et al., 2012). The extent to which energetic constraints that hold true for the annually and zonally averaged ITCZ can also hold true for the zonally localized monsoonal convergence zones remains an area of active research (e.g., Adam et al., 2016b).

Among all Earth's monsoons, the South Asian monsoon (SAM) is the largest and most dramatic one, bringing concentrated summer precipitation to densely populated regions, such as India and neighboring countries. The associated energetically-direct overturning circulation is characterized by an ascending branch over the subtropical continent, opposite cross-equatorial flows at upper and lower levels, and descending motion into the winter hemisphere, with a reversed meridional temperature gradient and easterly wind shear in the summer hemisphere (e.g., Bordoni and Schneider, 2008; Gadgil, 2003; Nie et al., 2010). At lower levels, westerly winds dominate over the Indian ocean, consistent with the Coriolis force on the northward flow in the Somali jet approximately balancing drag on the near-surface zonal winds. Upstream

of the lower-level westerlies over India in the summer, a strong cross-equatorial jet, known as the Somali jet, flows along the East African Highlands (EAHs) and turns eastward in the Arabian Sea (e.g., Findlater, 1969). The jet brings into the Indian subcontinent moisture from the warm ocean, with around $60 - 80\%$ of the moisture estimated to originate from the SH (e.g., Hoskins and Rodwell, 1995). The strong precipitation, the reversal of lower-level winds from easterly to westerly over the Indian Ocean in the NH, and the Somali jet are all distinctive features of the SAM in boreal summer.

Surrounding the SAM system, dramatic topographical features including the Himalayas, the Tibetan Plateau (TP), and the EAHs are all considered to have fundamental influences on the dynamic and thermodynamic properties of the monsoon. Understanding the mechanisms by which topography impacts the SAM provides a theoretical framework to link past monsoonal evolution to the topographical history on geological timescales (e.g., An et al., 2001; Molnar et al., 2010), to explain biases in climate model simulations (e.g., Boos and Hurley, 2013), and to better interpret past and future monsoon responses to changing climate, such as those driven by albedo changes with snowpack changes (e.g., Blanford et al., 1884; Boos and Kuang, 2010). Within a rich body of literature investigating the role of topography in the SAM, earlier work emphasized the importance of the TP as a major driver of the SAM, primarily through its elevated heating (e.g., Flohn, 1957; Molnar et al., 1993; Yeh et al., 1957). In this view, surface heat fluxes over the TP drive rising motion that draws air towards the mountains, converging moisture, which then condenses and releases latent heat in a positive feedback (e.g., Wu et al., 1997, 2012). Recent work, however, suggests that topography over Asia might support the development of a strong SAM by acting more as a thermal insulator, separating the warm and moist tropics from the cold and dry extratropics, than as a thermal heat source (e.g., Boos and Kuang, 2010, 2013; Privé and Plumb, 2007b).

While located significantly upstream of the SAM core, the EAHs have also been argued to be important for the dynamical structure of the monsoonal circulation, primarily by helping to spatially concentrate and strengthen the cross-equatorial flow in the Somali jet (e.g., Anderson, 1976; Krishnamurti et al., 1976; Paegle and Geisler, 1986; Rodwell and Hoskins, 1995; Sashegyi and Geisler, 1987). Explained by the possible impact of the Somali jet on the SAM precipitation through the associated moisture transport, some early observational studies show a positive correlation between the strength of the Somali jet and the rainfall intensity over

western India (e.g., Findlater, 1969; Halpern and Woiceshyn, 2001). However, recent modeling studies show that the removal of the African topography in fact results in an increase rather than a decrease of the monsoonal precipitation over India, despite a weakening of the Somali jet (e.g., Chakraborty et al., 2002, 2006, 2009; Slingo et al., 2005). These studies highlight that the fundamental dynamics of the jet remains debated, as does its relation to the SAM precipitation. Given the importance of the Somali jet to the overall monsoonal circulation and precipitation, in Chapter 4, we investigate in a full physics GCM the counter-intuitive precipitation response to the removal of African topography.

Theories and predictors of tropical precipitation

Different classes of theories exist for understanding tropical precipitation. In general, tropical precipitation over tropical oceans has been shown to be closely related to the sea surface temperature distribution. Two main theories have been developed to understand the quasi-steady oceanic tropical precipitation, given the sea surface temperature (SST) distribution. In one view, the planetary boundary layer (PBL) momentum dynamics is the key, as it determines the BL lower-level wind convergence, and with it moisture convergence, and hence convection. The BL moisture convergence maximizes where the Laplacian of the near-surface temperature is the most negative (i.e., maximum of -1×(surface temperature Laplacian)) (e.g., Lindzen and Nigam, 1987; Sobel, 2007; Waliser and Somerville, 1994).

In the other view, tropical precipitation is thermodynamically controlled and can be determined independently of the BL momentum budget. In this view, tropical convection is related to CAPE (convective available potential energy), which is primarily determined by the near surface moist static energy distribution, as temperature gradients in the tropical free troposphere are constrained to be weak (e.g., Sobel et al., 2001). Hence, tropical precipitation tends to occur over tropical SST and MSE maxima (e.g., Neelin and Held, 1987; Sobel, 2007).

A significant body of work has explored if and to what extent one of these two classes of theories provides superior predictions of tropical precipitation (e.g., Back and Bretherton, 2006, 2009a,b; Sobel and Neelin, 2006). More specifically, while in general the global SST maximum also corresponds to the region of largest negative temperature Laplacian, there are regions with local, rather that global SST maxima, that still have strong negative Laplacian of the SST and can sustain precipitation through BL lower-level convergence. The relative importance of thermodynamic

and dynamic controls on tropical precipitation might also explain the vertical structure of resulting ascending motion, with bottom-heavy profiles being more favored in regions of strong BL lower-level convergence and weak SST (e.g., Back and Bretherton, 2009a; Lindzen and Nigam, 1987; Sobel, 2007).

While theories are usually developed using simple or minimal models, the response of tropical precipitation to radiative or other perturbations in more complex climate models or observations is usually explored using large-scale budgets that can provide insight into mechanisms of change. One of the most common and direct ways to diagnose precipitation is through the moisture budget, which, for negligible storage, links the net precipitation (P-E) to the vertically integrated moisture flux converging into an atmospheric column, which is also called P−E budget (e.g., Clement et al., 2004; Held and Soden, 2006; Merlis et al., 2013; Walker et al., 2015). In chapter 4, we use this moisture budget to analyze the precipitation response to the removal of the African topography.

As mentioned above, one framework that has been extensively used in the past decade and that has allowed for significant progress in the understanding of ITCZ and monsoon dynamics is the atmospheric energy or moist static energy (MSE) budget (e.g., Chen and Bordoni, 2014; Chou and Neelin, 2003; Chou et al., 2001; Hill et al., 2015; Merlis et al., 2012a,b; Neelin, 1997; Neelin and Zeng, 2000). The MSE budget can be derived from the vertically integrated temperature and moisture equation (Neelin and Zeng, 2000; Sobel and Bretherton, 2000), which expressed in units of energy are:

$$C_p \frac{\partial \langle \overline{T} \rangle}{\partial t} + C_p \langle \overline{\mathbf{u} \cdot \nabla T} \rangle + \langle \overline{\omega \frac{\partial s}{\partial p}} \rangle = \langle \overline{Q_c} \rangle + \overline{\mathcal{S}^{net}} + \overline{\mathcal{L}^{net}} + \overline{SH}, \tag{1.1}$$

and

$$L_v \frac{\partial \langle \overline{q} \rangle}{\partial t} + L_v \langle \overline{\mathbf{u} \cdot \nabla q} \rangle + L_v \langle \overline{\omega \frac{\partial q}{\partial p}} \rangle = \langle \overline{Q_q} \rangle + \overline{LH}, \tag{1.2}$$

where $\langle \cdot \rangle$ represents a mass-weighted vertical integral [i.e., $\int (\cdot) dp/g$], $\overline{(\cdot)}$ a time-mean, $s = C_p T + gz$ is dry static energy, $\mathbf{u}$ the horizontal wind velocity, and ω the pressure vertical velocity. The Lagrangian tendency of vertically integrated internal energy and work on the left hand side of the equation is balanced by the energy input which includes the net shortwave radiation ($\mathcal{S}^{net}$, net downward shortwave radiation at the top of atmosphere (TOA), $\mathcal{S}^t$, minus that at the surface, $\mathcal{S}^s$), the net longwave radiation ($\mathcal{L}^{net}$, net upward longwave radiation at the surface, $\mathcal{L}^s$, minus that at the TOA, $\mathcal{L}^t$), the sensible heat flux at the surface (SH), and the condensational

heating within the air column ($\langle Q_c \rangle = L_v P$). The Lagrangian tendency of moisture in the atmospheric column is balanced by surface evaporation (LH, latent heat flux) and convective moisture source, whose vertical integral needs to balance the condensational heating ($\langle Q_q \rangle = -L_v P = -\langle Q_c \rangle$). When the vertically integrated thermodynamic and moisture equations are summed, one obtains the MSE budget

$$\frac{\partial \langle \overline{E} \rangle}{\partial t} = -\langle \overline{\mathbf{u} \cdot \nabla E} \rangle - \langle \overline{\omega \partial_p h} \rangle + \overline{NEI}, \tag{1.3}$$

where $E = C_p T + L_v q$ is the atmospheric moist enthalpy, $h = C_p T + L_v q + gz$ the MSE, and NEI (net energy input) = $\mathcal{S}^{net} + \mathcal{L}^{net} + SH + LH$, the net energy flux into the atmospheric column from radiative fluxes at the TOA and radiative and enthalpy fluxes at the surface. One of the advantages of the MSE budget is that it sidesteps the large but canceling terms that occur in the individual temperature and moisture equations, and relates atmospheric motions to sources and sinks of energy through the top and bottom of an atmospheric column.

In the deep tropics, where free tropospheric temperature gradients are constrained to be weak, the dominant balance is usually between the NEI and MSE vertical advection. To the extent that most of the vertical advection is accomplished by the mean flow and that the h is positively stratified (that is, $\partial_p h$ is negative), positive NEI will be balanced by export of MSE through the development of ascending motion (e.g., Neelin, 2007).

By further assuming that vertical motions have a dominant vertical structure $\Omega(p)$ (that is, a first baroclinic structure), the total vertical velocity $\omega(x, y, p, t)$ can be decomposed as $\Omega(p)\hat{\omega}(x, y, t)$, with $\hat{\omega}(x, y, t)$ representing spatial variations of the first baroclinic mode. The MSE equation then reduces to $\overline{NEI} \approx -\frac{p_T}{g}\hat{\omega}\overline{M}$, where M is the gross moist stability (GMS), defined as $-\frac{g}{p_T}\langle \Omega \partial_p h \rangle$, and P_T is the depth of troposphere (e.g., Neelin, 1997; Neelin and Held, 1987; Sobel, 2007).

The GMS represents the efficiency of vertically-averaged MSE divergence of the atmospheric column per unit mass convergence at lower level. For deep convection, the GMS is usually positive with convection exporting MSE out of the atmospheric column. For a given positive NEI and positive GMS, the larger the GMS the more efficient is the energy export per mass import. While this relation has been shown to provide the basis for theories of tropical precipitation, the GMS is a hard quantity to constrain and to understand from a theoretical perspective, and it has been shown to be very sensitive to both the Ω profile and the vertical MSE structure (e.g., Sobel, 2007). For example, it is shown that the GMS tends to be negative in the Eastern

Pacific, in association with the development of shallow or bottom-heavy convection (e.g., Back and Bretherton, 2006; Zhang et al., 2004). This suggests the limitation of assuming that vertical motions in the tropics have everywhere a first baroclinic mode structure. Additionally, in the Eastern Pacific, shallow vertical motions with negative GMZ import rather than export MSE.

While it is generally true that in deep convective regions the dominant balance in the MSE budget is between NEI and vertical MSE advection, it is now well recognized that horizontal advection can play an important role in shaping tropical and subtropical precipitation. Horizontal moist enthalpy advection has for instance been shown to be critical in setting the poleward extent of monsoonal convergence zones over subtropical land masses (Chou and Neelin, 2003; Chou et al., 2001) and in maintaining the meiyu-baiu front in a region of otherwise net energy input (Chen and Bordoni, 2014).

The MSE equation has also been used extensively to provide constraints on the zonally averaged ITCZ (e.g., Bischoff and Schneider, 2014; Frierson and Hwang, 2012; Hwang et al., 2013; Kang et al., 2009, 2008). In the zonal mean, the MSE equation can be written as:

$$\frac{\partial \langle [\overline{E}] \rangle}{\partial t} = -[\partial_y \langle \overline{vh} \rangle] + [\overline{NEI}], \tag{1.4}$$

where the $[\cdot]$ represents a zonal mean. By integrating meridionally Eq. (1.4) from the south pole (SP, where the energy flux goes to zero), the MSE flux at any given latitude ϕ is given by:

$$\langle [vh] \rangle_\phi = \frac{1}{cos\phi} \int_{SP}^{\phi} [\mathrm{NEI_{eff}}] a cos\phi d\phi, \tag{1.5}$$

where a is the radius of the Earth and $\mathrm{NEI_{eff}}$ (effective NEI) = NEI - storage. A cross-equatorial energy flux is therefore required to maintain energy balance if $\mathrm{NEI_{eff}}$ is hemispherically asymmetric.

Under the assumptions that the energy transport in the tropics is primarily accomplished by the Hadley circulation and that MSE is positively stratified (that is, GMS in the Hadley cell, defined here as GMS $= \int_0^{p_s} \overline{vh} \frac{dp}{g} / \int_0^{p_m} \overline{v} \frac{dp}{g}$, where p_m is the pressure at maximum streamfunction (e.g., Feldl et al., 2017; Frierson, 2007; Hill et al., 2015; Kang et al., 2009), is positive), the Hadley cell's ascending branch, and with it the ITCZ, will be located in the hemisphere with net energy input, so as to transport energy across the equator to the hemisphere with net energy loss. Under

these assumptions, the ITCZ will be approximately colocated with the energy flux equator, that is the latitude at which the MSE flux vanishes. We will explore to what extent these energetic arguments provide useful constraints on seasonal ITCZ migrations in Chapter 3.

While falling short of providing closed theories for tropical precipitation, these budgets provide insight into mechanisms controlling its position and response to perturbations on different time scales. Hence, they will be used extensively throughout this dissertation.

Chapter 2

ENERGETIC CONSTRAINTS ON THE ITCZ POSITION IN SIMULATIONS WITH A SEASONAL CYCLE

Ho-Hsuan Wei and Simona Bordoni (2018), Energetic Constraints on the ITCZ Position in Idealized Simulations with a Seasonal Cycle. *Journal of Advances in Modeling Earth Systems*. Accepted Author Manuscript. DOI: 10.1029/2018MS001313

Abstract

The atmospheric energy budget has recently been shown to provide powerful constraints on the position and shifts of the zonal and annual mean intertropical convergence zone (ITCZ), which lies close to the latitude of zero vertically integrated energy transport (energy flux equator, EFE). Relatively little work has however explored the applicability of the energetic framework to ITCZ shifts on shorter timescales. This study investigates to what extent the EFE tracks the ITCZ on subseasonal timescales in idealized aquaplanet simulations with different mixed layer depths. It is shown that the ITCZ always lags the EFE, even in the simulation with the shallowest mixed layer depth, making it possible for the EFE and the ITCZ to reside on opposite sides of the equator. At these times, which occur as the winter cross-equatorial Hadley circulation retreats from the summer hemisphere, the required energy balance is achieved not through shifts of the Hadley cell's ascending branch and ITCZ to track the EFE but through changes in the cell's vertical structure into one of negative gross moist stability (GMS). For any given position of the ascending branch, the winter cell is much weaker as it retreats from than as it expands into the summer hemisphere and develops a shallow return flow at mid-to-lower tropospheric levels where the moist static energy reaches its minimum, hence favoring a negative GMS. It is argued that the asymmetry between the expanding and retreating phases of the winter Hadley cell is linked to the nonlinear seasonal evolution of near-surface temperatures.

2.1 Introduction

The most intense rainfall over the Earth's surface occurs within the intertropical convergence zone (ITCZ), a zonally elongated band of moist convection and low-

level wind convergence over near-equatorial regions. In its annual and zonal mean, the ITCZ is located at around 6°N in present-day climate, with seasonal migrations characterized by a more northward (southward) position in boreal (austral) summer (e.g., Adler et al., 2003; Waliser and Gautier, 1993). Such asymmetry cannot arise from the insolation forcing, which is essentially symmetric about the equator. Hence, other asymmetries in the climate system must be responsible for the northward position of the ITCZ, such as possibly the coastline orientation of the Americas and feedbacks between resulting SST patterns and low clouds (e.g., Philander et al., 1996), and the presence of the Andes (e.g., Takahashi and Battisti, 2007). Which asymmetry is the most relevant one remains a topic of active research, but consensus is emerging that the ocean meridional overturning circulation significantly contributes to the hemispheric asymmetry in tropical rainfall by transporting energy from the southern to the northern hemisphere (NH) (e.g., Frierson et al., 2013; Marshall et al., 2013).

Traditional theories have historically linked the ITCZ to tropical SSTs and associated gradients (e.g., Lindzen and Nigam, 1987; Sobel, 2007). However, modeling studies (e.g., Broccoli et al., 2006; Chiang et al., 2003; Vellinga and Wood, 2002; Yoshimori and Broccoli, 2008; Zhang and Delworth, 2005) and paleoevidence (e.g., Arbuszewski et al., 2013; Haug, 2001; Lea, 2003) suggest that the ITCZ responds strongly to extratropical thermal forcing, shifting into (away from) the relatively warmed (cooled) hemisphere. In the past decade, the vertically integrated atmospheric energy budget has provided the theoretical framework to understand the ITCZ response to remote forcing as part of the anomalous meridional energy fluxes needed to restore energy balance (e.g., Donohoe et al., 2013; Frierson and Hwang, 2012; Kang et al., 2009, 2008).

This framework has emphasized the anti-correlation between the ITCZ position and the cross-equatorial atmospheric energy transport and has led to the introduction of the energy flux equator (EFE, the latitude at which the meridional energy transport vanishes) as a diagnostic for the ITCZ (Kang et al., 2008). Central to these arguments is the assumption that in the tropics energy and moisture transports are primarily accomplished by the Hadley circulation and that energy is transported in the direction of the Hadley cell's upper branch. Therefore, a northward (southward) shift of the ITCZ is associated with anomalous southward (northward) energy transport across the equator. The anti-correlation between the ITCZ and the cross-equatorial energy transport has been shown to be robust across observational data (e.g., Mcgee et al.,

2014) and model experiments, with the ITCZ position being directly influenced by energetic perturbations (such as those associated with changes in ice albedo, clouds and aerosols) in the extratropics (e.g., Frierson and Hwang, 2012; Hwang et al., 2013; Kang et al., 2009, 2008).

Factors controlling the sensitivity of the ITCZ position to the cross-equatorial energy transport are more directly quantified in Bischoff and Schneider (2014), who show how this sensitivity depends on the net energy input (NEI) into the equatorial atmosphere, that is, the net radiative fluxes at the top of atmosphere (TOA) minus any energy that is being uptaken by the ocean. This work emphasizes how changes in NEI near the equator can cause shifts in the ITCZ even without any change in cross-equatorial energy transport. Changes in NEI for instance explain the equatorward shift of the ITCZ during El Niño years.

While these energetic constraints have been shown to provide insight into the dynamics of annual and zonal mean ITCZ shifts, relatively little work has explored their implications on shorter timescales (e.g., subseasonal) (e.g., Adam et al., 2016a,b; Chiang and Friedman, 2012; Donohoe et al., 2013). Adam et al. (2016a) use reanalysis data to show how the zonal mean EFE and the ITCZ position covary on timescales of seasons and longer. Interestingly, a lag between the EFE and the ITCZ exists, especially as the ITCZ moves from the northern to the southern hemisphere (SH). This lag is also seen in sector-mean quantities over most ocean basins (Adam et al., 2016b). That is, there are times during the seasonal cycle when the EFE and the ITCZ can be on opposite sides of the equator and, hence, the vertically integrated energy transport and the mass transport in the upper branch of the Hadley circulation have opposite signs. These results therefore suggest limitations of the energetic perspective when considering ITCZ migrations on timescales shorter than seasonal and warrant further investigation.

This is indeed the scope of this paper. In particular, we want to address the following questions: 1) To what extent does the EFE track the ITCZ location on timescales shorter than seasonal? 2) Does a lag exist between these two quantities and, if so, how is this lag influenced by the heat capacity of the underlying ocean surface? 3) What are the implications of oppositely-signed energy and mass transport (or negative gross moist stability) for the atmospheric tropical circulation? To highlight fundamental mechanisms in a model of minimal complexity and advance conceptual understanding, we will address these questions in idealized aquaplanet simulations that lack any zonal asymmetry.

The model and experimental design are described in Section 2. In Section 3, we discuss energetic constraints on the ITCZ position for summertime averages. ITCZ seasonal migrations and their relation to the cross-equatorial energy transport and the EFE are presented in Section 4. There, possible mechanisms for the breakdown of commonly discussed relationships between the ITCZ, the EFE and the cross-equatorial energy transport are also discussed. We conclude in Section 5 with a discussion and summary of our results.

2.2 Methods

Model and experimental design

We use an idealized GCM, which builds on the model of Frierson et al. (2006), Frierson et al. (2007), and O'Gorman and Schneider (2008) and has been used in many studies of tropical and extratropical large-scale circulations (e.g., Bordoni and Schneider, 2008; Kaspi and Schneider, 2013; Merlis et al., 2013). The model is a primitive equation model of an ideal-gas atmosphere built on the Geophysical Fluid Dynamics Laboratory (GFDL) Flexible Modeling System (FMS). The primitive equations are solved spectrally at T42 horizontal resolution with 30 uneven sigma levels in the vertical. The radiation scheme is a two-stream radiative transfer scheme with gray atmosphere and prescribed optical thickness in longwave radiation. The GCM contains idealized representations of the effects of latent heat release on the dynamics, through a grid-scale condensation scheme and a quasi-equilibrium convection scheme (Frierson, 2007). Once liquid water is formed, it is immediately precipitated out, hence there is no representation of clouds and cloud radiative feedback. Similarly, the prescribed optical depth in the radiation scheme is decoupled from the specific humidity, hence there is no interactive water vapor feedback. The lower boundary consists of a uniform slab ocean of constant mixed layer depth. The idealized treatment of the physics and the idealized settings allow us to study the fundamental interaction between larger-scale circulations and moist convection in the absence of many complex and poorly constrained feedbacks, such as clouds.

Unlike previous studies of ITCZ dynamics using the same GCM (e.g., Bischoff and Schneider, 2014), here we perform simulations with a seasonal cycle of insolation with 360 days but no diurnal cycle. Orbital parameters are chosen to a near-contemporary obliquity of 23.5° and zero eccentricity. We choose a uniform mixed layer depth of 20 meters, as representative of oceanic thermal inertias (Aqua20m). Sensitivity to the slab ocean depth is explored by conducting experiments with 10 meter (Aqua10m) and 0.2 meter (Aqua0.2m) mixed layer depths. All simulations are

started from an equilibrated equinoctial state, and then integrated for 25 simulated years. Results are averaged over the last 15 simulated years. All statistics (including eddy fluxes) are computed from 6-hourly outputs and averaged at pentad (5 days) temporal resolution.

ITCZ and energetic diagnostics

In its most basic definition, the ITCZ is the locus of maximal tropical precipitation, $\phi_{P_{max}}$. When applied to any precipitation field (either from model outputs or observations), this ITCZ indicator has two limitations. First, given that $\phi_{P_{max}}$ is constrained by the horizontal resolution of the precipitation field, tracking seasonal migrations of the ITCZ using this indicator might introduce artificial discontinuities. Additionally, for situations where tropical precipitation features more than one peak, as commonly seen in both observations and model simulations (e.g., Lin, 2007; Zhang, 2001), seasonal precipitation redistributions between these peaks can introduce jumps or discontinuities in otherwise smooth precipitation changes.

Other ITCZ indices have therefore been introduced in the literature, such as the precipitation centroid of Frierson and Hwang (2012). More generally, Adam et al. (2016a) derive different ITCZ metrics using an integer power N of the area-weighted tropical precipitation:

$$\phi_{P_{max,smth}} = \frac{\int_{\phi_1}^{\phi_2} \phi[cos\phi P]^N d\phi}{\int_{\phi_1}^{\phi_2} [cos\phi P]^N d\phi}, \tag{2.1}$$

where P is the precipitation and ϕ the latitude. While N = 1 is the precipitation centroid, here we use N = 10, which, as discussed in Adam et al. (2016a), provides estimates of the ITCZ latitude that are close to the actual precipitation maximum but smooth out discretization issues. The integration boundaries ϕ_1 and ϕ_2 are chosen to cover the latitudinal span of tropical rainbands.

No single ITCZ indicator based on precipitation performs uniformly well across our simulations, which show a wide range of ITCZ structures, ranging from a well-defined single ITCZ in the Aqua20m case to a double ITCZ in the Aqua0.2m case, where a near-equatorial secondary precipitation maximum exists in the summer hemisphere during the warm seasons in addition to the seasonally moving convergence zone associated with the ascending branch of the Hadley cell (Fig. 4.1). More specifically, while $\phi_{P_{max,smth}}$ faithfully tracks the precipitation maximum in the Aqua20m single ITCZ, its relation to the seasonally migrating convergence zone in

the more extreme Aqua0.2m case is dubious (Fig. 2.1d). For these reasons, while the ITCZ location ($\phi_{P_{ITCZ}}$) is identified as $\phi_{P_{max,smth}}$ in Aqua20m, in Aqua10m and Aqua0.2m we identify it as the latitude of the poleward precipitation peak ($\phi_{P_{max}}$) even at those few pentads during the seasonal cycle when the near-equatorial convergence zone has higher precipitation.

Given that the ITCZ is associated with the ascending branch of the tropical overturning circulation, it is also of interest to compare the ITCZ location with the dividing boundary between the two Hadley cells, that is the latitude where the meridional mass streamfunction vanishes ($\phi_{\psi=0}$). In the annual average or around the equinoxes, when the tropical overturning circulation is characterized by two cells that are almost symmetric about the equator, the ITCZ and the latitude at which the meridional mass streamfunction changes sign are expected to be collocated. Around solstices, however, when this equinoctial pattern is replaced by a solstitial pattern characterized by a strong, cross-equatorial winter cell and a much weaker, or negligible, summer cell, $\phi_{\psi=0}$ more clearly identifies the poleward boundary in the summer hemisphere of the winter cell (e.g., Privé and Plumb, 2007a) and becomes progressively separated from the ITCZ, which is located equatorward of it (e.g., Lindzen and Hou, 1988). This is because precipitation is more directly linked to the region of strongest vertical velocity, and hence of maximal meridional gradient of the massflux streamfunction, which does not always coincide with the boundary between the two Hadley cells. We diagnose $\phi_{\psi=0}$ as the latitude at which the massflux streamfunction reaches 5% of its maximum value, at the level of this maximum. This definition works well even when the circulation is dominated by the winter cell, with a negligible summer cell, and thus the boundary between the two Hadley cells become less well defined and cannot be diagnosed from a change in sign of the streamfunction (e.g., Faulk et al., 2017; Walker and Schneider, 2005).

Finally, we use the energy flux equator (EFE), which, as discussed in the introduction, has been shown to be a good predictor of the ITCZ and its response to perturbations for annual and zonal averages. The ϕ_{EFE} is defined as the latitude at which the vertically integrated meridional moist static energy (MSE) flux goes to zero:

$$\langle \overline{vh} \rangle_{\phi_{EFE}} = 0, \tag{2.2}$$

where $\langle \cdot \rangle = \int_0^{p_s} (\cdot) dp/g$ is a mass-weighted vertical average, $\overline{(\cdot)}$ represents time and zonal mean, and $h = C_p T + L_v q + gz$ is MSE. Assuming that the energy transport in the tropics is primarily effected by the Hadley circulation, the zero of the massflux

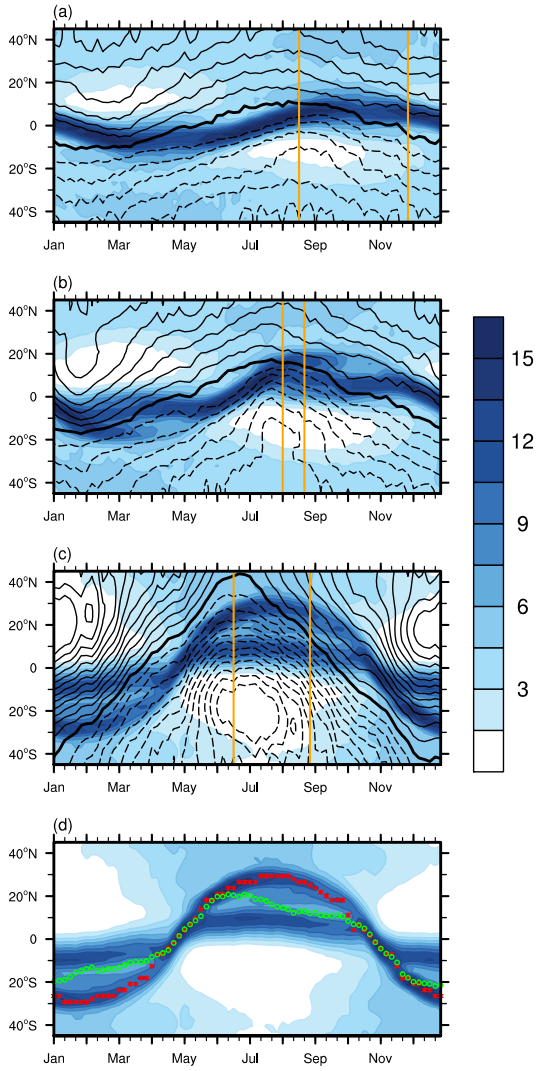

Figure 2.1: Seasonal evolution of zonal mean precipitation (shading, mm day^{-1}) and vertically integrated meridional energy flux (contours) in (a) Aqua20m, (b) Aqua10m, and (c) Aqua0.2m. The contour spacing is 2.5×10^7 W m^{-1} with solid contours for positive values, dashed contours for negative values, and thick contour for zero transport (EFE). Vertical orange lines indicate the time period during which the ITCZ ($\phi_{P_{ITCZ}}$) is poleward of 85% of its maximum excursion, which we use to construct summertime means in Figs. 2.2 and 2.3. (d) Seasonal cycle of zonal mean precipitation in the Aqua0.2m simulation, as in (c). Red asterisks show $\phi_{P_{max}}$ and the green open circles $\phi_{P_{max,smth}}$. The integration boundaries ϕ_1 and ϕ_2 to calculate $\phi_{P_{max,smth}}$ (Eq. (2.1)) are chosen as 35°S and 35°N for all three simulations, to account for the more extreme off-equatorial ITCZ excursions in the Aqua0.2m simulation.

streamfunction, which is expected to covary with the ITCZ, will also be where the energy flux vanishes. In addition to diagnosing the location of the EFE directly

from our simulations as the latitude where the energy flux goes to zero (which in the following we will denote as $\phi_{EFE,actual}$), we will also use the quantitative estimate of Bischoff and Schneider (2014). This estimate is obtained starting from the zonally averaged atmospheric energy budget:

$$\partial_t < \overline{\mathcal{E}} >= -\partial_y < \overline{vh} > + \overline{\mathcal{S}^t} - \overline{\mathcal{L}^t} + \overline{\mathcal{F}^s}, \tag{2.3}$$

where the left-hand side represents the atmospheric energy storage, with $\mathcal{E} = C_p T + L_v q$ and is approximately zero for long time averages, and $\overline{\mathcal{S}^t} - \overline{\mathcal{L}^t} + \overline{\mathcal{F}^s}$ is the net energy input (NEI), that is, the sum of TOA radiative fluxes (incoming shortwave radiation $\mathcal{S}^t$ minus outgoing longwave radiation $\mathcal{L}^t$) and upward surface fluxes ($\mathcal{F}^s$). For simplicity, here we express this equation in local Cartesian coordinates with $y = a\phi$ (where a is Earth's radius), but all calculations from the model outputs are done in spherical coordinates. Expanding the atmospheric energy flux around the equator to a first-order Taylor expansion in latitude (c.f., Bischoff and Schneider, 2014), the latitude of the zero energy flux can be expressed as

$$\phi_{EFE,analytical} \approx -\frac{1}{a} \frac{\langle \overline{vh} \rangle_0}{\overline{\mathcal{S}_0^t} - \overline{\mathcal{L}_0^t} + \overline{\mathcal{F}_0^s}}, \tag{2.4}$$

where the subscript 0 indicates quantities evaluated at the equator. This derived EFE latitude, which we refer to as the "analytical EFE", is proportional to the cross-equatorial energy flux and inversely proportional to the NEI at the equator.

2.3 Summertime Means

The simulated seasonal cycle of the zonal mean precipitation is shown in Fig. 2.1 for the three simulations with different mixed layer depths. In all simulations, tropical precipitation tends to be concentrated along narrow convergence zones that migrate seasonally across the equator into the summer hemisphere. Despite these broad similarities, important differences are observed: 1) With decreasing mixed layer depths, tropical precipitation shows a decreasingly lagged response to the imposed insolation, which reaches its maximum in the NH on Jun 21 (NH summer solstice); 2) with decreasing mixed layer depths, the ITCZ has larger seasonal excursions away from the equator (~8° in Aqua20m and ~30° in Aqua0.2m); 3) as the mixed layer depth is decreased, we see the appearance of a secondary precipitation band in the summer hemisphere that remains close to the equator throughout the warm season (Fig. 2.1b, c). The zero meridional mass streamfunction tracks the surface MSE maximum in all simulations (shown in Fig. 2.7 for Aqua20m) and covaries with the

precipitation maximum, as expected from convective quasi-equilibrium theories for monsoon location (e.g., Emanuel, 1995; Privé and Plumb, 2007a). The fact that a lagged response to the seasonal cycle of insolation exists even for a very shallow mixed layer depth indicates the importance of dynamic and thermal atmospheric inertia for the circulation and precipitation seasonal evolution.

Before investigating energetic constraints on the ITCZ position on subseasonal timescales, here we first focus on seasonal (summertime) averages. In particular, we consider NH summer and, to account for the different precipitation and circulation responses in simulations with different mixed layer depths (Fig. 2.1a−c), we perform averages around times of largest precipitation shifts (rather than averages around NH summer solstice). More specifically, we compute averages over the time period during which the ITCZ ($\phi_{P_{ITCZ}}$) is poleward of 85% of its maximum excursion, as indicated within the orange lines in Fig. 2.1a−c. The resulting averaged streamfunction and precipitation are shown in Fig. 2.2a, c, e. Differences in the seasonal ITCZ migrations in the three simulations are reflective of differences in the seasonal cycle of the tropical overturning circulation and associated ascending branch. As the mixed layer depth becomes shallower, the summertime circulation is increasingly dominated by one single, strong winter Hadley cell that becomes progressively more and more cross equatorial. While this pattern is not representative of summertime conditions of the zonally averaged Hadley cell observed on Earth, it has been shown to be relevant for the dynamics of sector-averaged overturning circulations associated with monsoons (e.g., Bordoni and Schneider, 2008; Merlis et al., 2013).

Fig. 2.3 shows the NH summertime averaged precipitation and vertically integrated total energy transport in the three simulations. The actual EFE is shown by the green circle, while the analytical EFE is shown by the red arrow. When considering summertime averages, both the actual and the analytical EFE show excellent skills in capturing the location of the precipitation maximum and, therefore, the poleward boundary in the summer hemisphere of the cross-equatorial cell (Fig. 2.2a, c, e). As we will discuss in the next session, this does not always hold true when the full seasonal cycle is being considered.

The approximate colocation between the EFE and the ITCZ is also based on the assumption that in the tropics the energy transport is primarily effected by the mean meridional circulation (that is, the Hadley cell). For a typical annual mean pattern of two Hadley cells almost symmetric about the equator, the cell's ascending branch,

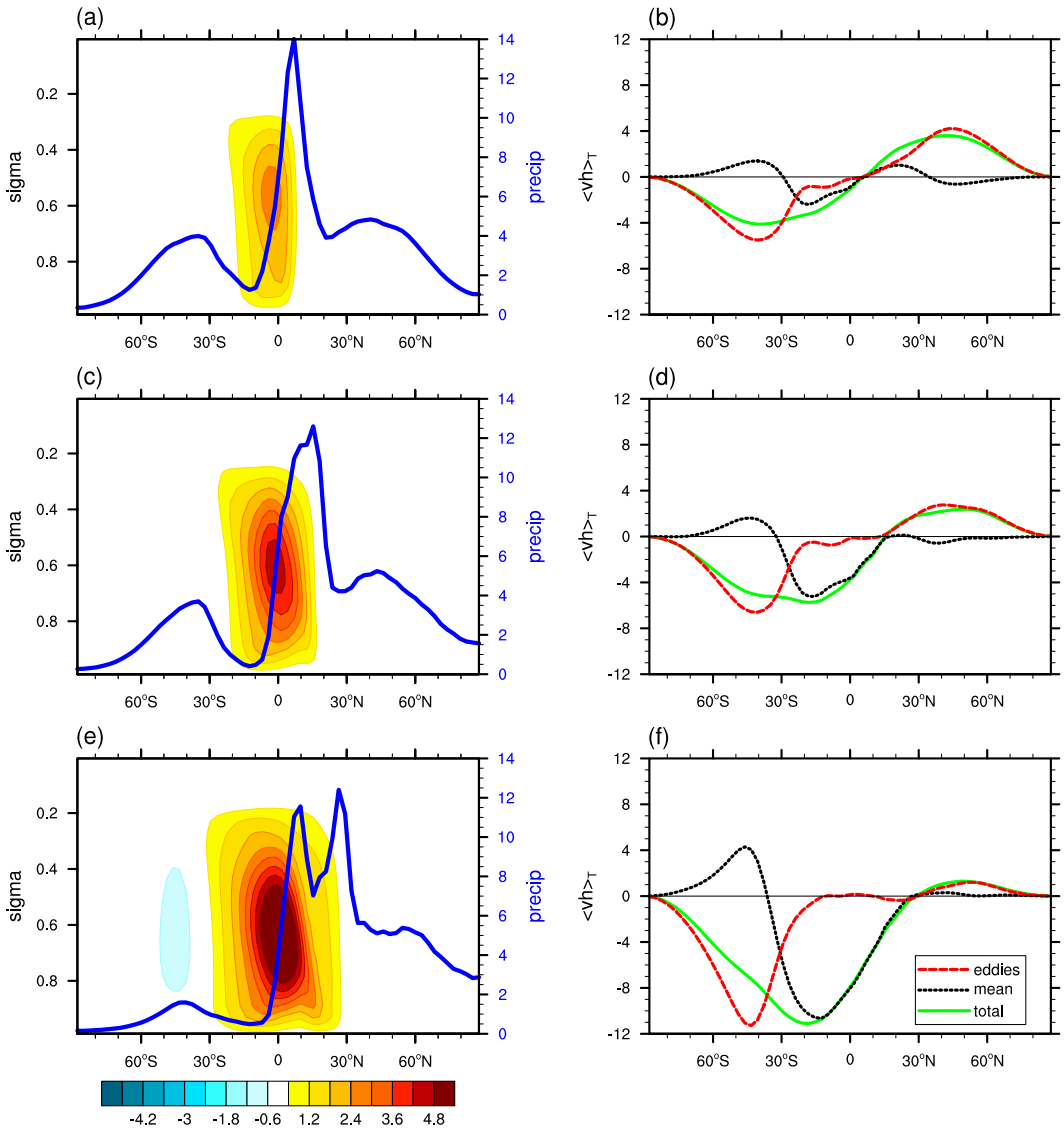

Figure 2.2: (a, c, e) Summertime mean meridional streamfunction (shading, 10^{11} kg s^{-1}) and (b, d, f) energy transport for Aqua20m, Aqua10m, and Aqua0.2m, respectively. In a, c, e, the zonal mean precipitation distribution is shown in blue (right y axis, mm day^{-1}). In b, d, f, total energy transport is shown in green, mean energy transport in black and eddy energy transport in red.

which is where the ITCZ resides, is also where the mean energy, mass and moisture transports vanish. However, the energy balance more directly constrains the total, rather than the mean, energy transport, which justifies the identification of the EFE with the latitude at which the total transport goes to zero taken by many previous studies (e.g., Adam et al., 2016a; Bischoff and Schneider, 2014). This however raises the question of how the total transport is decomposed into mean and eddy

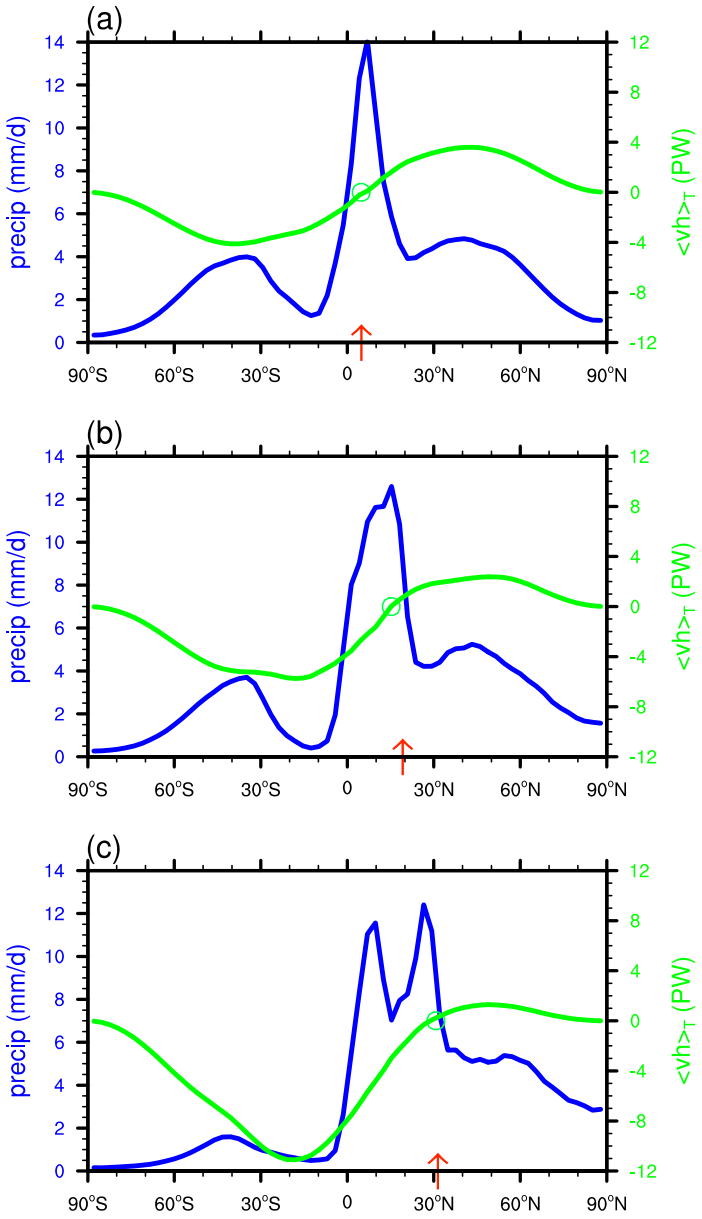

Figure 2.3: Summertime zonal mean precipitation (blue) and vertically integrated energy transport (green) in (a) Aqua20m, (b) Aqua10m, and (c) Aqua0.2m. The green circles are $\phi_{EFE,actual}$ and the red arrows $\phi_{EFE,analytical}$.

contributions, and to what extent latitudes of EFE estimated from mean and total transports coincide.

This decomposition is shown in Fig. 2.2b, d, f. For the Aqua20m experiment, we find that while the mean transport dominates in the stronger winter cell, the eddy transport is comparable to the mean transport in the weaker summer cell; this configuration is similar to what observed on Earth for the zonal mean ITCZ. In this

case, although the eddy transport is not negligible, total, mean and eddy transports all vanish at the same location. In Aqua0.2m and Aqua10m, where the asymmetry between the winter and summer cells is much stronger than in the Aqua20m case, we see that because there is no significant positive mean transport in the summer cell, the poleward boundary of the winter Hadley cell does not coincide with the latitude at which the mean energy transport switches sign (i.e., there is no clear mean EFE). Rather, the dividing boundary between southern and northern cells is the latitude where the total energy transport transitions from being effected by the mean in the winter cell (with negligible contribution by the eddies) to being primarily effected by the eddies in the weaker and entirely eddy-driven summer cell (e.g., Schneider and Bordoni, 2008; Singh et al., 2017; Walker and Schneider, 2006). This pattern is in disagreement with the conventional picture of a weakly cross-equatorial Hadley cell, in which the mean energy transport in the two cells is comparable in magnitude and of opposite sign, and the mean EFE coincides with the ITCZ. In this pattern, in fact, not only is the eddy energy transport not negligible in the proximity of the ITCZ, but also a mean EFE cannot always be identified. This confirms that in general the total EFE is a better predictor of the ITCZ location than the mean EFE. For this reason, for the rest of this paper we will focus on the total EFE and explore its relation to the ITCZ location throughout the seasonal cycle.

2.4 Seasonal Migrations

Lag between the EFE and the ITCZ

One interesting feature emerging from Fig. 2.1a−c is that the EFE (thick black lines) always leads the precipitation maximum, even when the mixed layer depth is very shallow. While some previous studies have shown a similar lead-lag relationship in observations and modeling studies, no explanation of this seasonal offset has been offered. That the ϕ_{EFE} leads the $\phi_{P_{ITCZ}}$ can also be seen in a scatter plot of their seasonal evolution (Fig. 2.4a). The two quantities are correlated in all simulations, with correlation coefficients of 0.48, 0.72 and 0.84 in Aqua20m, Aqua10m, and Aqua0.2m, respectively. However, the existence of a lag between the two quantities leads to an elliptical pattern rather than a straight line. Also, while the slope between the ϕ_{EFE} and the $\phi_{P_{ITCZ}}$ is close to one in all simulations, the ϕ_{EFE} tends to be poleward of the $\phi_{P_{ITCZ}}$. This is especially evident in the Aqua0.2m simulation and is a result of the latitudinal separation between the EFE and the ITCZ in strongly cross-equatorial Hadley cells (e.g., Faulk et al., 2017). Given that many previous studies have more directly related the ITCZ to the cross-equatorial energy transport,

we also plot the scatter plot of the seasonal evolution of $\phi_{P_{ITCZ}}$ and cross-equatorial energy transport (Fig. 2.4b). Seasonal variations of $\phi_{P_{ITCZ}}$ and cross-equatorial energy transport are strongly anticorrelated with a slope of around -2.76° PW^{-1} (with correlation coefficients of 0.66, 0.81, and 0.88 in Aqua20m, Aqua10m, and Aqua0.2m, respectively), and have a time offset relative to each other. While the regression coefficient between the ITCZ location and the cross-equatorial energy transport in our simulations is similar to what is seen in observations (-2.7° PW^{-1}, Donohoe et al. (2013)), we find that it remains roughly constant with decreasing mixed layer depths, unlike what was argued in their paper. The reason for this discrepancy is unclear, but it might arise from the lack of cloud and other radiative feedbacks in our idealized model. Additionally, the sensitivity of the ITCZ location to changes in cross-equatorial energy transport is not constant throughout the year, but has a semi-annual component, primarily arising through seasonal changes in the NEI into the equatorial atmosphere (Eq. (2.4)). Consistent with arguments in Donohoe et al. (2013), this leads to a flatter slope between the ITCZ location and the cross-equatorial energy transport at times of maximal off-equatorial excursions.

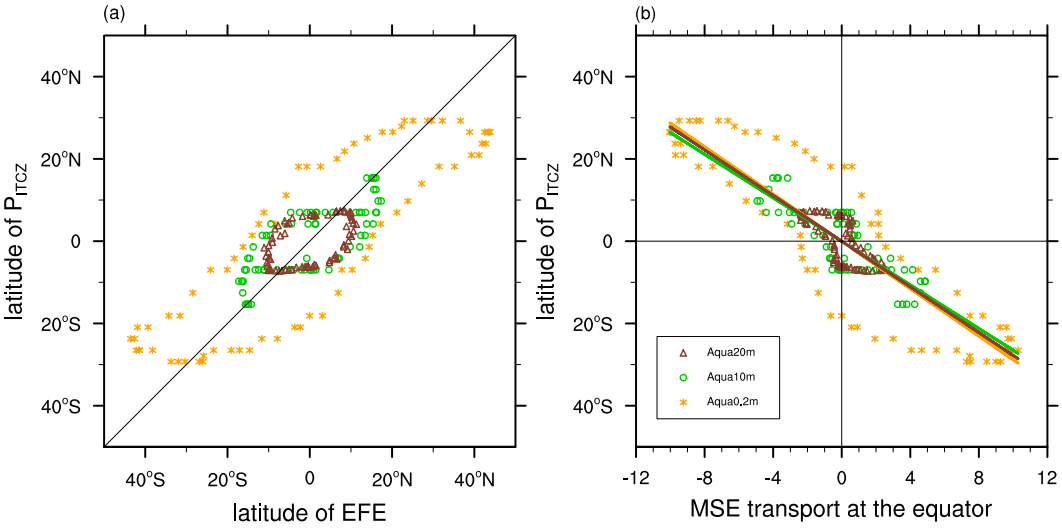

Figure 2.4: Scatterplot of the seasonal cycle of (a) $\phi_{\mathrm{P_{ITCZ}}}$ v.s. $\phi_{\mathrm{EFE,actual}}$, and (b) $\phi_{\mathrm{P_{ITCZ}}}$ v.s. cross-equatorial energy transport in Aqua20m (brown open triangles), Aqua10m (green open circles), and Aqua0.2m (orange asterisks). The slopes in (b) are -2.77° PW^{-1} for Aqua20m, -2.65° PW^{-1} for Aqua10m and -2.87° PW^{-1} for Aqua0.2m.

In order to quantify more directly the seasonal evolution of the ITCZ, the circulation, and the EFE, here we define their seasonal amplitude and phase as the amplitude and phase of the annual harmonic of the ITCZ position ($\phi_{P_{ITCZ}}$), the location of the

zero streamfunction ($\phi_{\psi=0}$), and the EFE ($\phi_{EFE,actual}$). Corresponding values are shown in Table. 2.1. It is evident that for all simulations the EFE leads the ITCZ, with the lead decreasing from about two months in Aqua20m to about one month in Aqua0.2m. In general, the circulation boundary and the ITCZ tend to evolve more closely in phase during the seasonal cycle.

Table 2.1: Amplitude and phase of the annual cycle of the $\phi_{P_{ITCZ}}$, $\phi_{\psi=0}$, and ϕ_{EFE} in the Aqua20m, the Aqua10m, and Aqua0.2m simulations. The phase shown here is the day of the crest of the annual cycle relative to the time of equinoctial insolation on March 21. The last row shows the phase difference between $\phi_{P_{ITCZ}}$ and ϕ_{EFE}.

	Amplitude (degree)			**Phase (day)**		
	*Aqua*0.2*m*	*Aqua*10*m*	*Aqua*20*m*	*Aqua*0.2*m*	*Aqua*10*m*	*Aqua*20*m*
$\phi_{P_{ITCZ}}$	30.19	10.56	7.59	121.83	162.47	197.26
$\phi_{\psi=0}$	32.11	17.59	11.41	118.03	159.12	184.55
ϕ_{EFE}	37.53	15.45	10.46	90.76	122.38	136.52
δphase ($\phi_{P_{ITCZ}} - \phi_{EFE}$)				31.07	40.09	60.74

These results raise a number of questions: 1) Why does the EFE always lead the ITCZ, even in the limit of very small thermal inertia of the lower boundary? 2) To the extent that precipitation might be more strongly constrained by the mass and moisture budgets than the energy budget on seasonal timescales, can we offer any insight on when and how the EFE fails as a diagnostic of the ITCZ during the seasonal cycle?

As discussed throughout this paper, energetic constraints on the ITCZ location have emphasized the anticorrelation between the cross-equatorial energy transport and the position of the ITCZ, with the ITCZ shifting into the relatively warmer hemisphere (that is, the summer hemisphere during the seasonal cycle) and energy being transported into the relatively cooler hemisphere (that is, the winter hemisphere) in the same direction as the Hadley cell's upper branch. One important assumption is that the effective energy stratification, or GMS, of the Hadley cell, which is defined in this study as GMS $= \int_0^{p_s} \overline{vh}\frac{dp}{g} / \int_0^{p_m} \overline{v}\frac{dp}{g}$, where p_m is the pressure at maximum streamfunction, is positive (e.g., Feldl et al., 2017; Frierson, 2007; Hill et al., 2015; Kang et al., 2009). According to this definition, the GMS represents the energy transported per unit mass transport. With positive GMS, the vertically integrated energy transport and the mass transport in the cell's upper branch have the same sign, and the EFE is collocated with the boundary between the two Hadley cells (and hence is just slightly poleward of the ITCZ). Our simulations suggest that in

the course of the seasonal cycle this does not always hold true. In fact, one important consequence of the lead-lag relationship between the EFE and the ITCZ is that there are times during the seasonal cycle when the EFE and the ITCZ are on opposite sides of the equator (e.g., around May to Jun., and Nov. to Dec.), leading to a breakdown of the commonly assumed anti-correlation between the ITCZ and the cross-equatorial energy transport. More generally, this suggests that vertically integrated energy transport and upper-level mass transport at certain latitudes and times are in opposite directions, implying negative GMS of the corresponding Hadley cell. In the following, we want to investigate mechanisms of the lag relationship between the EFE and the ITCZ and changes in the circulation leading to negative GMS. We primarily focus on the Aqua20m simulation, which features the largest phase difference between the EFE and the ITCZ, and a Hadley cell structure and seasonality that is more similar to the zonally averaged circulation observed on Earth.

Seasonal evolution of the EFE and the ITCZ position

To understand why the EFE leads the ITCZ, it is useful to go back to the energy budget and understand what determines the phase of the annual cycle of the ϕ_{EFE}. At each given latitude, the total energy transport in petawatts (PW) can be expressed as:

$$\langle\overline{vh}\rangle_{T,\phi} = 2\pi \int_{SP}^{\phi} \partial_y \langle\overline{vh}\rangle cos\phi a^2 d\phi = 2\pi \int_{SP}^{\phi} \mathrm{NEI}_{\mathrm{eff}}\ cos\phi a^2 d\phi, \tag{2.5}$$

where we start the integration from the South Pole (SP) where there is no energy transport, a is the radius of the Earth, subscript T is used to emphasize that this quantity represents the energy transport in units of PW, and $\mathrm{NEI}_{\mathrm{eff}}$ is the effective NEI, which is equal to NEI minus the atmospheric storage ($\partial_t \langle\overline{\mathcal{E}}\rangle$). In Aqua20m, the atmospheric energy storage term is negligible in the energy balance equation (c.f. Eq. (2.3)) on seasonal timescales, so the divergence of the energy transport itself is approximately equal to the NEI into the atmospheric column at each given pentad. However, the seasonal distribution of the storage term does have nonnegligible contributions to the total meridional energy transport, as will be shown below.

Based on Eqs. (2.2) and (2.5), the EFE is the latitude at which the meridionally integrated energy input to its north and south is the same and equal to zero:

$$\begin{aligned} \langle\overline{vh}\rangle_{T,\phi_{EFE}} &= 2\pi \int_{SP}^{\phi_{EFE}} \mathrm{NEI}_{\mathrm{eff}} cos\phi a^2 d\phi \\ &= 2\pi \int_{\phi_{EFE}}^{NP} \mathrm{NEI}_{\mathrm{eff}} cos\phi a^2 d\phi \\ &= 0. \end{aligned} \tag{2.6}$$

This is to say that the EFE, rather than being collocated with maximum energy flux divergence as it is often the case for the precipitation maximum, is determined by the meridional integral of the NEI. The relationship between the seasonal evolution of the EFE and the $\mathrm{NEI}_{\mathrm{eff}}$ is made more apparent in Fig. 2.5: while there are regions of localized $\mathrm{NEI}_{\mathrm{eff}}$ maxima, which indicate maximum divergence near the ITCZ, it is the hemispherically asymmetric distribution of the $\mathrm{NEI}_{\mathrm{eff}}$ in regions away from the precipitation (and hence $\mathrm{NEI}_{\mathrm{eff}}$) maxima that determines the seasonal evolution of the EFE. In other words, the overall seasonally evolving spatial pattern of $\mathrm{NEI}_{\mathrm{eff}}$ dictates the seasonal evolution of the EFE and its migration on either side of the equator, whereas its local structure more directly determines the divergence of the energy flux.

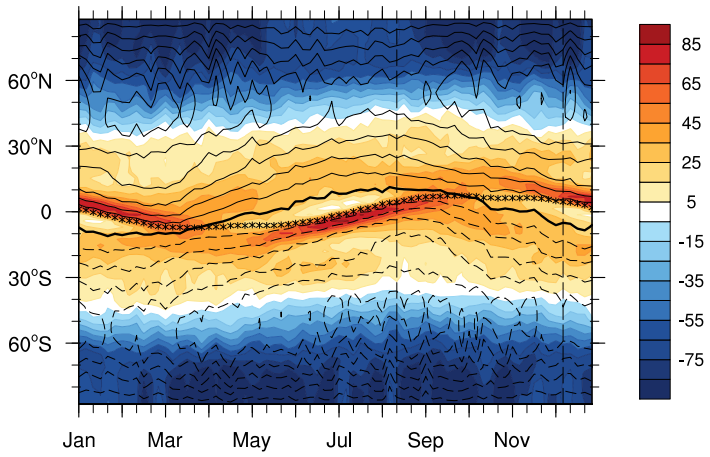

Figure 2.5: Seasonal cycle of the zonal mean effective net energy input ($\mathrm{NEI}_{\mathrm{eff}}$, shading, W m^{-2}) and vertically integrated meridional energy flux (contours, interval 2.5×10^7 W m^{-1}) in Aqua20m. Asterisks show $\phi_{P_{ITCZ}}$. Vertical black dashed lines indicate pentads Aug. 11–15 and Dec. 6–10, respectively, which are chosen as times in which the southern winter cross-equatorial Hadley cell is expanding into and retreating from the northern summer hemisphere (as shown in Fig. 2.8a, b), but has the same ITCZ location.

A more direct assessment of factors contributing to the seasonal evolution of the energy transport – and with it of the EFE – can be obtained through the following

Table 2.2: Amplitude (PW) and phase (day) of the annual cycle of the meridional energy transport at 11°N and of the contributions to $\langle\overline{vh}\rangle_{T,\phi}$ from each term in Eqs. 2.7–2.9.

	$TermA$	$TermC$	$TermB$			
				$TermB_1$	$TermB_2$	$TermB_3$
$\langle\overline{vh}\rangle_{T,11°\mathrm{N}}$ **Amplitude (PW)**	**1.83**	**3.17**	**3.87**	23.07	3.4	18.88
$\langle\overline{vh}\rangle_{T,11°\mathrm{N}}$ **Phase (day)**	**317.46**	**76.75**	**282.2**	267.35	161.49	74.29

decomposition:

$$\langle\overline{vh}\rangle_{T,\phi} = \overbrace{2\pi\int_{SP}^{\phi}\partial_y\langle\overline{vh}\rangle cos\phi a^2 d\phi}^{A} \tag{2.7}$$

$$= \underbrace{2\pi\int_{SP}^{\phi} NEI cos\phi a^2 d\phi}_{B}\underbrace{-2\pi\int_{SP}^{\phi}\partial_t\langle\overline{\mathcal{E}}\rangle cos\phi a^2 d\phi}_{C} \tag{2.8}$$

$$= \underbrace{2\pi\int_{SP}^{\phi}\overline{\mathcal{S}^t} cos\phi a^2 d\phi}_{B_1}\underbrace{-2\pi\int_{SP}^{\phi}\overline{\mathcal{L}^t} cos\phi a^2 d\phi}_{B_2}$$

$$\underbrace{+2\pi\int_{SP}^{\phi}\overline{\mathcal{F}^s} cos\phi a^2 d\phi}_{B_3} - 2\pi\int_{SP}^{\phi}\partial_t\langle\overline{\mathcal{E}}\rangle cos\phi a^2 d\phi, \tag{2.9}$$

where the total energy transport (term A) is decomposed into contributions from the NEI (term B) and the storage term (term C). The NEI (integrand in term B) can be further decomposed into shortwave (integrand in term B_1) and longwave (integrand in term B_2) radiation at TOA, and surface fluxes (integrand in term B_3). The evolution of the seasonal anomaly (defined as the deviation from the annual mean at each latitude) of each term is shown in Fig. 2.6, which suggests that it is the seasonal cycle of the shortwave radiation that contributes the most to the phase of the seasonal evolution of the energy transport.

More quantitatively, amplitude and phase of the annual harmonic of each term at 11°N is shown in Table. 2.2. While the contributions from the NEI and the energy storage have similar seasonal amplitudes, the phase of the total energy transport is primarily influenced by the phase of the NEI-derived energy transport. Among individual terms in the NEI, the contribution from $\mathcal{S}^t$ is the one that features the

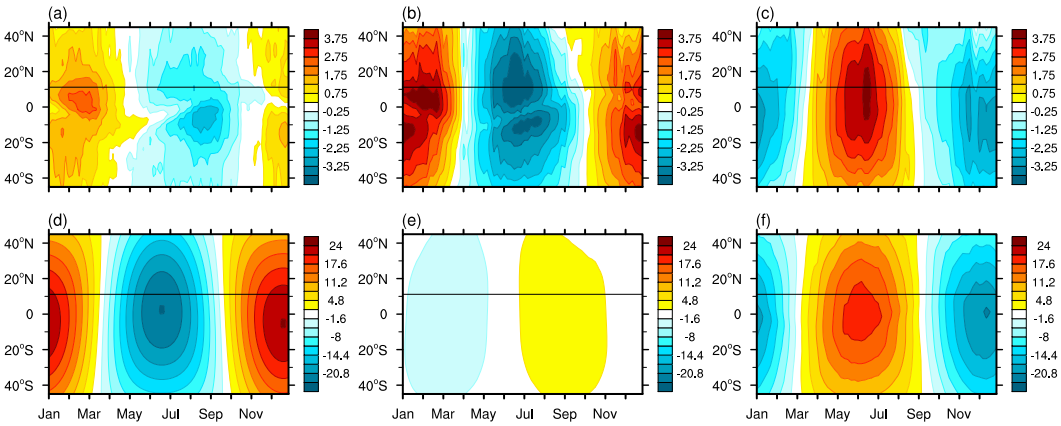

Figure 2.6: Seasonal evolution of the anomalous (relative to the annual mean) (a) vertically integrated energy transport and its decomposition into contributions from (b) net energy input, (c) negative atmospheric energy storage, (d) downward shortwave radiation at the TOA, (e) negative upward longwave radiation at the TOA, and (f) upward surface fluxes in Aqua20m. Thin black lines indicate 11°N, the location we choose to show phase and amplitude of all terms contributing to the vertically integrated energy transport in Table. 2.2.

largest amplitude and the phase that best agrees with that of the NEI-derived, and hence, of the total energy transport. This implies that the seasonal migration of the EFE is almost in phase with the seasonally varying insolation forcing and that the atmospheric circulation needs to change to achieve the required energy flux and energy flux divergence. However, the atmospheric circulation, which is primarily constrained by surface thermodynamics, cannot adjust as rapidly as the EFE because of thermal and dynamic inertia. This is to say that the tropical precipitation nearly co-evolves with surface temperature and surface MSE (e.g., Emanuel, 1995; Privé and Plumb, 2007a) and, like these surface thermodynamic quantities, lags the insolation and the EFE (Fig. 2.7b). The lag between the EFE and the Hadley cell's poleward extent and the associated ITCZ is thus shorter with decreasing mixed layer depths and thermal inertia of the lower boundary (e.g., Cronin and Emanuel, 2013; Dwyer et al., 2012). In summary, the lag between the EFE and the ITCZ is related to the lag between insolation and surface temperature. The phase offset between the EFE and the ITCZ, however, contradicts the assumption that the GMS of the Hadley cell is always positive, raising the question of how the circulation adjusts to achieve the required energy balance.

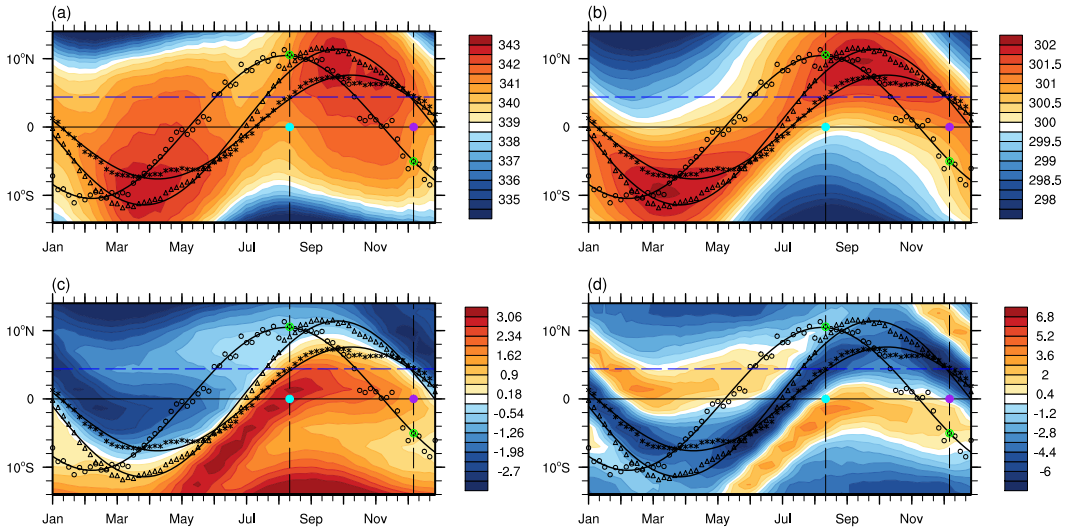

Figure 2.7: Seasonal evolution of the zonal mean (a) moist static energy (MSE, K), (b) temperature (K), (c) meridional gradient of temperature (10^{-6}K m^{-1}), and (d) Laplacian of temperature (10^{-12}K m^{-2}) at the lowest model level (σ= 0.989) in shading in Aqua20m. The open circles are $\phi_{EFE,actual}$, the open triangles $\phi_{\psi=0}$, and the asterisks $\phi_{P_{ITCZ}}$. Solid thick black lines show their annual harmonic. Vertical black dashed lines indicate pentads Aug. 11−15 and Dec. 6−10, respectively, shown in Fig. 2.5, which have the same ITCZ location, shown by the horizontal blue dashed line, but different EFE, denoted by the green ⊗ symbol. The horizontal thin black line indicates the equator. The cyan and purple dots represent location (equator) and times (Aug. 11−15 and Dec. 6−10, respectively) for the vertical cross-sections shown in Fig. 2.8c, d.

Circulation response

To understand how the system achieves negative GMS at some latitudes and times during the seasonal cycle, we investigate how the circulation and the energy field evolve with time. We begin by showing in Fig. 2.7 the evolution of the circulation boundary, the ITCZ, and the EFE. As discussed in the previous subsection, the phase of the annual cycle of the EFE is mainly determined by the solar insolation, while the circulation boundary and the precipitation maximum migrate with a lag; yet, energy balance still needs to be satisfied. We therefore select two pentads (Aug. 11−15 and Dec. 6−10) at which the ITCZ is located at the same latitude in the NH (around 4.5°N), while the EFE sits in the NH (around 10.5°N) and SH (around 5°S), respectively. How do the corresponding Hadley cells differ at these two times to achieve oppositely directed energy transports near the equator while featuring ascending branches at approximately the same latitude? The massflux

streamfunctions at these two pentads (Fig. 2.8a and b) show that the cross-equatorial cell is much stronger on Aug. 11−15 than it is on Dec. 6−10, which highlights the existence of an asymmetry between the expanding and retreating phases of the cross-equatorial winter cell.

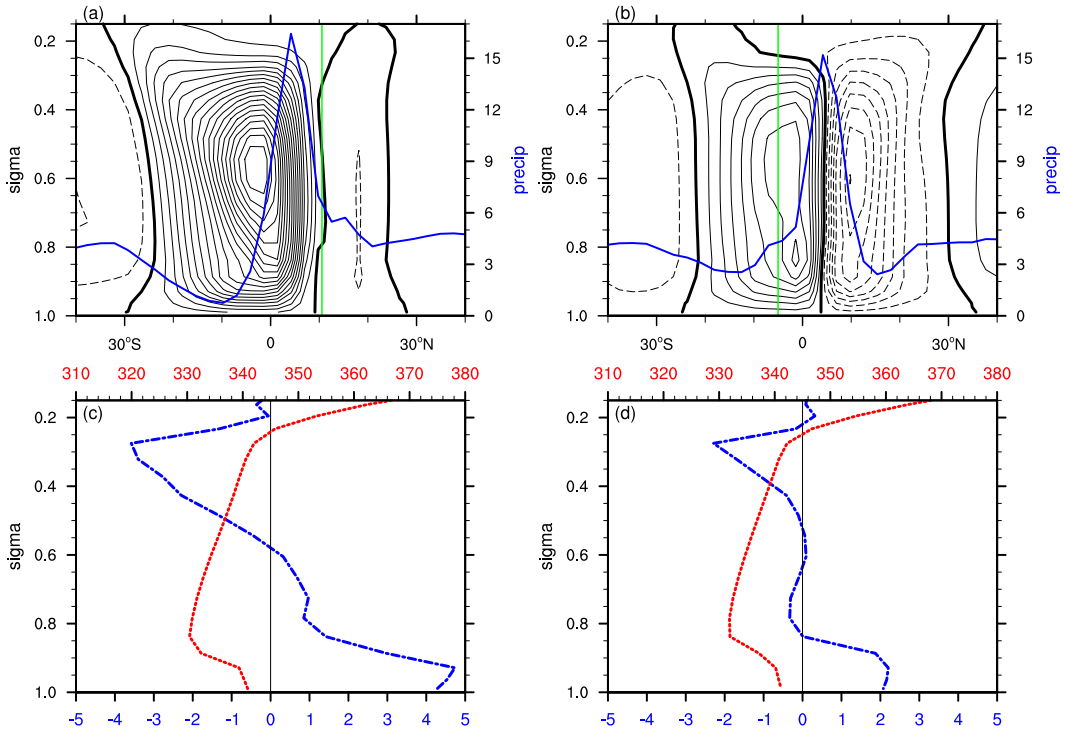

Figure 2.8: Mass meridional streamfunction (contours, interval 1.75×10^{10} kg s^{-1}) in Aqua20m for (a) Aug. 11−15 and (b) Dec. 6−10. Solid (dashed) contours indicate positive (negative) values and the thick black contours the zero value. Blue solid line is zonal mean precipitation and the green vertical line indicates $\phi_{EFE,actual}$. Vertical profiles of the MSE (red dotted line, K) and meridional wind (blue dashed-dotted line, m s^{-1}) at the equator on (c) Aug. 11−15 and (d) Dec. 6−10.

To understand how oppositely signed cross-equatorial energy transport is effected at these two pentads, the corresponding vertical profiles of v and h at the equator are shown in Fig. 2.8c and d, for the Aug. and Dec. pentad, respectively. The MSE vertical profiles at both pentads are consistent with observed typical profiles in the tropical atmosphere, with a minimum in the mid-to-lower troposphere and values at upper levels being larger than those close to the surface. While largely similar, these profiles differ in the lower atmosphere, with slightly higher MSE values below the minimum being found over a deeper layer in the retreating phase. Vertical profiles of the meridional wind, however, feature more pronounced differences.

More specifically, in the retreating phase, the cross-equatorial Hadley cell develops a shallow return flow at heights where the MSE minimum is located. This is also evident in the structure of the streamfunction (Fig. 2.8b). That the differences in the circulation (or meridional wind) vertical structure are more important than the differences in the MSE vertical structure for the sign reversal of the GMS in the retreating phase of the winter Hadley cell can be more accurately quantified by decomposing the anomalous mean MSE flux according to

$$\langle \delta(\overline{v}\overline{h}) \rangle = \langle \overline{v}\delta\overline{h} \rangle + \langle \overline{h}\delta\overline{v} \rangle, \tag{2.10}$$

where δ represents the difference between the Dec. and Aug. fields (Dec. 6−10 minus Aug. 11−15) and we neglect the quadratic term, which is much smaller than the linear terms. The first term represents the contribution to the anomalous mean MSE flux due to changes in the MSE vertical profile, while the second term represents the contribution due to changes in the meridional wind vertical profile. As shown in Fig. 2.9, in the tropics differences in the total MSE flux between the two pentads are almost entirely accounted for by differences in mean MSE flux, which in turn are primarily dominated by differences in the circulation vertical structure rather than differences in MSE profiles. In other words, it is the presence of the shallow return flow near the MSE minimum, rather than MSE increases at lower levels, that causes the vertically integrated energy transport to be in the direction of the lower-level mass transport in the retreating phase, resulting in a negative GMS. At other pentads, the retreating cell does not always feature a shallow return flow as well defined as that seen around Dec. 6−10. Nonetheless, the structure of the associated streamfunction is very different from that of the winter cell in its expanding phase, with the upper- and lower-level meridional flow being confined in very thin layers, which also favors negative GMS (not shown). This means that while the EFE evolves seasonally almost in phase with the insolation, the surface temperature, the Hadley cell, and its ascending branch cannot change as rapidly. Without shifting the boundary between the two Hadley cells and the ITCZ across the equator together with the EFE, the Hadley cell achieves the required energy transport by changing its vertical structure into one with negative GMS.

An interesting question arising from this discussion is how the retreating cell develops the shallow return flow and why an asymmetry exists between the times at which the cross-equatorial Hadley cell (the southern cell for northern summer and the northern cell for southern summer) is expanding into and retreating from the summer hemisphere. Fig. 2.7c shows that the meridional temperature gradient

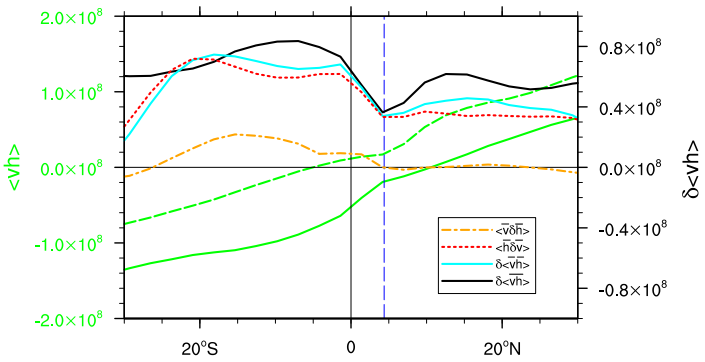

Figure 2.9: Meridional distribution of energy flux (W m^{-1}) on Aug. 11−15 (solid green line) and Dec. 6−10 (dashed green line, left y axis) and difference (Dec. 6−10 minus Aug. 11−15) between the two ($\delta\langle\overline{vh}\rangle$, black solid line, right y axis). Anomalous mean energy flux ($\delta\langle\overline{v}\,\overline{h}\rangle$), and contributions from changes in meridional wind profile ($\langle\overline{h}\delta\overline{v}\rangle$) and from changes in MSE profile ($\langle\overline{v}\delta\overline{h}\rangle$) are shown in cyan solid line, red dashed line, and orange dashed-dotted line, respectively (right y axis). The vertical blue dashed line indicates the latitude of the ITCZ ($\phi_{P_{ITCZ}}$) at these two pentads.

within the latitudinal span of the cross-equatorial Hadley cell is stronger when the cell is expanding than it is when retreating, which might support a weaker overturning circulation in its retreating phase. We also find that the meridional Laplacian of temperature below the ITCZ is slightly more negative when the cell is retreating from the summer hemisphere (Fig. 2.7d), suggestive of the role of boundary layer convergence in favoring bottom heavy vertical velocity profiles (e.g., Back and Bretherton, 2009a; Lindzen and Nigam, 1987; Sobel, 2007). We therefore want to investigate the reasons for the asymmetry in the near-surface temperature evolution. We do so by plotting in Fig. 2.10 the seasonal evolution of the near-surface temperature at 10°N (asterisks) and 10°S (crosses). It can be seen that in both hemispheres the near-surface temperature evolves more slowly as it is increasing and more rapidly as it is decreasing, resulting in a tilted sinusoidal evolution (i.e., the temperature evolution shifts to the right (left) of the sine wave when it is warmer (colder) than annual mean temperature). With opposite temperature seasonal anomalies and oppositely tilted temperature evolutions at 10°N and 10°S, the averaged meridional surface temperature gradient near the equator, approximated by the difference between the temperature at 10°N and 10°S, is stronger as the winter cross-equatorial cell is expanding (before the time at which NH temperature peaks and the precipitation reaches the location of its maximum northward excursion) than as it is retreating (after the time at which NH temperature peaks).

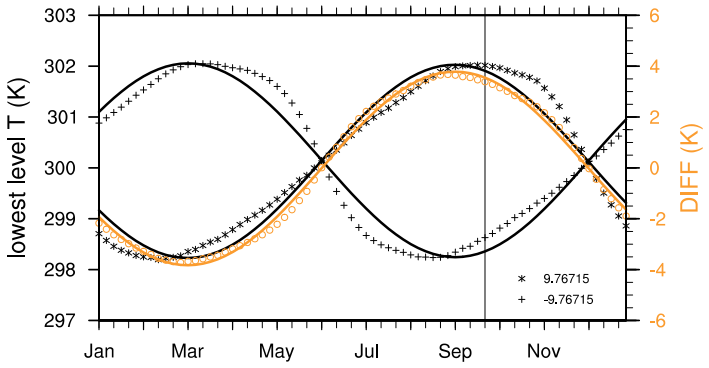

Figure 2.10: Seasonal evolution of the lowest level atmospheric temperature at around 10°N (black asterisks) and 10°S (black crosses) in Aqua20m. Orange open circles show the difference between these two, representative of the average meridional temperature gradient near the equator. Solid lines show their annual harmonic. The vertical black line indicates the time at which $\phi_{P_{ITCZ}}$ has the largest northward excursion.

While the mechanisms responsible for the tilted temperature evolution remain unclear, they most likely involve nonlinearities in the effective heat capacity of the coupled atmosphere/slab ocean system and/or nonlinear circulation influences. These mechanisms will be explored in more detail in future work. Through its impact on the circulation, the asymmetry in the temperature evolution appears essential for the lead-lag relationship between the EFE and the ITCZ, as complete symmetry between expanding and retreating phases would imply cross-equatorial winter cells with equal mass and energy transports for any given ITCZ location. Hence, the EFE and the ITCZ would evolve in phase.

2.5 Discussions and Conclusions

In this study, we have explored the extent to which emerging energetic constraints on the ITCZ provide accurate predictions of its evolution on seasonal and shorter timescales in idealized aquaplanet simulations with different mixed layer depths. In agreement with previous studies, the EFE shows excellent skill in capturing the location of the precipitation maximum on seasonal or longer means. One important caveat is that it is the total, rather than the mean, EFE that provides the best ITCZ predictor across simulations. As the mixed layer depth decreases, the asymmetry between the winter and summer Hadley cell increases during the warm seasons, with the strong and broad winter Hadley cell approaching conservation of angular momentum and the weak and narrow summer cell being eddy driven (e.g., Schneider and Bordoni, 2008; Singh et al., 2017; Walker and Schneider, 2006). In this case,

unlike what's usually assumed, not only is the eddy energy transport not negligible in the summer cell, but it determines the zero of the total energy flux even when the mean energy flux approaches zero but does not change sign. Hence, in these more asymmetric cases, the poleward boundary of the winter cell in the summer hemisphere, which is approximately collocated with the ITCZ, coincides with the latitude at which the total, and not the mean energy transport, switches sign as it transitions from being effected by the mean in the winter cell to being effected by the eddies in the summer cell.

On subseasonal timescales, we find that the EFE leads the ITCZ and the maximum in lower-level MSE. This arises because, while the seasonal evolution of the EFE is primarily in phase with the insolation changes, the circulation and associated precipitation more closely track the near-surface temperature and can't adjust as rapidly. In fact, while decreasing with decreasing mixed layer depths, the lag is as large as about one month even for the shallowest depth. This implies that the seasonal evolution of the ITCZ is not simply negatively correlated with the strength of the cross-equatorial energy transport: there are times when the ITCZ and the EFE reside on opposite sides of the equator. It also implies that at these times, the GMS of the Hadley circulation is negative, with the overturning cell transporting energy in the direction of the lower-level, rather than upper-level, mass transport. These results therefore suggest that one important pathway by which the tropical circulation achieves the required energy balance in the seasonal cycle is through changes in the efficiency of its energy transport, that is the GMS, in addition to changes in its mass transport. This manifests as an asymmetry in the vertical structure of the winter cell in its expanding and retreating phases. For a given position of the ascending branch, the cell is much weaker as it retreats from than as it expands into the summer hemisphere and has the tendency to develop a shallow return flow at the levels in the mid-to-lower troposphere where the MSE reaches its minimum, favoring a negative GMS. Differences in the structure, energy transport, EFE and ITCZ of the cross-equatorial Hadley cell in its expanding and retreating phases are schematically summarized in Fig. 2.11 for northern summer.

While we do not have a theory for the development of such a shallow return flow within a circulation with a deep ascent, the asymmetry between the expanding and retreating phases of the winter cell seems to be linked to an asymmetry in the near surface temperature seasonal distribution. More specifically, while the meridional temperature gradient is much larger within the expanding than within

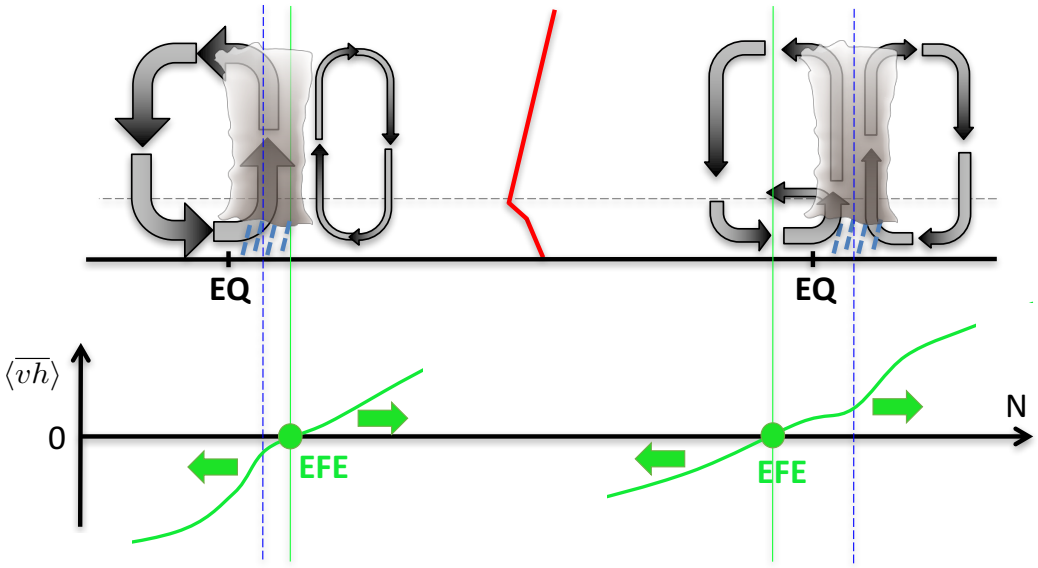

Figure 2.11: Schematic of the asymmetry between the expanding (left) and retreating (right) phases of the winter cross-equatorial cell for northern summer. The upper panel shows the structure of the overturning cell and associated ITCZ, and the vertical profile of MSE in red. The lower panel shows the meridional energy flux (green line) and the EFE (green dots). The vertical blue dashed lines indicate the ITCZ location.

the retreating cell, the near-surface temperature curvature is stronger within the retreating cell close to the ITCZ. These results seem to be consistent with arguments linking boundary layer convergence driven by SST gradients to the development of shallow circulations (e.g., Back and Bretherton, 2009a). To the extent it drives the asymmetry in the seasonal evolution of the winter Hadley cell, the asymmetry in the near-surface temperature seasonal distribution appears to be crucial to the existence of a lag between the EFE and the ITCZ.

That the GMS cannot always be assumed as constant and that its changes need to be accounted for to understand the response of tropical precipitation to radiative perturbations have been highlighted by a few recent studies (e.g., Feldl and Bordoni, 2016; Merlis et al., 2013; Seo et al., 2017). In particular, Seo et al. (2017) show how changes in GMS dominate over changes in mass fluxes in the annual-mean ITCZ response to doubling CO_2 in aquaplanet simulations with full-physics GCMs. Because of the GMS changes, the induced ITCZ shifts in those simulations are not explained by shifts in the EFE. Ours is the first study to show that this can also hold true when considering ITCZ migrations through the course of the seasonal cycle.

Importantly, we show that the GMS can in fact become negative, which makes it possible for the EFE and the ITCZ to reside in opposite hemispheres. Unfortunately what determines the GMS remains an outstanding question (e.g., Raymond et al., 2009). Being dependent on both the vertical MSE distribution and the vertical structure of the large-scale circulation, the GMS depends on complex interactions between large-scale motions, convection and clouds, and has been shown to be very sensitive to different parameterizations (e.g., Seo et al., 2017). Negative values of GMS are however not an artifact of the simplified physics used in our idealized GCM, as they are also seen in seasonally varying aquaplanet simulations with comprehensive GCMs in the TRACMIP archive [Voigt et al. (2016); Biasutti, personal communication, 2017]. Future work leveraging the TRACMIP archive will explore the sensitivity of our results to the parameterized physics.

Overall, our results point to limitations of the atmospheric energy transport to provide quantitative predictions of ITCZ shifts on subseasonal timescales, with significant offsets in both amplitude and phase between the seasonal evolution of the EFE and that of the ITCZ. Across all simulations and at all times during the seasonal cycle, the best predictor of the ITCZ location is the maximum near-surface MSE, as expected from convective quasi-equilibrium views of tropical circulations. Given that the MSE distribution is itself influenced by the circulation, this association is however only diagnostic and itself falls short of a predictive theory. It is also important to emphasize how in our simulations tropical precipitation does not appear to be just controlled by thermodynamic constraints through local temperature (or MSE) maxima. In the Aqua0.2m simulation, and to some extent in the Aqua10m simulation, a secondary near-equatorial precipitation maximum exists in the summer hemisphere, whose location is more directly constrained by the curvature in the near-surface temperature distribution and, hence, by the boundary layer momentum budget (e.g., Lindzen and Nigam, 1987; Pauluis, 2004). The dynamics of this secondary ITCZ will be discussed elsewhere.

Some caveats are worth mentioning. Our results are based on simulations that are idealized both in terms of the zonally symmetric configuration and the represented physics. It is well known, for instance, that cloud feedbacks play an important role in the quantitative response of the tropical precipitation to a given radiative perturbation and that they are the major source of intermodel spread (e.g., Kang et al., 2009, 2008; Seo et al., 2017). Additionally, in the Aqua0.2m the lower boundary has a thermal inertia that is more representative of values over land than ocean surfaces, allowing

excursions of the convergence zones into subtropical latitudes similar to what is seen in Earth's monsoon regions (e.g., Bordoni and Schneider, 2008). Yet, it differs from land in other important features, such as albedo and limited evaporation, which have nonnegligible effects on the energetics. The relevance of the mechanisms discussed here to monsoonal circulations as well as oceanic regions remains unclear. Analyses of observational data, both in the zonal mean and over oceanic and monsoon sectors, might shed some light on these open questions and will be pursued in future work. Vertical ascending motions that import MSE and have negative GMS are indeed observed over the East Pacific, where shallow circulations exist (e.g., Back and Bretherton, 2006; Zhang et al., 2004). These observed circulations and associated GMS should be reassessed within the atmospheric energy framework to explore their relationship with the ITCZ position and variability.

Finally, in our study we have neglected the possible role of ocean heat transport in seasonal ITCZ migrations. It is now well accepted that the mean northward position of the ITCZ primarily arises because the Atlantic Ocean transports energy from the southern to the northern hemisphere (e.g., Frierson et al., 2013; Marshall et al., 2013). Moreover, theoretical arguments and modeling studies using fully coupled models show that changes in ocean heat transport can dampen the ITCZ response to energetic perturbations (e.g., Green and Marshall, 2017; Hawcroft et al., 2016; Schneider, 2017). Through its impact on SST distributions and cross-equatorial heat transport, ocean dynamics might therefore modify the mechanisms discussed in this study in important ways. An assessment of the impact of seasonally varying ocean heat transport in different basins on seasonal ITCZ shifts deserves further investigation.

Chapter 3

ENERGETIC CONSTRAINTS ON THE ITCZ IN THE OBSERVED SEASONAL CYCLE

Abstract

Energetic arguments have provided useful constraints on the zonally and annually averaged ITCZ position and shifts. Simulations with a seasonal cycle, however, show that on timescales shorter than seasonal, there exists a lag between the energy flux equator (EFE) and the ITCZ and that the ITCZ position is not simply anti-correlated with the cross-equatorial energy transport. One important consequence of these findings is that the tropical Hadley cell can achieve the required energy balance not through shifts in its ascending branch (and hence ITCZ) but through changes in its gross moist stability (GMS), which can in fact become negative as the cell develops a shallow return flow near the mid-to-lower tropospheric moist static energy minimum. Shallow circulations are known to occur in the Eastern Pacific, but their relationship to the ITCZ position and cross-equatorial energy transport has not been previously investigated.

In this study, we explore to what extent similar mechanisms are seen in the observed seasonal cycle both in the zonal mean and in different zonal sectors. In the zonal mean, an offset exists between the ITCZ and the EFE, as the ITCZ is retreating from the northern to the southern hemisphere. At these times of the seasonal cycle, the Hadley cell needs to transport energy northward across the equator, in spite of a northward shifted ITCZ. This occurs as the southern Hadley cell develops a bottom-heavy structure, which forces the boundary between the two Hadley cells to deviate from being vertical and favoring a northward MSE transport. In the Eastern Pacific sector, the existence of two nodes of the meridional energy transport during parts of the seasonal cycle suggests the possibility of negative GMS in the associated overturning circulation. It is shown that, while bottom-heavy vertical velocity profiles favoring shallow return flows at levels of minimum moist static energy exist throughout the year, the bottom heaviness becomes much stronger at times with negative GMS, and weak SSTs and large negative SST Laplacian below the ITCZ. These results suggest that EFE and ITCZ are not related in any simple manner in the course of the seasonal cycle. Conclusions based on energetic arguments also appear to be very sensitive to the degree to which the energy budget

in reanalysis data can be closed.

3.1 Introduction

Idealized simulations with a seasonal cycle show that energetic arguments that provide useful constrains on the zonal and annual mean ITCZ (e.g., Bischoff and Schneider, 2014; Donohoe et al., 2013; Frierson and Hwang, 2012; Hwang et al., 2013; Kang et al., 2009, 2008) fail on shorter timescales (Wei and Bordoni (2018), Chapter 2). More specifically, the energy flux equator (EFE), whose position is primarily determined by the insolation forcing, always leads the ITCZ, whose location is in phase with the lower level temperature and moist static energy. As a result, the EFE and the ITCZ do not always reside on the same side of the equator and the gross moist stability of the Hadley cell in which the ITCZ is embedded can become negative. Negative GMS is achieved through the development of a shallow return flow at levels of minimum MSE. These results are however based on idealized simulations, which, most importantly, lack zonal and hemispheric asymmetries and dynamical coupling with the ocean. Hence, the relevance of these mechanisms for the observed seasonal cycle remains unclear.

Reanalysis data have been used extensively in the literature to understand the energy balance of the climate system and to infer the required atmospheric and oceanic energy transport (e.g., Trenberth and Caron, 2001). Recent work has also explored observed relationships between the ITCZ and energetic diagnostics in reanalyses, both in the annual mean and in the seasonal cycle (e.g., Adam et al., 2016a,b; Donohoe et al., 2014, 2013; Frierson et al., 2013). Importantly, Adam et al. (2016a) and Adam et al. (2016b) show that a lag exists between the EFE and the ITCZ. However, the implications of this lag for the energy transport by the Hadley circulation and changes in its vertical structure (and possibly GMS) have not been explored. It is, for instance, well documented that shallow circulations which import MSE exist throughout the year over the Eastern North Pacific (e.g., Back and Bretherton, 2006, 2009a; Zhang et al., 2004), but no study has so far investigated their relationship and influence on the ITCZ seasonal migrations. This is indeed the goal of this study: by using MERRA 2 reanalysis, we document the relationship between the ITCZ position, the EFE, the overturning circulation vertical structure and the associated energy transport in the course of the observed seasonal cycle, both in the zonal mean and different sectors. We also compare our results with those existing in the literature based on other reanalysis products, and highlight how existing residuals in the mass and MSE budgets might affect the interpretation of emerging results.

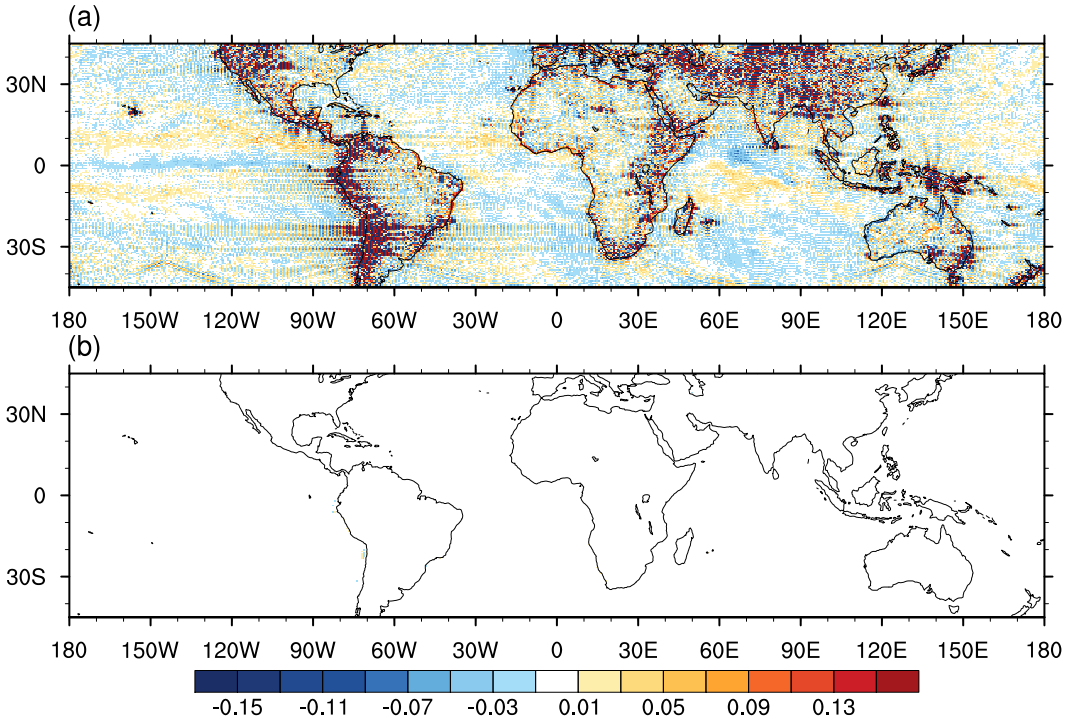

Figure 3.1: The dry mass residual (M_dRES, kg m^{-2} s^{-1}) in the mass mass equation (a) before and (b) after mass adjustment for the MERRA2 data averaged in July, 2016.

3.2 Data and Methods

We use fields from NASA's Modern−Era Retrospective analysis for Research and Applications, Version 2 (MERRA-2) (e.g., Bosilovich et al., 2015; Rienecker et al., 2011), with horizontal resolution of 0.5° (latitude) × 0.625° (longitude) and 3-hourly (atmospheric fields) and 1-hourly (other variables such as surface fluxes and radiation) temporal resolution for years 2002−2016. All data are averaged over 5 days (for a total of 73 pentads) for each year and then multi-year pentad means are computed.

The dry mass budget in MERRA-2, like in other reanalyses, is not closed. As discussed in Trenberth (1991), a barotropic wind adjustment hence needs to be performed to close it. The dry mass budget is

$$\frac{\partial m_d}{\partial t} = \nabla \cdot \frac{1}{g} \int_0^{p_s} (1-q)\boldsymbol{v}\, dp + M_dRES, \tag{3.1}$$

where M_dRES is the residual of the dry mass, which is also equal to the difference between the total mass and moisture residuals. With a barotropic wind adjustment

$\boldsymbol{v_c} = (u_c, v_c)$, the $M_d RES$ disappears and the dry mass equation becomes

$$\frac{\partial m_d}{\partial t} = \nabla \cdot \frac{1}{g} \int_0^{p_s} (1-q)(\boldsymbol{v} - \boldsymbol{v_c}) dp. \tag{3.2}$$

By subtracting Eq. (3.2) from (3.1), the barotropic wind adjustment can be derived as

$$\boldsymbol{v_c} = \frac{\nabla \chi^c}{(p_s - p_t - pw)}, \tag{3.3}$$

where pw is precipitable water (i.e., $pw = \int_0^{p_s} q dp/g$), p_s is surface pressure, p_t the top level pressure, and $\nabla^2 \chi^c = M_d RES$.

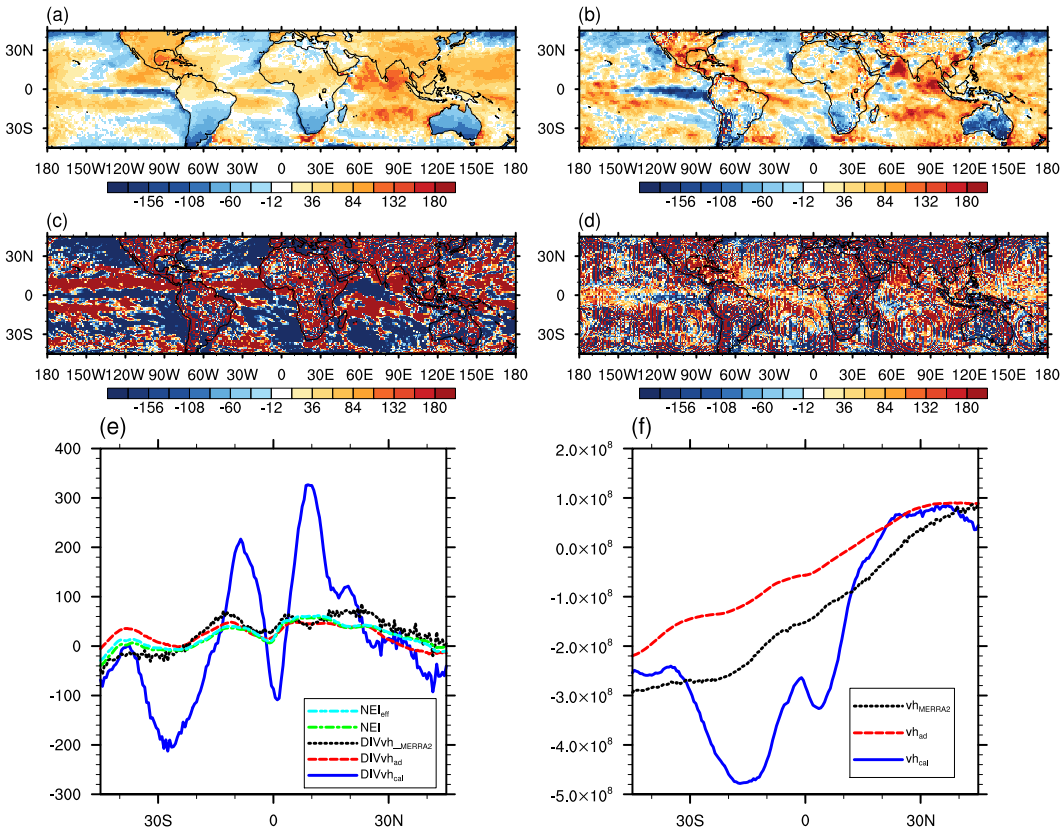

Figure 3.2: Monthly averaged (a) NEI, divergence of (b) adjusted meridional MSE flux ($\langle vh \rangle$), (c) unadjusted $\langle vh \rangle$, and (d) $\langle vh \rangle$ calculated from MERRA2 vertically integrated output (W m^{-2}) for July, 2016. (e) Zonally averaged effective NEI (cyan dashed line, W m^{-2}), NEI (green dashed-dotted line), divergence of $\langle vh \rangle$ calculated from MERRA2 (black dotted), adjusted $\langle vh \rangle$ (red dashed line), and unadjusted $\langle vh \rangle$ (blue solid line). (f) Zonally averaged meridional energy flux output from MERRA2 (black dotted, W m^{-1}), adjusted $\langle vh \rangle$ (red dashed line), and unadjusted $\langle vh \rangle$ (blue solid line).

The mass adjustment is calculated from 6-hourly data on pressure levels (42 layers), which allows us to compute the vertically integrated total MSE flux at pentad

temporal resolution. In Fig. 3.1, we show how mass adjustment significantly reduces the $M_d RES$ over monthly time scales. The residual of both the zonal mean and local MSE budget is also reduced significantly compared to the one computed without mass adjustment or from the vertically integrated MSE flux directly available from MERRA-2 (Fig. 3.2). Please note that the vertically integrated MSE flux we show here is the divergent component of the flux, which is the one from the circulation component that contributes to precipitation.

3.3 General Features of the ITCZ, Circulation and the Energy Flux

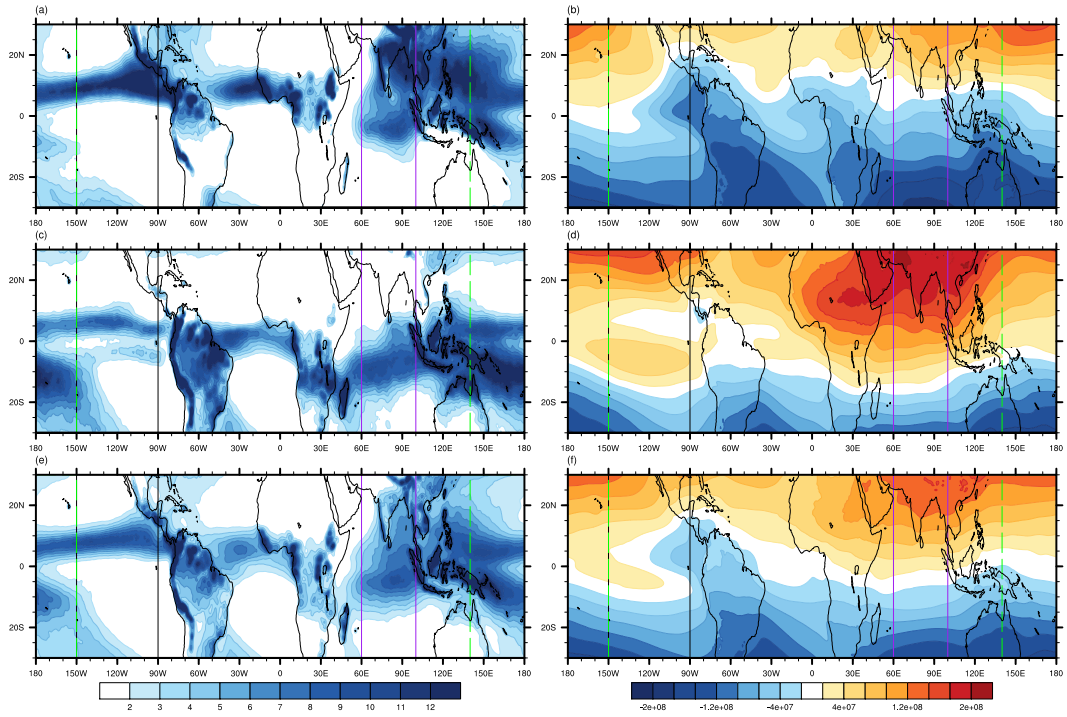

Figure 3.3: (a) JAS, (c) JFM, and (e) annual mean precipitation from MERRA2 reanalysis data averaged over the years 2002–2016 (mm day^{-1}). (b, d, f) Same seasonal mean as (a, c, e), but for the divergent component of the vertically integrated meridional MSE flux (W m^{-1}). Vertical lines indicate individual sectors selected for following analyses: East Pacific (black), West Pacific (dashed green) and Indian (purple).

Fig. 3.3 shows the precipitation and energy flux distribution in tropical regions for NH summer (JAS), winter (JFM), and in the annual mean. While both the EFE and ITCZ tend to migrate northward (southward) in the NH summer (winter) relative to their annual mean position at every longitude, they are not collocated. Strong zonal variations are also seen in both their seasonal and annual means. For example, over the East Pacific the ITCZ remains in the NH even during NH winter, with the

development of a secondary ITCZ south of the equator around March. Over India and Africa, regional ITCZs more clearly follow the seasonal cycle of insolation, with excursions across the equator into the summer hemispheres. Note however how near equatorial precipitation over the Southern Indian Ocean is evident even during NH summer, when the most active convection is found over South-East Asia as the monsoon develops there. Over the Western Pacific, on the other hand, strong convection develops over the warm pool and over the Southern Pacific Convergence Zone (SPCZ) in the SH. The latter is particularly strong in SH summer.

The EFE also shows strong zonal asymmetries, with times during the seasonal cycle at which the energy transport vanishes at two different latitudes for a given longitude. As discussed in Bischoff and Schneider (2016) and Adam et al. (2016b), these EFE bifurcations occur over latitudes where the NEI becomes negative (that is, where there is convergence of MSE flux). Interestingly, EFE bifurcations do not always correspond to ITCZ bifurcations (or a double ITCZ), nor do their latitudes feature a clear colocation with the positions of the double ITCZ. We next detail seasonal evolution of both zonal mean and sector-mean quantities.

Zonal mean

In the zonal mean, as well documented by many previous studies, the ITCZ migrates seasonally between the two hemispheres and in the annual mean is located at around 6°N (Fig. 3.4). For the ITCZ metric defined in Adam et al. (2016a) and used in Chapter 3 ($\phi_{P_{max,smth}}$), the ITCZ resides longer in the NH and migrates somewhat rapidly into the SH around January. This results from the development of the SH ITCZ in the Eastern Pacific, a strengthening of the SPCZ in the Western Pacific, and a southward shift into the SH of the ITCZ in the African and Indian sectors.

The ITCZ generally coevolves with the zonal mean near-surface MSE maximum migration and is located slightly equatorward of it (Fig. 3.5c), consistent with convective quasi-equilibrium (e.g., Emanuel, 1995; Privé and Plumb, 2007a). It is interesting to note how the evolution of the zonal mean MSE maximum results from a combination of temperature and moisture, with temperature maximizing poleward than both moisture and MSE during NH summer because of the presence of land masses (Fig. 3.5a, c, e). The offset between temperature and moisture disappears when we only take a zonal mean over ocean (Fig. 3.5b, d, f) where the near-surface moisture tracks closely the near-surface temperature.

While tropical precipitation is dictated by surface thermodynamic quantities, re-

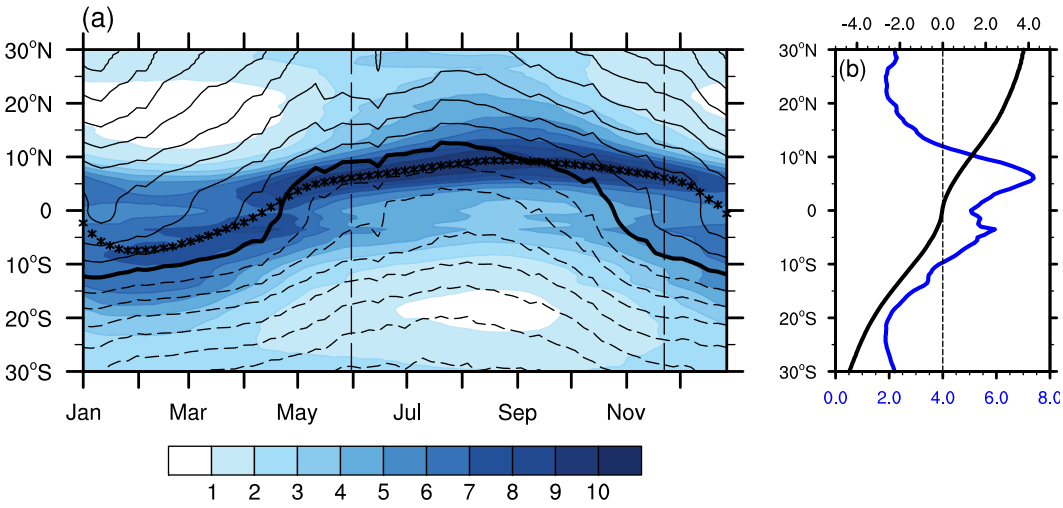

Figure 3.4: Seasonal evolution of (a) zonal mean precipitation (shading, mm day^{-1}) and vertically integrated meridional energy flux (contours, W m^{-1}). Solid (dashed) contours indicate positive (negative) values and thick black contour the zero value. The contour spacing is 2×10^7W m^{-1}. (b) Annual and zonal mean precipitation (blue line, mm day^{-1}) and meridional energy transport (black line, PW).

maining in the NH for a large portion of the seasonal cycle, the EFE follows the seasonal evolution of solar insolation and spends almost equal amounts of time in the two hemispheres. Unlike what is seen in the idealized simulations, in the observations the temporal relationship between the EFE and the ITCZ cannot therefore simply be described as a lag, because of the ITCZ evolution differs from an annual harmonic [1] (Fig. 3.4, Fig. 3.5c).

Despite being more complex than what is seen in the idealized simulations, a temporal and spatial offset between the EFE and the ITCZ still raises the question of how the overturning cell in which the ITCZ is embedded achieves negative GMS over the regions between the EFE and the ITCZ. In fact, at any time at which the EFE and the ITCZ reside on opposite sides of the equator, the cross-equatorial overturning cell transports energy in the direction of the lower-level. We therefore select two pentads with same ITCZ location but different EFEs at which the southern cell is expanding and retreating into the NH, respectively (vertical dashed lines in Fig. 3.4, around May 31– Jun. 4 and Nov. 22–26), and compare the associated circulation structure. The overturning circulation and the corresponding vertical profiles of meridional wind and MSE at the equator are shown in Fig. 3.6. Other

[1] For reference, in Fig. 3.5, we still show the fit to the EFE and ITCZ based on an annual harmonic. But it is to be understood that the relationship between EFE and ITCZ cannot just be interpreted as arising from a different phase lag to a forcing with the same frequency.

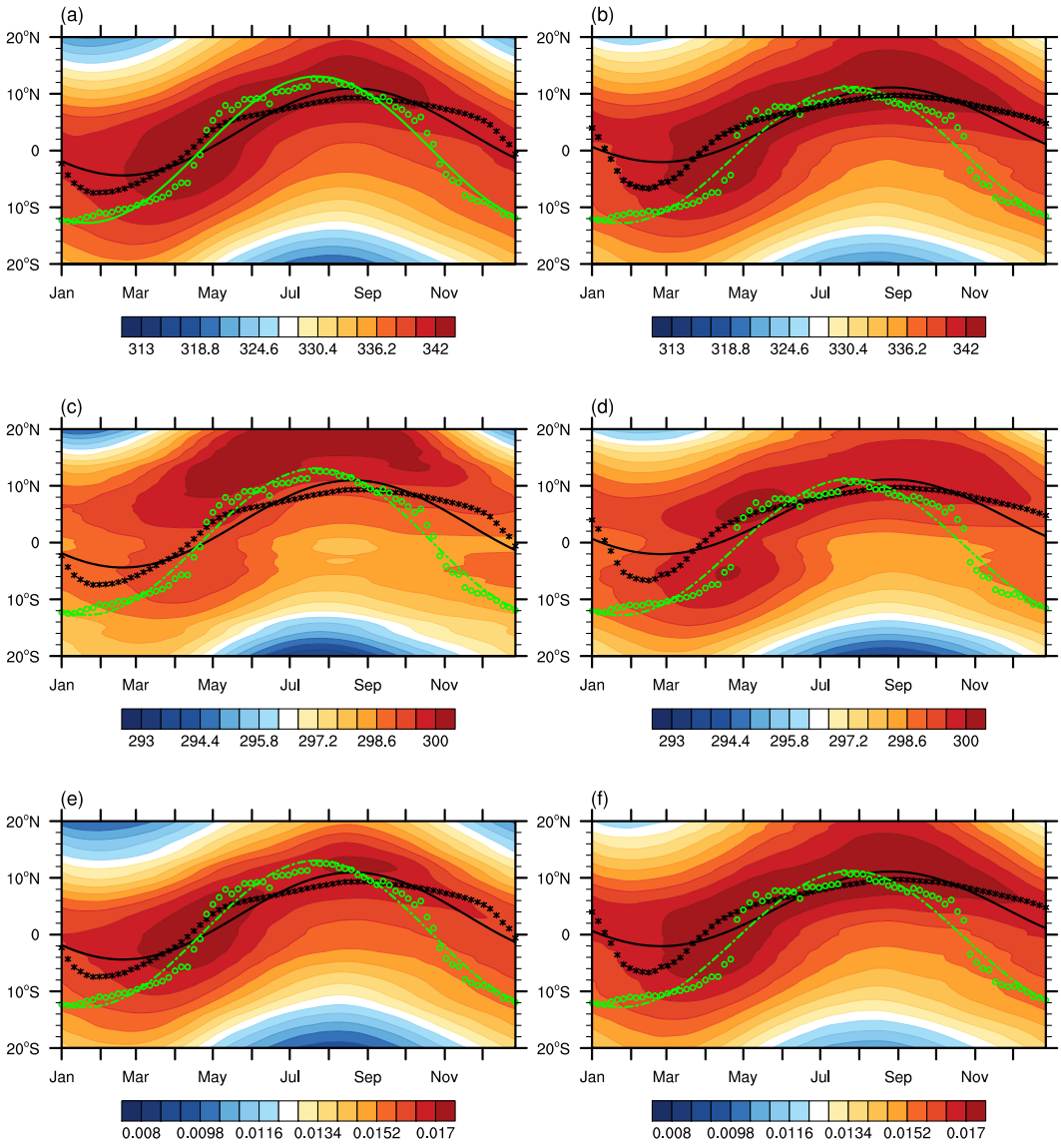

Figure 3.5: Seasonal evolution of zonal mean (a) MSE (K), (c) temperature (K), and (e) moisture (kg kg^{-1}) at the lowest model level (σ=0.985) for MERRA2 reanalysis data averaged over the years 2002−2016. (b, d, f) Same as (a, c, e), but for ocean. Green circles are zonal mean EFE and the asterisks are the ITCZ location ($\phi_{P_{max,smth}}$) for (a, c, e) all data and (b, d, f) ocean.

than being much weaker than the winter cell in its expanding phase, the retreating cell is much broader at lower levels than at upper levels. This structure allows the development of a shallow meridional flow near the minimum MSE, which favors negative GMS.

This structure, while explaining how the required energy transport is achieved in the zonal mean, is not representative of a dominant structure at all longitudes but in fact

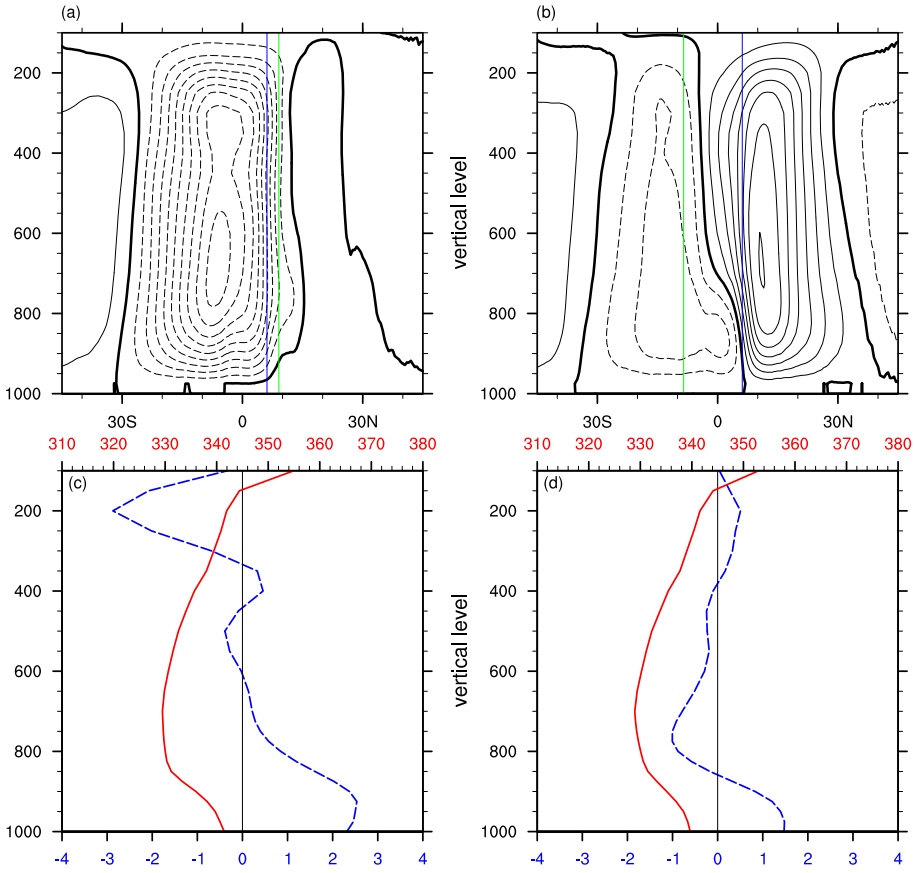

Figure 3.6: Meridional mass streamfunction (contour, interval 2×10^{10} kg s^{-1}, positive (negative) value corresponding to clockwise (counter-clockwise) circulation) for (a) May 31–Jun. 4 and (b) Nov. 22–26. Solid (dashed) contours indicate positive (negative) values and thick black contours the zero value. Blue vertical line indicates the $\phi_{P_{max,smth}}$ and the green vertical line the ϕ_{EFE}. Vertical profiles of the MSE (red solid line, K) and meridional wind (blue dashed line, m s^{-1}) at the equator on (c) May 31–Jun. 4 and (d) Nov. 22–26.

arises from different structures in different sectors. The distorted boundary between the two Hadley cells results from a more bottom-heavy overturning cell in the Pacific sector with ascending motion in the NH, and a more top-heavy overturning cell with ascending motion in the SH and near the equator over the western Pacific and Indian sectors (Fig. 3.7). This motivates us to look more closely at regional differences in different sectors in the next section.

Eastern Pacific sector

Due to strong zonal variations, the evolution of the EFE and the ITCZ in different sectors have very different structures and relationships. In the Eastern Pacific

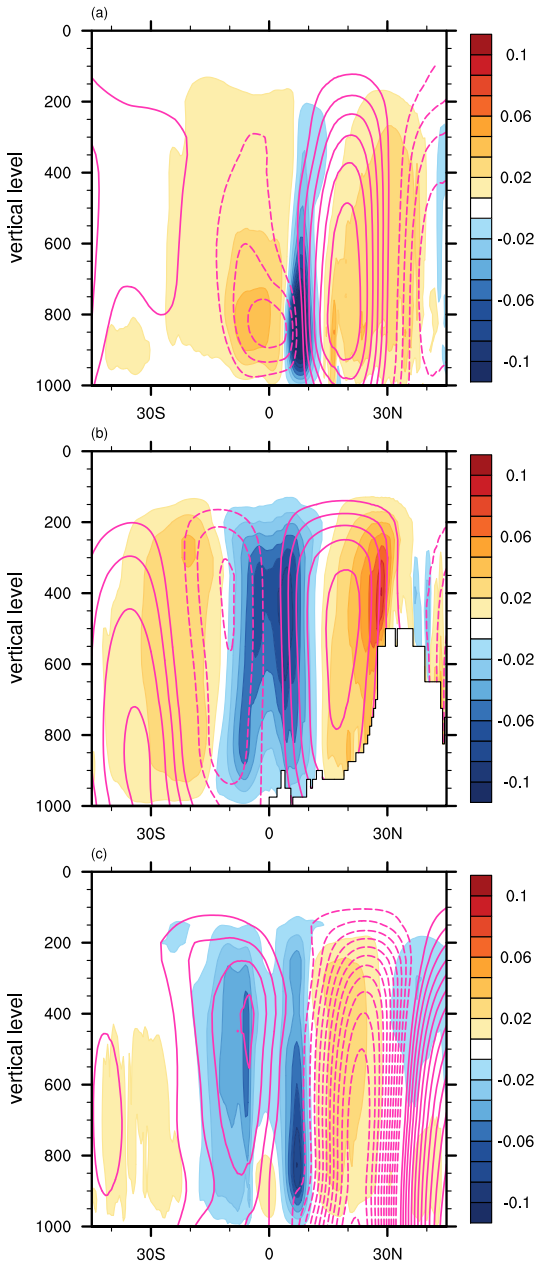

Figure 3.7: Sector mean meridional mass streamfunction (contour, interval 10^{10} kg s^{-1}) for 15 days (3 pentads) average near Nov. 22−26 in the (a) Eastern Pacific, (b) Indian, and (c) Western Pacific sectors. Solid (dashed) maroon contours indicate positive (negative) values. Positive (negative) contours indicate northward (southward) meridional flow at upper levels, and oppositely directed flows at levels below the streamfunction maximum (minimum). The shading shows vertical pressure velocity (Pa s^{-1}).

sector, the specific longitudinal range is chosen to minimize the contribution from land masses.

In the Eastern Pacific sector (150°W − 90°W, indicated within the black vertical lines in Fig. 3.3), the precipitation stays in the NH throughout the year while a secondary ITCZ develops around March in the SH (Fig. 3.8). The ITCZ in the NH has a temporally asymmetric evolution, being stronger as the ITCZ is expanding into the NH than as it is retreating from it. Given that, similar to what is seen in the zonal mean, the ITCZ does not evolve at the same frequency as the annual cycle of insolation, the temporal relationship between the EFE and the ITCZ cannot simply be described as a lag. Also, because of the double EFE in this sector, even with a similar EFE location, the energy transport nearby can be very different. For example, for the Jun. and Nov. pentad (indicated by the vertical black dashed lines in Fig. 3.9), with the same ITCZ and similar EFE, the southern cell corresponds to very different energy transport. In the Jun. pentad, the expanding cross-equatorial cell transports energy to the south, while the cross-equatorial cell in the Nov. pentad tends to transport no or some energy to the north, which corresponds to zero or negative GMS.

Fig. 3.9 shows the overturning cell structure for the Jun. and Nov. pentads mentioned earlier with the same ITCZ but different energy transport distribution. Within the Eastern Pacific sector, previous work has shown that a shallow circulation tends to persist throughout the year (e.g., Back and Bretherton, 2006; Zhang et al., 2004). However, we do see differences in the circulation structure between the expanding and retreating phases. More specifically, in the expanding phase, the shallow return flow extends over a deeper layer within the mid troposphere and there exists a stronger return flow at upper levels, which results in energy being transported in the same direction as the upper level flow (Fig. 3.9a, c). The retreating cross-equatorial cell, however, has a shallower and stronger shallow return flow and, more importantly, a much weaker flow at upper levels, which results in an overturning circulation and vertical velocity that have clear bottom-heavy vertical structures (Fig. 3.9b, d). This clear bottom heaviness is what favors a more negative GMS at this time of the year near the equator.

To explore the possible reasons for these seasonal differences in the overturning cell structure, the evolutions of the surface temperature, its gradient and its Laplacian are calculated. We find that the SSTs are much weaker and their Laplacian is much stronger near the ITCZ as it is retreating from the NH around Nov. This is consistent with arguments by Back and Bretherton (2009a) and Lindzen and Nigam (1987), that link a more negative SST Laplacian and weaker SST to more bottom

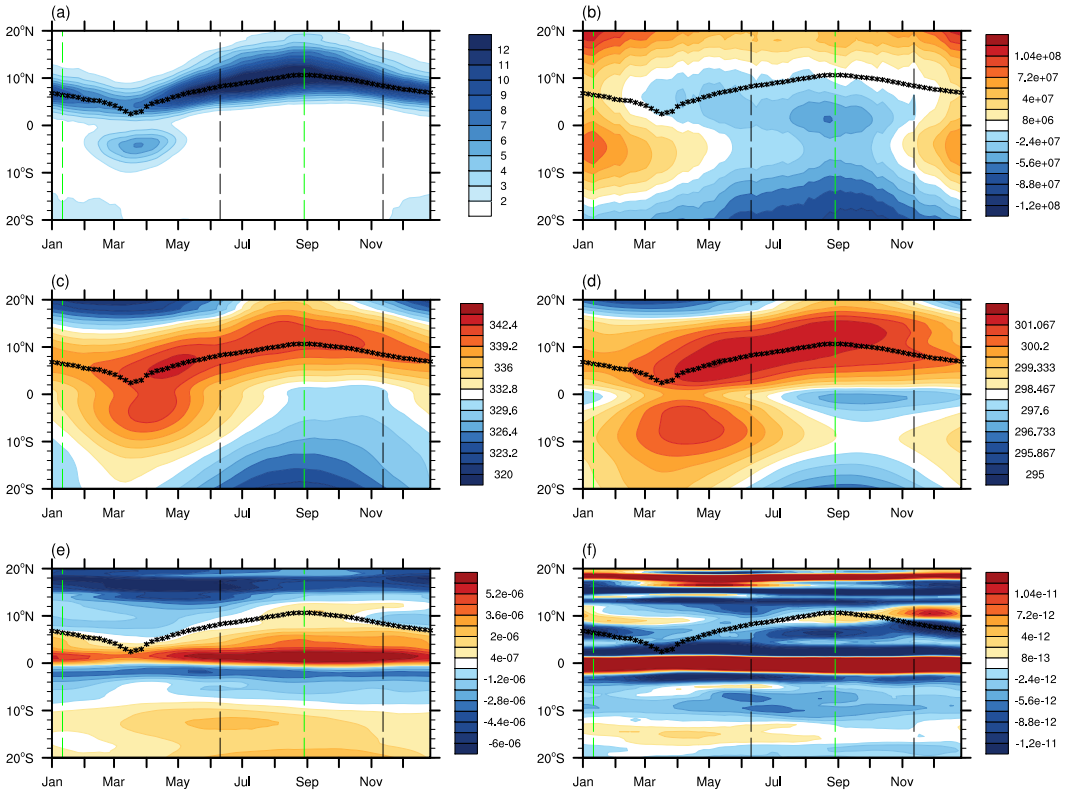

Figure 3.8: Seasonal evolution of zonal mean (a) precipitation (mm day^{-1}), (b) meridional energy flux (W m^{-1}), (c) surface MSE (K), (d) skin temperature, (e) meridional skin temperature gradient (K m^{-1}), and (d) meridional Laplacian of the skin temperature (K m^{-2}) in the Eastern Pacific sector (150°W −90°W). The black (green) vertical dashed lines indicate Jun. 15−19 and Nov. 17−21 (Jan. 16−20 and Aug. 29−Sep. 2), respectively, which are compared in Fig. 3.9 (Fig. 3.10). The asterisks are $\phi_{P_{max,smth}}$.

heavy convection due to the corresponding stronger lower level convergence and hindrance to the development of deep convection, respectively.

If we also compare pentads corresponding to times of maximum southward and northward energy transport south of the ITCZ (Jan. 16−20 and Aug. 29−Sep. 2, respectively, indicated by the vertical green dashed lines in Fig. 3.8), we see a similar difference in bottom heaviness of the associated circulation, with a more bottom-heavy profile around January favoring a northward energy transport in the southern cell (Fig. 3.10).

3.4 Discussions and Conclusions

In this study, we have analyzed the seasonal evolution of the ITCZ, the structure of the overturning circulation in which the ITCZ is embedded and their relationships

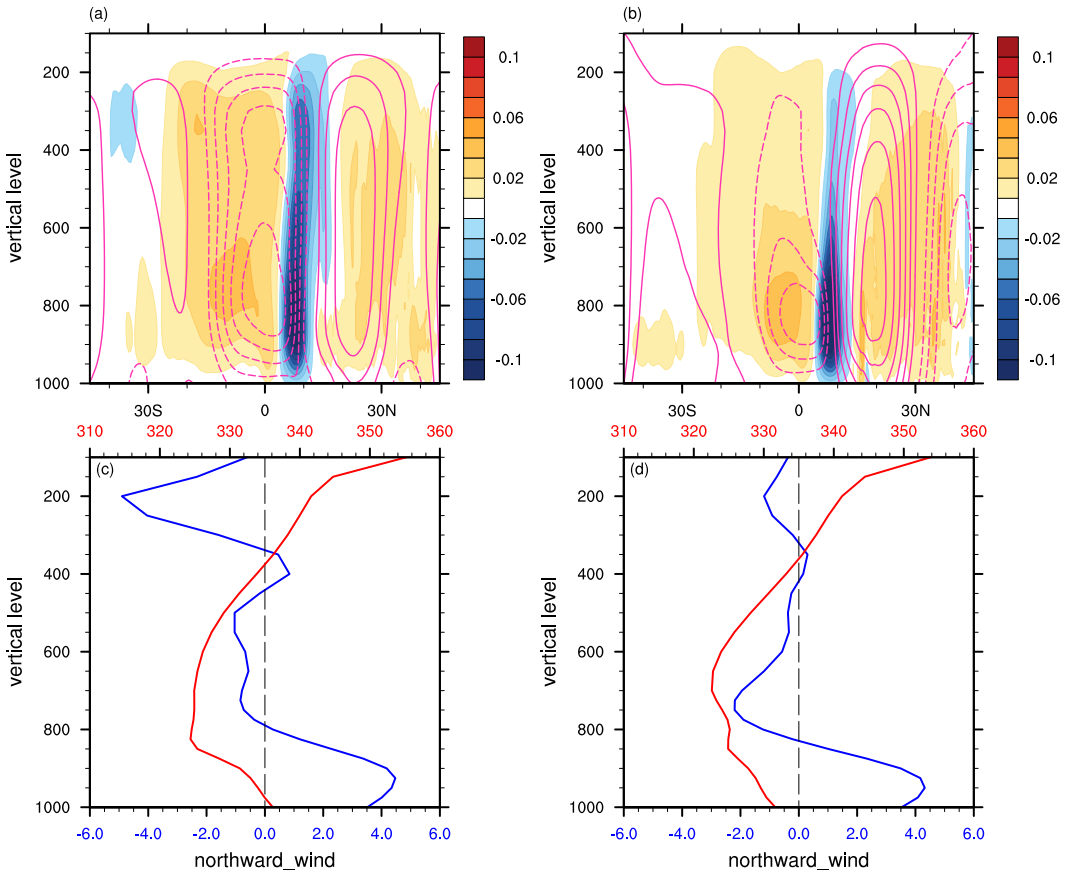

Figure 3.9: Same as Fig. 3.7a but for 15 days average around (a) Jun. 15−19 and (c) Nov. 17−21 in the Eastern Pacific sector. Vertical profiles of the MSE (red, K) and meridional wind (blue, m s^{-1}) at the equator for 15 days average around (c) Jun. 15−19 and (d) Nov. 17−21. The vertical dashed line indicates zero value for wind speed.

to energetic variables. While the EFE and the ITCZ tend to coevolve during the seasonal cycle, there is a clear offset between the two, with strong zonal variations. Similarly to what we proposed in Chapter 2, EFE and ITCZ on seasonal and shorter time scales respond differently to the seasonal cycle of insolation and are not necessarily collocated. More specifically, the required energy balance is not always achieved through the Hadley cell shifting its ascending branch to follow the EFE, but and associated efficiency of energy transport. This pathway allows commonly held relationships between the ITCZ, EFE and cross-equatorial energy transport to break down on seasonal timescales.

While in the idealized simulations discussed in Chapter 2 the temporal relationship between the ITCZ and the EFE can be described as a lag, in observations this

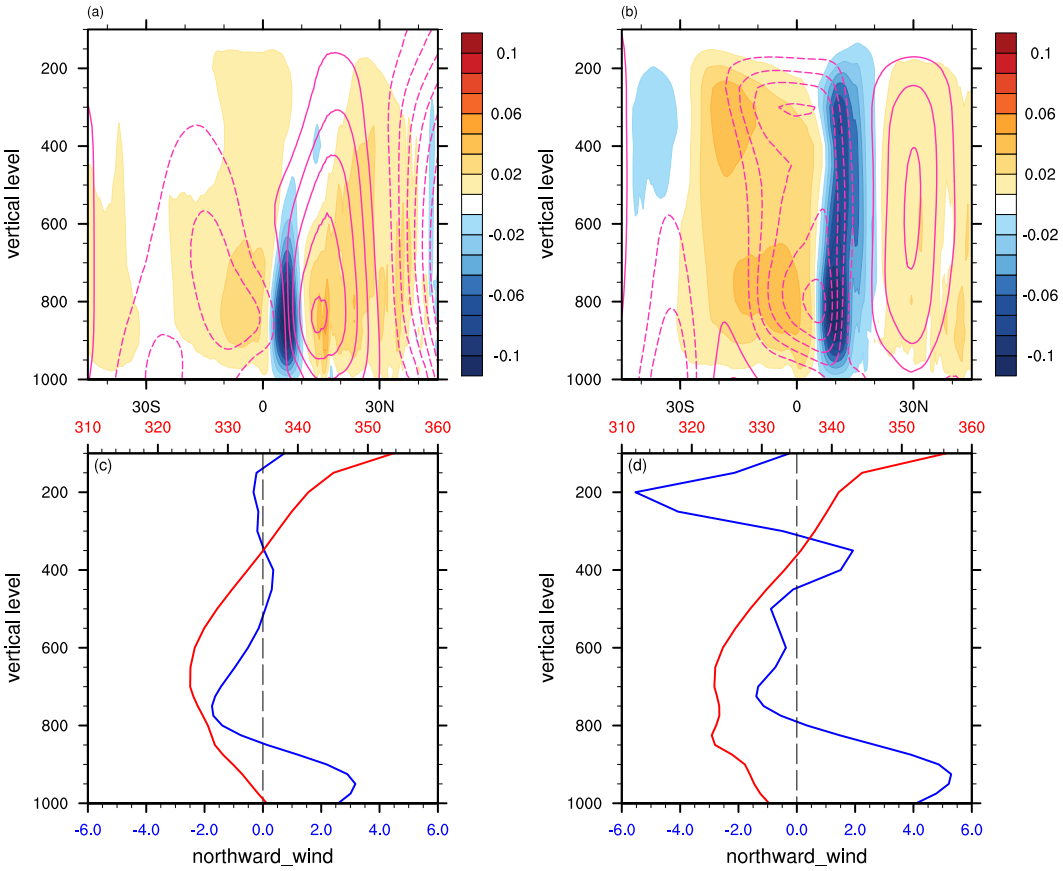

Figure 3.10: Same as Fig. 3.9, but for (a, c) Jan. 16–20 and (b, d) Aug. 29–Sep. 2.

relationship is complicated by the fact that both the ITCZ and the EFE do not evolve just following the period of the annual harmonic. A clear offset however exists, raising the question as to how the required energy balance is achieved as the EFE and the ITCZ reside on opposite sides of the equator or when the energy flux distribution is not monotonic around the EFE.

In the zonal mean, the ITCZ resides in the NH for most of the seasonal cycle, while the EFE spends around equal times in both hemispheres. As the EFE retreats from the NH to the SH, while the ITCZ remains north of the equator, the associated Hadley circulation must transport energy in the direction of its lower rather than its upper branch, with a negative GMS. This occurs as the Hadley cell develops a bottom-heavy structure, with a distorted diving boundary between the two Hadley cells, which is in the NH at lower levels and in the SH at upper levels. This results in a shallow meridional return flow that favors negative GMS. This Hadley cell structure results from strong zonal differences in the overturning structure, with a bottom-heavy cross-equatorial cell with ascending branch in the NH over the Eastern Pacific

and a deeper overturning with ascending branch in the SH mainly over other sectors, like the Indian and Western Pacific sectors. While bottom-heavy convection exists most of the time throughout the year in the Eastern Pacific, the bottom heaviness at times at which ITCZ migrates from the NH to SH is much stronger, favoring a more negative GMS at these times. This stronger bottom heaviness seems to be associated with weaker SSTs and stronger SST Laplacian.

It is worth noting that based on our calculations, in the annual mean, the zonal mean EFE is at the equator, while the ITCZ is 6°N of the equator (Fig. 3.4). The corresponding overturning cell structure is shown in Fig. 3.11, in which the weakly distorted boundary between the two cells could be favoring the offset between the precipitation and the EFE. These results are at odds with ones reported elsewhere in the literature, which show southward cross-equatorial energy transport consistent with a northward shifted position of the ITCZ (e.g., Adam et al., 2016a; Frierson et al., 2013; Marshall et al., 2013; Schneider et al., 2014), and might be related to remaining residuals in the MSE budget, after our mass flux corrections in Eq. (3.3). This highlights difficulties in closing the MSE budgets from reanalyses and suggests that conclusions based on energetic arguments need to be interpreted with caution.

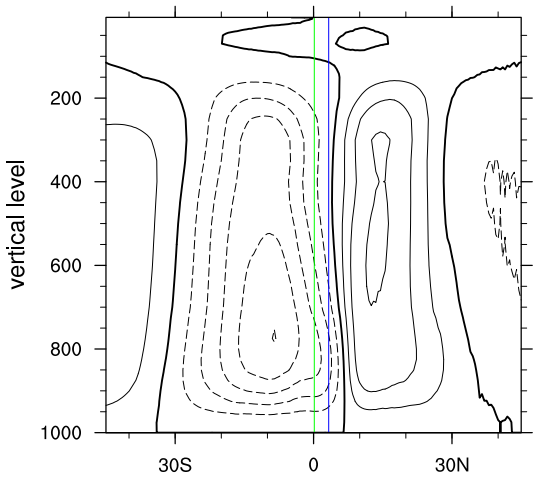

Figure 3.11: Same as Fig. 3.6, but for zonal and annual mean.

That the relationship between the ITCZ, the associated overturning circulation, the EFE and cross-equatorial energy transport during the seasonal cycle is much more complex in the observations than in idealized aquaplanet simulations does not come as a surprise. The aquaplanet simulations in fact neglect processes that have nonnegligible impacts on the energetics, such as zonal asymmetries induced by land-sea contrast and other asymmetries in the lower boundary, and non-represented

physical processes such as ocean circulation and radiative feedbacks. Due to the complexities existing in the reanalysis data, the gap between them and the idealized simulations is large. It will be useful to conduct simulations that, by progressively increasing complexity, can provide increased understanding of processes that control the seasonal cycle of the ITCZ and its relation to energetic constraints.

Chapter 4

ON THE ROLE OF THE AFRICAN TOPOGRAPHY IN THE SOUTH ASIAN MONSOON

Ho-Hsuan Wei and Simona Bordoni (2016), On the Role of the African Topography in the South Asian Monsoon. *Journal of the Atmospheric Sciences*, 73(8): 3197–3212. DOI: 10.1175/JAS-D-15-0182.1

Abstract

The Somali jet, a strong low-level cross-equatorial flow concentrated in a narrow longitudinal band near the coast of Somalia, is a key feature of the South Asian monsoon (SAM) circulation. Previous work has emphasized the role of the East African Highlands in strengthening and concentrating the jet. However, the fundamental dynamics of the jet remains debated, as does its relation to the SAM precipitation. In this study, numerical experiments with modified topography over Africa are conducted with the GFDL AM2.1 general circulation model (GCM), to examine the influence of topography on the Somali jet and the SAM precipitation. We find that when the African topography is removed, the SAM precipitation moderately increases in spite of a weakening of the cross-equatorial Somali jet. The counter-intuitive precipitation increase is related to lower-level cyclonic wind anomalies, and associated meridional moisture convergence, which develop over the Arabian Sea in the absence of the African topography. Potential vorticity (PV) budget analyses along particle trajectories show that this cyclonic anomaly primarily arises because, in the absence of the blocking effect by the African topography and with weaker cross-equatorial flow, air particles originate from higher latitudes with larger background planetary vorticity and thus larger PV.

4.1 Introduction

The South Asian Monsoon (SAM) is the southern part of the Asian monsoon system, the largest scale monsoon in the Earth′s atmosphere. The monsoon brings rain that is concentrated in the summer to densely populated and rapidly growing regions, such as India and neighboring countries. Traditionally, the SAM has been interpreted as a large-scale sea breeze circulation driven by contrast in thermal

properties between the Indian subcontinent and the surrounding ocean (e.g., Meehl, 1994; Webster, 1987; Wu et al., 2012). However, recent theoretical advances suggest that the SAM should be more generally viewed as the regional manifestation of the seasonal migration of the Intertropical Convergence Zone (ITCZ) into the summer subtropical continents (e.g., Gadgil, 2003). The associated thermally direct circulation is characterized by ascending motion in the summer hemisphere subtropics, opposite cross-equatorial flows at lower and upper levels, and descending motion in the winter hemisphere (e.g., Nie et al., 2010), giving rise to a reversed meridional temperature gradient and, by thermal wind balance, an easterly vertical wind shear in the summer hemisphere (e.g., Li and Yanai, 1996). At lower levels, westerly winds dominate in the summer hemisphere over the Indian Ocean, consistent with the Coriolis force on the cross-equatorial flow approximately balancing the drag in near-surface zonal winds (e.g., Bordoni and Schneider, 2008), while easterlies develop at upper levels. The strong precipitation, the displacement into the northern hemisphere (NH) of the upper-tropospheric temperature maximum, and reversal of lower-level winds from easterly to westerly over the Indian Ocean in the NH are all distinctive features of the SAM in boreal summer.

Upstream of the lower-level westerlies, a strong cross-equatorial jet develops near the east coast of Africa. This jet, referred to in the literature as the Somali jet, flows along the East African Highlands (EAH), having a core located at about 1.5 km above sea level, equatorial mean wind speed of around 25 m s^{-1}, and maximum wind speed as large as 50 m s^{-1} (Findlater, 1969). The Somali jet is estimated to contribute up to half of the mass flux crossing the equator during the Asian summer monsoon season. After crossing the equator and turning eastward in the Arabian Sea, the jet brings into the Indian subcontinent moisture from the warm ocean, with around $60 - 80\%$ of the moisture estimated to originate from the southern hemisphere (SH) (Hoskins and Rodwell, 1995).

The Somali jet results from cross-equatorial flow developing in response to the ITCZ displacement in the NH subtropics, and its dynamics has been described as analogous to those of western boundary currents in the ocean (e.g., Anderson, 1976). The EAH have been argued to be essential for the spatial concentration and strength of the cross-equatorial flow. Krishnamurti et al. (1976) used a one-level primitive equation model to show that the East African and Madagascar mountains, the land-sea contrast, and the beta effect are all necessary to simulate a Somali jet similar to what is seen in observations. Subsequent studies have explored the

response of linear models with prescribed diabatic heating and have argued that a western boundary (provided by the EAH) is necessary to develop a concentrated cross-equatorial flow (e.g., Paegle and Geisler, 1986; Sashegyi and Geisler, 1987). Rodwell and Hoskins (1995), hereafter RH95, extended these results to a nonlinear, hydrostatic, primitive equation model with linear drag in the lowest two levels and specified orography and diabatic heating. Their analysis shows how the combination of high terrain over East Africa and greater friction there acts as a positive tendency to potential vorticity (PV) that partially cancels the negative PV of air crossing the equator from the SH and allows the flow to concentrate in a jet and remain in the NH, rather than curving back southward and returning into the SH.

Interest in the fundamental dynamics of the Somali jet is motivated by its possible impact on the SAM precipitation through the associated moisture transport. Some early observational studies do support a positive correlation between the strength of the Somali jet and the rainfall intensity over western India (e.g., Findlater, 1969; Halpern and Woiceshyn, 2001). However, no comprehensive observational study has provided further support to the existence of such robust correlation on scales from intraseasonal to interannual using recent higher resolution data. The only multi-year study based on reanalysis (Boos and Emanuel, 2009) indicates that the rapid onset of the SAM is not associated with a rapid strengthening of the Somali jet. This suggests that the relationship between the lower-level cross-equatorial jet and the monsoonal precipitation might be more subtle than generally thought. This is confirmed by recent modeling studies, which show that the removal of the African topography in fact results in an increase rather than a decrease of the monsoonal precipitation over India, despite a weakening of the Somali jet (Chakraborty et al., 2002, 2006, 2009; Slingo et al., 2005).

This discussion highlights how important questions on the impact of the African orography over the SAM remain outstanding: 1) How does topography over Africa affect the strength and spatial structure of the Somali jet? 2) What is the relationship between the cross-equatorial flow and its downstream westerly extension over the Arabian Sea? 3) How are topographically induced changes in lower-level meridional and zonal flow related to the SAM precipitation? In this paper, we will address these questions by performing simulations with a comprehensive general circulation model (GCM) with modified topography over Africa and the Arabian peninsula. The GCM experiments and analysis methods are described in Section 2. In Section 3, we explore how the Somali jet and the precipitation over the SAM region respond to the

removal of the African topography. The dynamics of these changes is explored more in depth and linked to changes in the PV and the larger-scale monsoonal circulation in Section 4. In Section 5, we present results from an additional simulation, in which we remove both the African and Arabian topography, to understand how the absence of an extended topographical wall from Africa into Arabia might affect the monsoon. Conclusions follow in Section 6.

4.2 Methods

The simulations in this study are performed with the Geophysical Fluid Dynamics Lab (GFDL) Atmospheric Model, version 2.1 (AM2.1, Anderson et al. (2004)). AM2.1 uses a finite-volume dynamical core with horizontal resolution of 2.5 degrees in longitude and 2.0 degrees in latitude and 24 vertical levels. Climatologically fixed sea surface temperatures (SSTs) derived from 2 degrees x 2 degrees 49 years (1950 to 1998) monthly mean of Reynolds reconstructed historical SST analysis (Smith et al., 1996) are used as the lower boundary condition. The convection scheme is the relaxed Arakawa-Schubert scheme.

In this study, we primarily discuss two simulations: A control (CTL) simulation where full global topography is retained (Fig. 4.1a) and an experiment simulation in which topography over Africa is removed (NoAf). In the NoAf experiment, topography is removed between 20^{o}W – 35^{o}E, 0^{o}N – 35^{o}N and between 10^{o}E – 50^{o}E, 40^{o}S – 15^{o}N (Fig. 4.1b). The topographic height of the grid points right outside the edge of these boxes is halved to allow for a smoother transition. In Section 5, we also briefly discuss an additional experiment, NoAfArab, in which together with topography over Africa we also remove the Arabian topography. More precisely, in the NoAfArab experiment, topography is removed between 20^{o}W – 40^{o}E, 0^{o}N – 35^{o}N; 10^{o}E – 50^{o}E, 40^{o}S – 15^{o}N; 40^{o}E – 47^{o}E, 15^{o}N – 30^{o}N; and 47^{o}E – 55^{o}E, 15^{o}N – 25^{o}N (Fig. 4.1c). In all these experiments, the orographic gravity wave drag is modified accordingly to modified topography.

The initial conditions for all three experiments are derived from a one-year simulation with standard topography. After the topography height is changed following the one-year simulation, the experiments are integrated for 19 years, and the analyses discussed below are based on the last ten simulated years.

Large-scale budgets, such as the moisture and PV budgets, are analyzed to shed light into mechanisms that are implicated in the precipitation and circulation response to the change of topography. We also perform trajectory analyses, to explore how

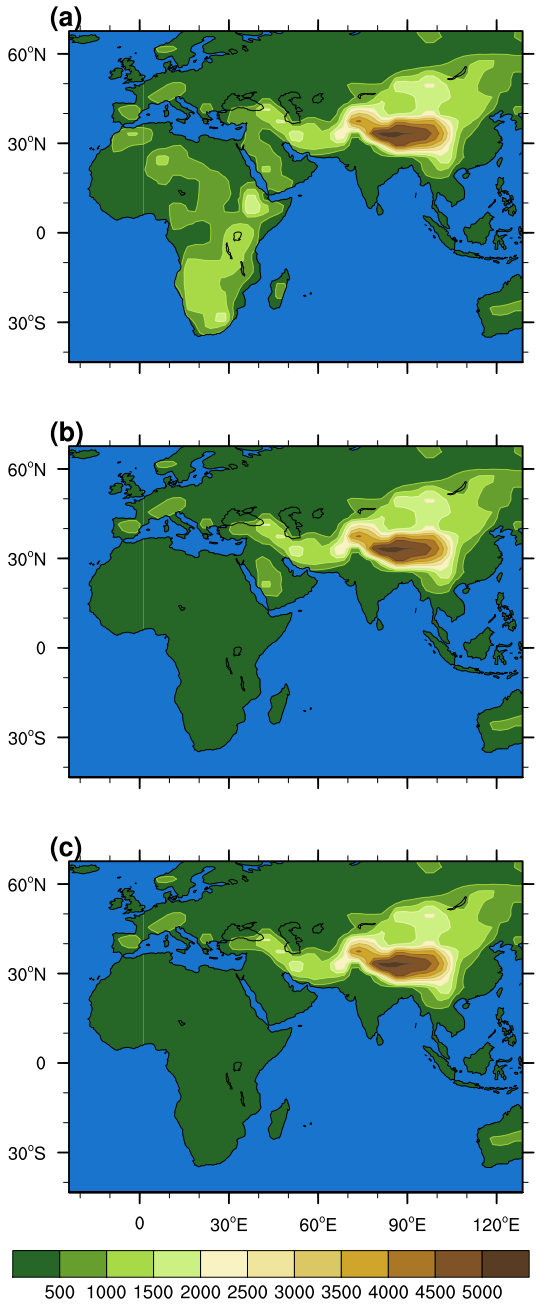

Figure 4.1: Surface height (m) configuration in the (a) CTL, (b) NoAf, and (c) NoAfArab experiments.

topography, possibly through blocking or changes in the Somali jet, impacts the trajectories of air parcels reaching the Indian region, and to more carefully analyze the PV budget from a material perspective. Three-hour wind field data in pressure coordinates are used to compute backward and forward trajectories. The integration time step is three hours as the data output. For each integration, we use the wind

field at the time of calculation, so that the wind field used in the integration is updated at every calculated time step. Once the trajectories have been computed, other variables, including the different terms in the PV analysis, as described in detail in Section 4, are interpolated along the paths. Please note that trajectories are being computed using the 3-dimensional (3D) wind field resolved by the GCM at the grid scale. In regions where convection is active, the resolved mean vertical velocity might underestimate vertical motions due to subgrid-scale convective processes.

In order to consider the conditions representative of the JJA average, which is what we show throughout the paper, eight different integration-starting dates are chosen within July and August at selected locations (e.g., 7/15, 7/20, 7/25, 7/30, 8/5, 8/10, 8/15, 8/20) for the trajectory analyses. In the PV budget analysis, we average these eight integrations, to show average summertime trajectories. The spread of the eight trajectories for the different integration-starting dates increases with integration time, but the trajectories all have similar patterns (not shown).

4.3 Impact of the African Topography on the Somali Jet and SAM Precipitation

The CTL model integration with standard topography produces a SAM with large-scale precipitation and circulation patterns similar to those found in observations (Fig. 4.2). The model precipitation exhibits some bias, with stronger maxima near the western Ghats and the southerly Himalayas, and a weaker and southward shifted maximum over the Bay of Bengal. Other GCMs feature similar simulated bias in this region (e.g., Boos and Kuang, 2010). The cross-equatorial Somali jet, whose response to topography modifications is a primary focus in this paper, is also well captured. The reasonable agreement between the CTL experiment and the observations gives us confidence on the use of AM2.1 as a valid tool to study the impact of the African topography on the SAM.

When topography over Africa is removed in AM2.1, we find that the meridional cross-equatorial flow in the core of the Somali jet weakens, with a reduction of $\sim 30\%$ of the maximum jet strength (Fig. 4.3). While not explicitly discussed there, this weakening appears to be in agreement with simulation results in previous studies (Chakraborty et al., 2002, 2006, 2009; Slingo et al., 2005). A pressure-longitude cross-section at the equator shows that the maximum reduction is at around 800 hPa, slightly above the simulated maximum in CTL at 850 hPa. Additionally, in the NoAf experiment, the cross equatorial flow spreads over the African continent, and the

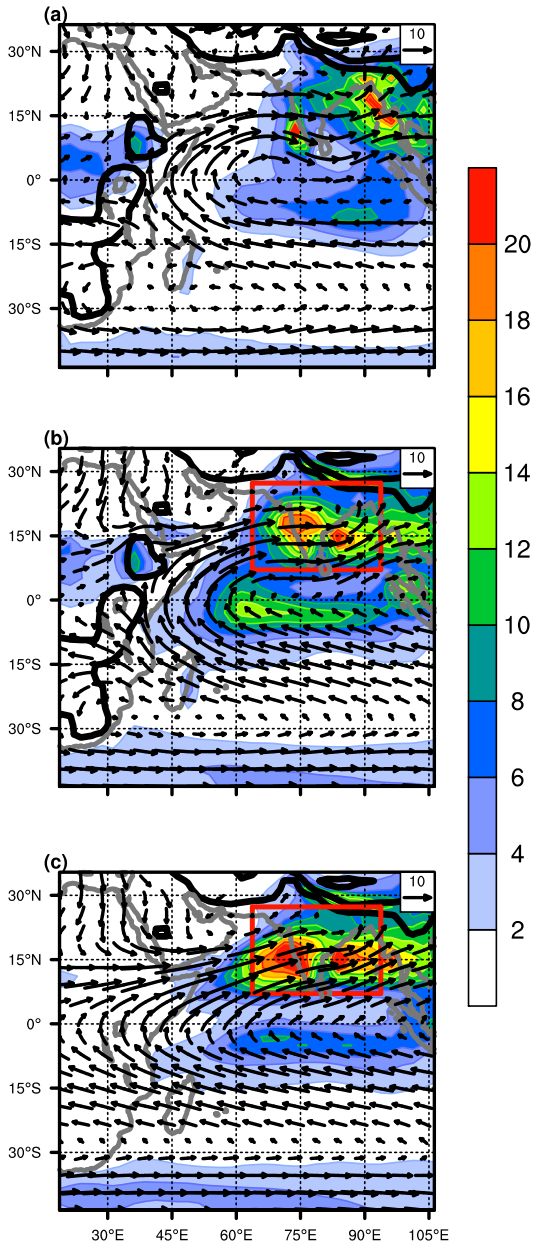

Figure 4.2: JJA precipitation (shading, mm day^{-1}) and 850-hPa winds (vectors, m s^{-1}) in (a) observations, (b) the CTL and (c) NoAf experiments. In panel (a), precipitation is from GPCP v2.2 and winds are from the NCEP reanalysis. Thick black lines indicate the surface height in each simulation (from 1000 m to 5000 m, contour interval 2000 m). The red rectangle indicates the “Indian region", for which accumulated precipitation in the model experiments is shown in Fig. 4.5a.

jet core moves to lower levels and weakens. This finding confirms that the African topography helps accelerate and spatially concentrate the Somali jet. Interestingly, we find that the removal of the African topography causes a positive meridional wind

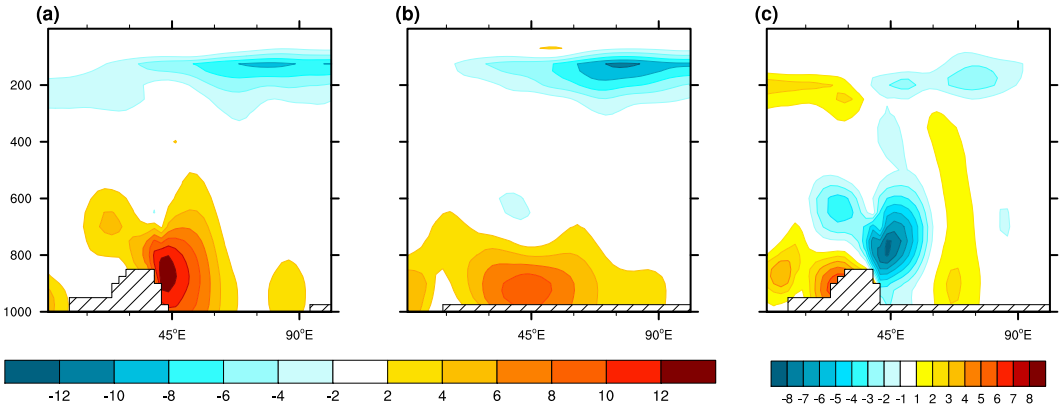

Figure 4.3: Equatorial (1°S – 1°N) pressure-longitude cross-sections of the JJA-average meridional wind (m s^{-1}) in (a) CTL, (b) NoAf and (c) difference between the two.

anomaly over the Arabian Sea north of the equator, where climatological winds are primarily westerlies (Fig. 4.4a and Fig. 4.2b, c). As discussed below, this positive anomaly has an unexpected and important impact on the SAM precipitation.

The weakening of the cross-equatorial flow in the Somali jet core region in the absence of topography over Africa might support the expectation of a similar decrease in monsoonal precipitation, possibly because of decreased moisture transport. Counter-intuitively, we find that precipitation increases almost everywhere in the Indian region, with largest anomalies just west of the Indian subcontinent over the Arabian Sea and smaller anomalies over the Bay of Bengal (Fig. 4.2b, c, and Fig. 4.5b). The “Indian region" here is defined as the broad area within 7.07°N – 27.3°N, 63.75°E – 93.75°E (shown by the red rectangle in Fig. 4.2b, c, and following figures), which includes the Indian subcontinent and neighboring oceans, where precipitation maxima are found in the CTL experiment (Fig. 4.2). The accumulated precipitation in this region, representative of the larger-scale SAM, is shown in Fig. 4.5a for the different numerical experiments: in the NoAf experiment, area-averaged JJA accumulated precipitation increases by $\sim$ 16% compared to the CTL experiment. In the following, we primarily focus on mechanisms responsible for the precipitation response over the Arabian Sea, which are more clearly linked to possible changes in the Somali jet, and associated moisture transport, and have been the focus of previous studies (e.g., Chakraborty et al., 2002, 2006, 2009).

These results therefore demonstrate how changes in the strength of the Somali jet in response to modified topography are not linearly correlated to changes in the SAM precipitation. This is consistent with Boos and Emanuel (2009), who show

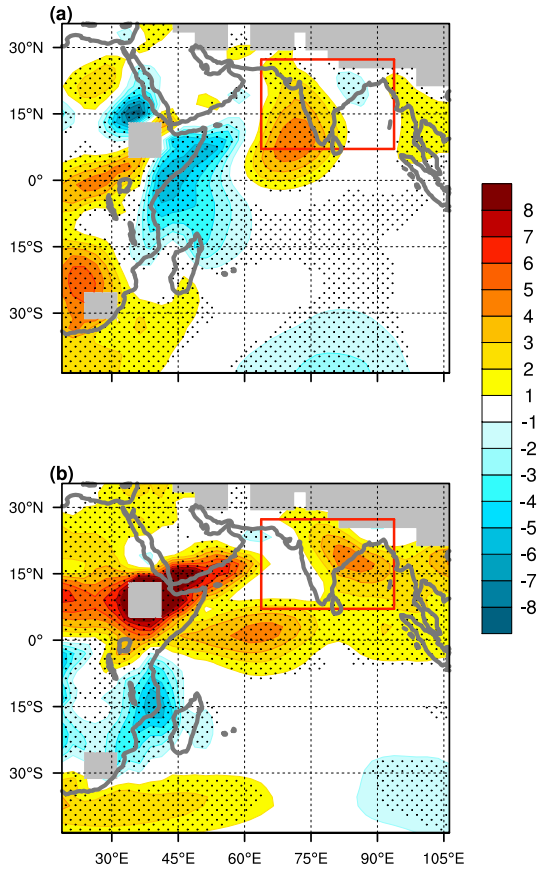

Figure 4.4: Anomalous (NoAf - CTL) (a) meridional and (b) zonal wind at 850 hPa (m s^{-1}). The gray shading indicates regions with no data below 850 hPa. The red box is as in Fig. 4.2. Stippling shows regions where the wind anomalies are statistically significant at the 95% level.

how in the annual cycle the rapid strengthening of the wind over the Arabian Sea at monsoon onset is not accompanied by similarly rapid changes in the cross-equatorial mass transport in the core of the jet near the EAH (between 38.75°E and 48.75°E). They found that these rapid SAM wind changes are instead accompanied by a rapid strengthening of the cross-equatorial mass transport in the periphery of the jet (between 48.75°E and 71.25°E). This suggests that the maximum speed of the cross-equatorial jet, which is influenced by the existence of the African topography, might not be directly related to the SAM precipitation. Following the procedure in Boos and Emanuel (2009), we analyze separately changes in the cross-equatorial mass flux in the topographically-bound core cross-equatorial flow, and in its oceanic periphery region. As shown in Fig. 4.6, in the NoAf experiment, the cross-equatorial mass flux decreases solely in the core region, and remains largely unchanged in the periphery. This suggests that even in the absence of the African topography, the

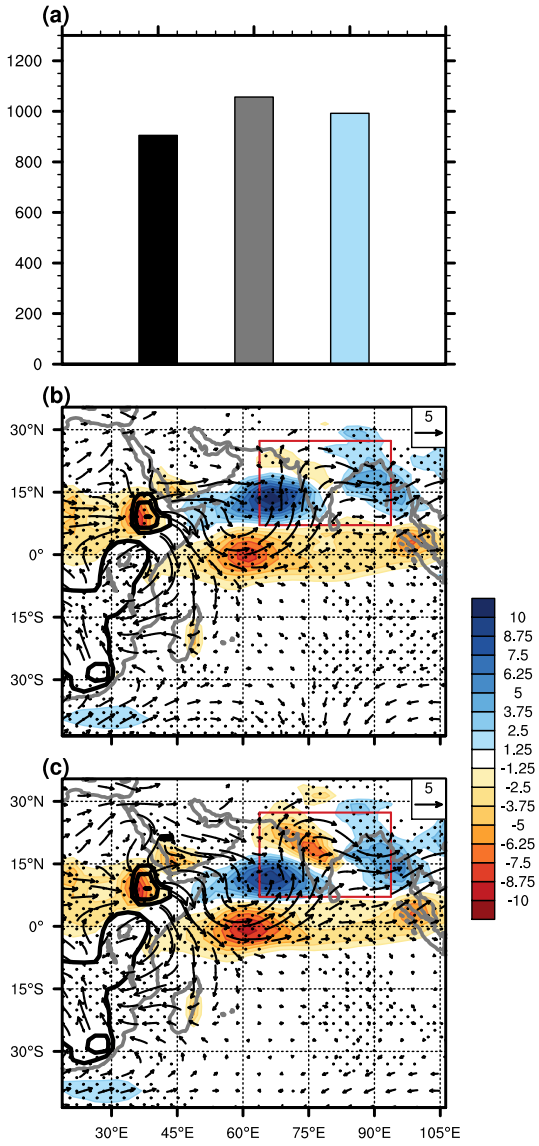

Figure 4.5: (a) Accumulated JJA precipitation (mm) averaged over the Indian region (red rectangle in (b)) in the CTL (black), NoAf (gray), and NoAfArab (light blue) experiments. Anomalous JJA precipitation (shading, mm day^{-1}) and 850-hPa winds (vectors, m s^{-1}) for (b) NoAf - CTL and (c) NoAfArab - CTL. Thick black lines indicate the surface pressure anomalies (contour interval 50 hPa), and hence topography difference, between the two experiments. Stippling shows regions where anomalies are statistically significant at the 95% level.

cross-equatorial mass flux in the periphery region transports sufficient moisture to sustain the monsoon and prevents significant decreases in its precipitation.

While the removal of the African topography does not significantly alter the large-scale patterns of the SAM, it is accompanied by an increase in the overall accu-

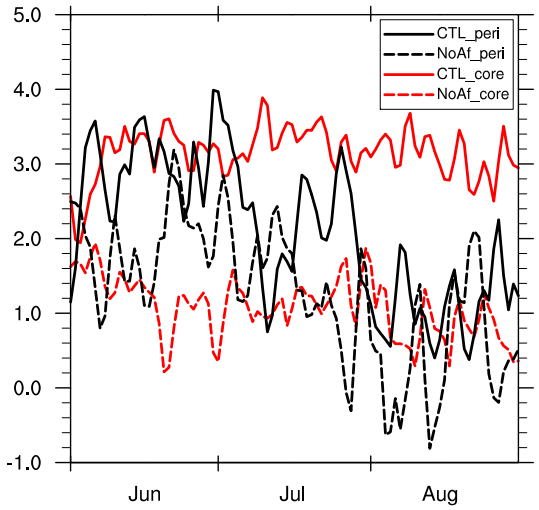

Figure 4.6: Time evolution of the cross-equatorial ($5^oS - 5^oN$) mass flux (10^{10} kg s^{-1}), with red and black lines showing values integrated over the core ($38.75 - 48.75^oE$) and periphery ($48.75 - 71.25^oE$) of the jet region, respectively. The solid lines show the CTL, while the dashed lines show the NoAf experiment.

mulated precipitation that is larger than the standard deviation (10%) associated with the observed monsoon interannual variability and leads to non-negligible regional changes. We interpret these regional changes using the moisture budget, which relates the net precipitation ($P - E$) to the vertically integrated moisture flux convergence. Calling δ the difference between the NoAf and CTL experiments, and decomposing changes in the moisture flux convergence into changes due to winds (the dynamic components, including the convergence and advection terms) and changes due to moisture (the thermodynamic component) as done by a number of previous studies (e.g., Clement et al., 2004; Held and Soden, 2006; Walker et al., 2015), we can write:

$$\delta\overline{P} \approx \delta\overline{E} - \langle\overline{q}\nabla\cdot\delta\overline{\mathbf{v}}\rangle - \langle\delta\overline{\mathbf{v}}\cdot\nabla\overline{q}\rangle - \langle\nabla\cdot[(\delta\overline{q})\overline{\mathbf{v}}]\rangle, \tag{4.1}$$

where $\langle\cdot\rangle$ represents a mass-weighted vertical integral [i.e., $\int(\cdot)dp/g$] and $\overline{(\cdot)}$ a time average. The first term in the right hand side is the change in evaporation, the second term the dynamic convergence term, the third term the dynamic advection term, and the last term the thermodynamic term.

Except for evaporation, which is negligible, the contribution of all terms in Eq. (4.1) to precipitation changes are shown in Fig. 4.7. The residual term is small relative to the other terms, especially compared to the δP term. This small residual also

includes the quadratic term, which is due to covariations in changes of moisture and winds, and the surface term which is due to the additional vertical levels (i.e., pressure interval) in the NoAf experiment where topography is removed. This surface term can be explicitly computed, and we find that its contribution to the moisture flux convergence in the area where topography is removed is small, despite a local increase in moisture there (not shown). Consistent with Chakraborty et al. (2002, 2006, 2009), we find that the largest contribution comes from the dynamic convergence component, that is, changes in precipitation are primarily accounted for by changes in wind convergence. Chakraborty et al. (2009) suggest that in the absence of blocking by the African topography, the westerly flow over Africa would extend eastward into the Arabian Sea and increase the westerlies there. This in turn would favor an increased wind and moisture convergence as the flow approaches the Indian subcontinent. We test this hypothesis by examining how both the westerly flow and air parcel trajectories are modified in the absence of the African topography. When comparing forward trajectories for particles originating over Africa at 850 hPa in the CTL (Fig. 4.8a) and NoAf (Fig. 4.8b) experiments, we see that in the absence of the African topography air particles can indeed flow past Africa and move into the Indian region. Also, in our simulations, the zonal wind does increase near the region in which topography is removed and over the equatorial Indian Ocean (Fig. 4.4b). This suggests that indeed the African topography blocks air from Africa and weakens the westerlies. However, the stronger zonal wind does not extend into the Arabian Sea, to the west of the Indian subcontinent, where the precipitation response to the topography removal is the largest. After further decomposing the horizontal convergence in the dynamic convergence term into zonal and meridional components in the moisture budget (Eq. (4.1)), we find that the enhanced precipitation results primarily from increased meridional wind convergence, rather than stronger zonal wind convergence as proposed by Chakraborty et al. (2009) (Fig. 4.7e and f). This stronger meridional moisture convergence is associated with the development of a larger-scale cyclonic circulation anomaly over the Arabian Sea (Fig. 4.5b). Mechanisms driving this cyclonic anomaly are explored more in detail in the next section.

4.4 Impact of the African Topography on the Larger-scale Circulation

Stationary wave pattern

The cyclonic anomaly developing over the Arabian Sea in response to the removal of the African topography and the anticyclonic anomalies in its upstream and down-

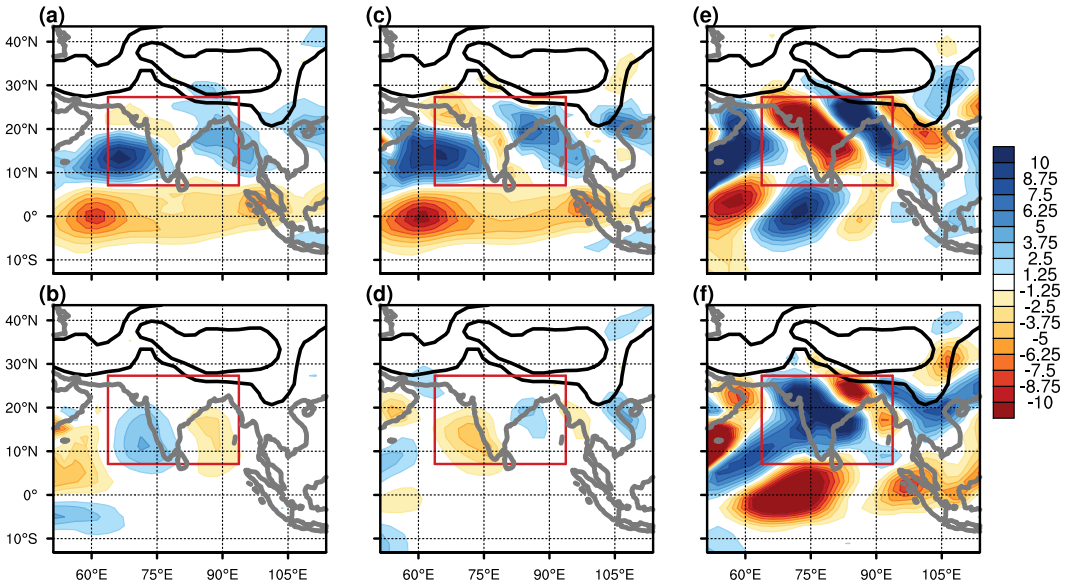

Figure 4.7: Anomalous (NoAf - CTL) JJA-average moisture budget: (a) anomalous precipitation; (b) thermodynamic component, (c) convergence and (d) advection term of the dynamic component, (e) zonal and (f) meridional dynamic convergence term (mm day^{-1}). Thick black lines indicate the surface pressure in CTL (from 900 hPa to 700 hPa, with interval of 200 hPa), indicating the location of topography.

stream are indicative of a wave-like pattern. A similar wave-like pattern is also seen in the simulations of Slingo et al. (2005), who suggest a possible link between the stationary wave response to the African topography and changes in the SAM precipitation as the topography is removed. This stationary wave pattern can be qualitatively understood as a direct response to the weakening of the cross-equatorial meridional flow as topography is removed: a weakening of the cross-equatorial southerly wind at its core along the coast of Africa at around 8^{o}N and 50^{o}E would be accompanied by cyclonic anomalies to its east at around 50 - 70^{o}E and anticyclonic anomalies to its west at around 40 - 50^{o}E, consistent with what is seen in our simulations (Fig. 4.9a). However, as already extensively discussed in RH95, a full consideration of the PV budget can provide a quantitative understanding of the flow properties and PV dynamics in the downstream of the cross-equatorial meridional flow. In the following subsection, we present PV budget analyses following trajectories to develop a more mechanistic understanding of the cyclonic anomaly over the Arabian Sea in the NoAf experiment.

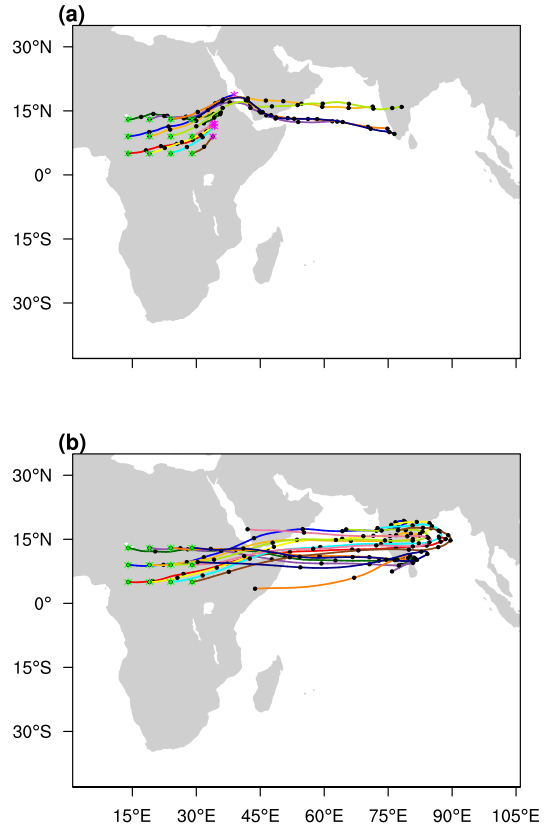

Figure 4.8: Forward trajectory analysis for the (a) CTL and (b) NoAf experiments. The green asterisks are the integration-starting points and different colors indicate different integration-starting locations. Particles are chosen to originate from the 850-hPa level.

PV dynamics of the Somali jet and its relation with the SAM precipitation

As discussed in detail in the previous subsection and as shown in Fig. 4.9a, a cyclonic circulation anomaly (i.e., the difference between the NoAf and CTL experiments) exists to the west of India over the Arabian Sea. A region of positive PV anomaly is also located there. In Section 3, we have shown how, as topography is removed, precipitation increases mainly over the ocean just west of the Indian subcontinent (Fig. 4.5b), primarily in association with anomalous meridional wind convergence (Fig. 4.7f). The increased meridional wind convergence is colocated and related to the southerly flow on the eastern flank of the cyclonic anomaly over the Arabian sea (Fig. 4.9a). To better highlight the possible relationship between the cyclonic anomaly and the precipitation response, in Fig. 4.10, we decompose the anomalous total wind into its rotational and divergent components at two levels at the top (850 hPa) and within (900 hPa) the boundary layer. At the higher level, the anomalous wind is clearly dominated by the rotational component, with the divergent compo-

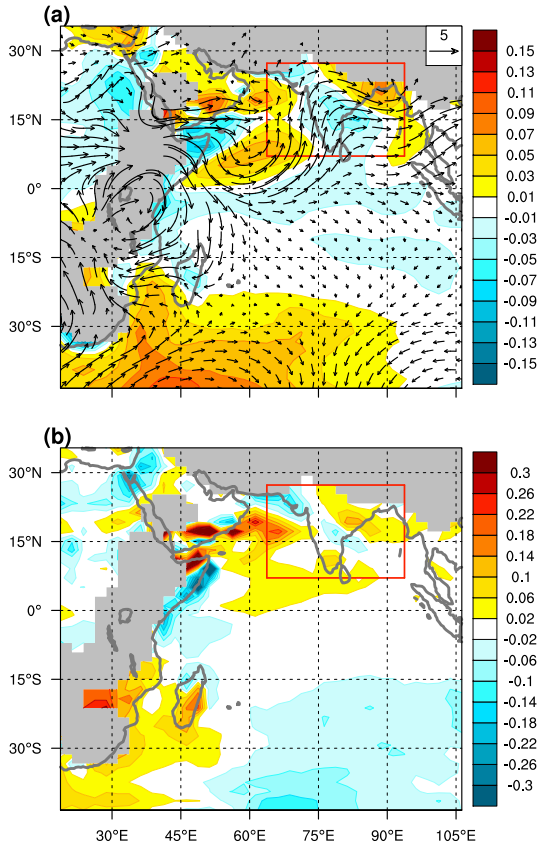

Figure 4.9: (a) Anomalous (NoAf - CTL) JJA-average PV (shading, PV unit, PVU, 10^{-6} K m^2 kg^{-1} s^{-1}) and 850-hPa winds (vectors, m s^{-1}). (b) Anomalous material PV tendency (PVU day^{-1}). The gray shading indicates regions with no data below 850 hPa.

nent becoming more dominant as the surface is approached. Despite these vertical changes, two features are seen at both heights: 1) the wave-like pattern downstream of the African topography is evident at all levels in the anomalous rotational flow; and 2) the anomalous convergence, which is directly linked to and influenced by the anomalous enhanced precipitation over the Arabian Sea, is approximately colocated with the enhanced southerly wind on the eastern flank of the anomalous cyclone. Here we speculate that the cyclonic anomaly in the rotational component is a direct response to the topography removal. Close to the surface, this rotational response is modified by surface friction and its spatial changes, as the southerly flow approaches the Indian subcontinent, which creates a region of strong meridional wind convergence and enhanced precipitation (Fig. 4.7).

Therefore, in the following, we focus on understanding dynamical mechanisms responsible for the anomalous rotational component, namely the lower-level anoma-

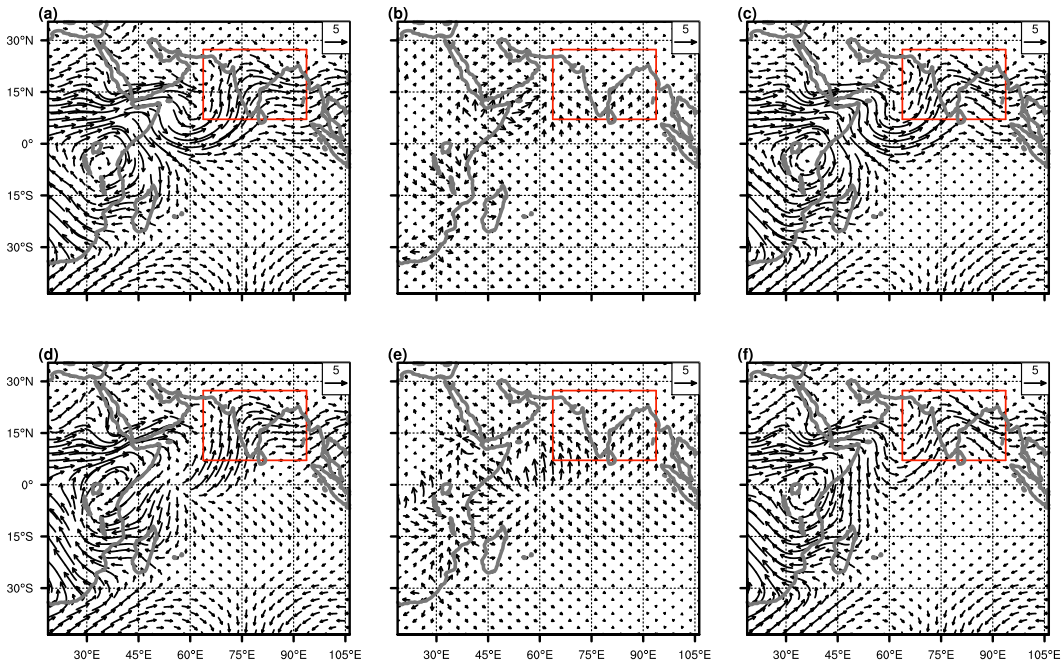

Figure 4.10: Anomalous (a, d) total, (b, e) divergent, and (c, f) rotational winds at $\sim$ 850 and 900 hPa, respectively. Please note that these analyses are conducted on hybrid model coordinates.

lous cyclone over the Arabian Sea, and we focus on the 850-hPa level, where this component has strongest anomalies within the boundary layer. In order to do so, we consider the full PV dynamics, which includes its sources and sinks, and perform a detailed analysis of its budget. Please note that results would not change, at least qualitatively, if we considered a moisture weighted vertical average (more closely linked to the moisture budget) within the boundary layer.

Ertel's PV, $\frac{1}{\rho}(\boldsymbol{\eta} \cdot \nabla\theta)$, is a scalar quantity that expresses both the rotational and stratification features of the fluid. Here, $\boldsymbol{\eta}$ is the 3D absolute vorticity vector, θ the potential temperature, and ρ the density of the fluid. In z-coordinate, the PV budget is:

$$\frac{D(PV)}{Dt} = \frac{1}{\rho}\boldsymbol{F}_\eta \cdot \nabla\theta + \frac{1}{\rho}\boldsymbol{\eta} \cdot \nabla\dot{\theta}, \tag{4.2}$$

where $\boldsymbol{F}_\eta$ is the curl of the 3D frictional forcing $\boldsymbol{F}$, and $\dot{\theta}$ is the heating rate. The first term in the right-hand side of Eq. (4.2) is the frictional term and the second term is the heating term. This conservation law clearly highlights how PV is materially conserved in the absence of friction and diabatic heating.

RH95 used the PV budget to analyze the dynamics of the Somali cross-equatorial

flow. They argued that the change in sign of planetary rotation at the equator would prevent cross-equatorial flow in a stratified fluid, so much so that PV material tendencies are necessary for cross-equatorial flow to be achieved. Particles that retain their negative PV over the Arabian Sea would recirculate back into the SH, with a significant reduction of the moisture flux into the monsoon region. The combination of land-sea contrast in friction, which is enhanced by the African topography, and diabatic heating allows for sufficient positive PV modification and helps maintain the jet in the NH. Removal of topography in their dry model, forced by a prescribed diabatic heating, suggests that without the African topography, PV tendencies would decrease to a point that no significant cross-equatorial flow could be maintained into the Indian monsoon region.

In our simulations, removing the African topography has a significantly less dramatic impact on the cross-equatorial flow than what is discussed in RH95. In fact, the cross-equatorial flow weakens only in its core, close to the region of modified topography. However, we still find significant differences in the lower-level flow, and its curvature, downstream of the topography in the CTL and NoAf experiments. In the NoAf experiment, the flow has a stronger meridional component, with anomalous southerlies, compared to that in the CTL experiment, in which the flow is primarily zonally oriented when approaching the Indian subcontinent. This, as discussed above, has a non-negligible impact on the SAM precipitation. Here, we want to explore if and to what extent these lower-level flow changes can be understood through changes in the PV budget along flow trajectories. To this aim, we perform a PV budget analysis similar to the one done by RH95. One important difference is that in this work we use a full-physics GCM, where diabatic heating is not prescribed but interacts with and depends on the monsoonal circulation. We analyze the overall impact of all terms on the PV budget of the cross-equatorial flow and its downstream extension. In particular, we want to unravel mechanisms responsible for the positive PV anomaly over the Arabian Sea when the African topography is removed.

Fig. 4.9b shows the difference of the JJA mean material PV tendency between the NoAf and CTL experiments at 850 hPa (i.e., the sum of the frictional and heating terms in the PV budget). Please note that changes in the material tendencies at other levels within the boundary layer are of similar magnitude as the ones at 850 hPa (not shown). Caused by the mountain range to the west of the cross-equatorial flow, lateral frictional forces induce positive material PV tendency in the CTL experiment along the particles moving near the African topography. When the

African topography is removed, the frictional tendencies to its east decrease, which explains the negative anomalies there. Positive anomalies in PV tendencies are found over the Arabian Sea, in the same broad region of positive PV anomalies. One might therefore anticipate that larger PV over the Arabian Sea in the NoAf experiment is primarily due to these positive PV tendencies. However, the tendencies shown in Fig. 4.9b are material tendencies, which can be directly linked to PV changes only from a Lagrangian perspective, following particle trajectories. That is to say that to understand PV changes over the Arabian Sea, one also needs to consider where particles reaching this region originated from and passed by. To this aim, we analyze the PV budget along backward trajectories for particles with integration-starting points in the Arabian Sea region with the largest PV anomalies. In so doing, we account for all factors that can potentially influence PV in the target region, from the particle initial locations, and hence initial planetary vorticity, initial relative vorticity, and material tendencies accumulated along specific paths.

The backward trajectory analysis is calculated in both experiments with particles starting from the region that has the largest PV anomaly (Fig. 4.11). The backward trajectories highlight important differences in the flow between the CTL and NoAf experiments: while in the former the cross-equatorial flow is more coherent and organized, with most of the particles in the Arabian Sea originating from similar latitudes in the SH, in the latter particles appear to originate from different latitudes, from the SH Indian Ocean to near equatorial Africa. Interestingly, we find that in both experiments particles undergo significant height variations, which influences the material PV tendencies they experience (Fig. 4.11c, d).

By integrating the material PV tendency along the paths, we can track the anomalous evolution of PV (Fig. 4.12a) and compute the net PV change along the trajectories[1]. At time 0 hr, the PV in the NoAf experiment is larger than that in the CTL experiment for every trajectory (Fig. 4.12a). This is to be expected since we choose the region of positive PV anomaly as our integration-starting region. However, the PV difference at the integration-ending time of our backward calculation (-240 hrs) is even more positive. This implies that the larger PV over the Arabian Sea in the NoAf experiment at time 0 hr are primarily due to larger values in the initial PV. This can also be seen from Fig. 4.13, which shows that the averaged total net PV change is larger in the CTL experiment than in the NoAf experiment. If this were the dominant effect, the PV anomaly over the Arabian Sea would be negative (anticyclonic), rather than

[1]The offset between the real PV evolution and the accumulated PV evolution integrated from the total material PV tendency is small, so we mainly discuss the calculated PV evolution.

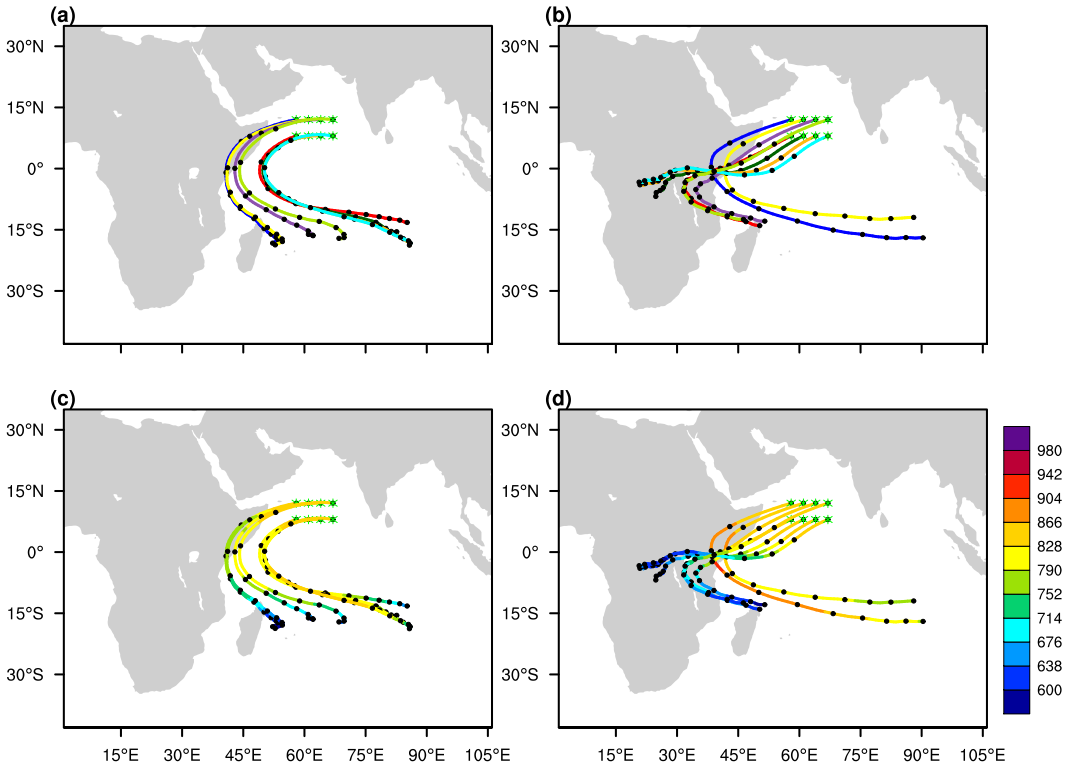

Figure 4.11: Backward trajectories in the (a) CTL and (b) NoAf experiments. The green asterisks mark the integration-starting points and different colors indicate different integration-starting locations. Particles are chosen to originate from the 850-hPa level. The integration-starting time is 8/20. Trajectories in (c) and (d) are the same as in (a) and (b), but the color coding indicates the pressure level (hPa) for each point along the trajectories.

positive (cyclonic). Our results show the opposite, which suggests that the primary difference lies in the initial PV values. More specifically, the positive PV anomaly between the NoAf and CTL experiments over the Arabian Sea is due to the larger (or less negative) initial PV in the NoAf experiment compared to that in the CTL experiment. This is further confirmed in Fig. 4.14, which shows the time evolution of the latitude along the particle trajectories in the CTL and NoAf experiments, and their difference (NoAf-CTL). Because the initial latitudes of the particles are larger (that is, further northward) in the NoAf experiment, the particles contain larger initial planetary vorticity and therefore larger initial PV. Similar conclusions can be reached if particles are chosen to originate from a lower level in the backward trajectory calculations.

Please note that the net PV change along trajectories can also be computed following

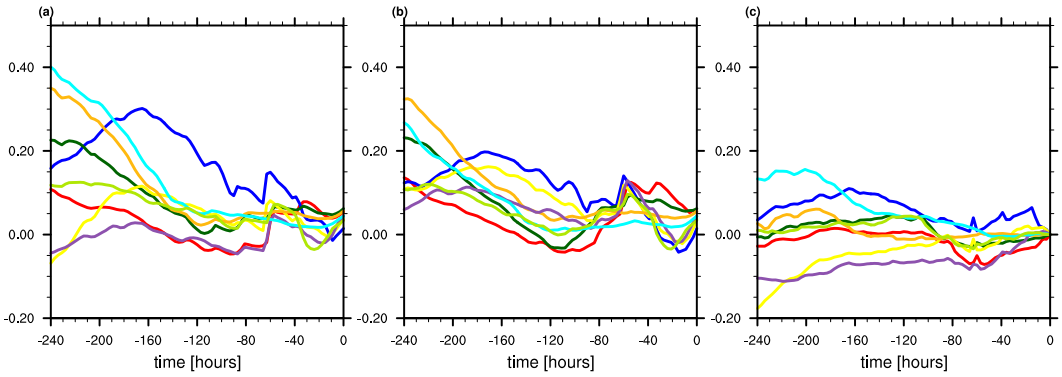

Figure 4.12: Anomalous (NoAf - CTL) evolution of PV (a) calculated by integrating the material PV tendency and (b) interpolated along trajectories, respectively. (c) The residual (difference) between (a) and (b). Different colors indicate different integration-starting locations, consistent with Fig. 4.11a and b.

the actual PV evolution along the paths (Fig. 4.12b). While the PV budget is not completely closed and there exists some residual, the associated error at the beginning of the trajectories is smaller than the difference in initial PV discussed above. Hence, the presence of residuals in the PV budget does not invalidate the main conclusion emerging from our analyses[2].

The significant differences in the latitude of the initial particle locations between CTL and NoAf are consistent with the changes in the simulated flow, discussed in previous sections. In particular, in the NoAf experiment, the weaker blocking effect by the African topography and the weaker cross-equatorial flow close to the African coast allow for some of the particles to originate further west and closer to the equator in the SH than what seen in the CTL run. The particles, therefore, have a larger initial planetary vorticity value: this allows them to reach the Arabian Sea with more positive PV, even if the net material PV tendencies along their trajectories are less positive than the one experienced by particles reaching the same location in the CTL experiment. While individual trajectories shown in Figs. 4.12a and 4.13 somewhat differ in the relative importance of the initial PV and the material PV tendencies in the resulting PV difference at the end point, most of them do highlight the role of the initial PV difference. Also note that results in Figs. 4.12a and 4.13 represent averages for eight different trajectories, and hence emphasize the general pattern emerging from most trajectories.

Order-of-magnitude calculations also show that the vorticity difference implied by

[2]We have also verified that the residual term of the local PV budget (in an Eulerian perspective) is small compared to the material PV tendency (not shown).

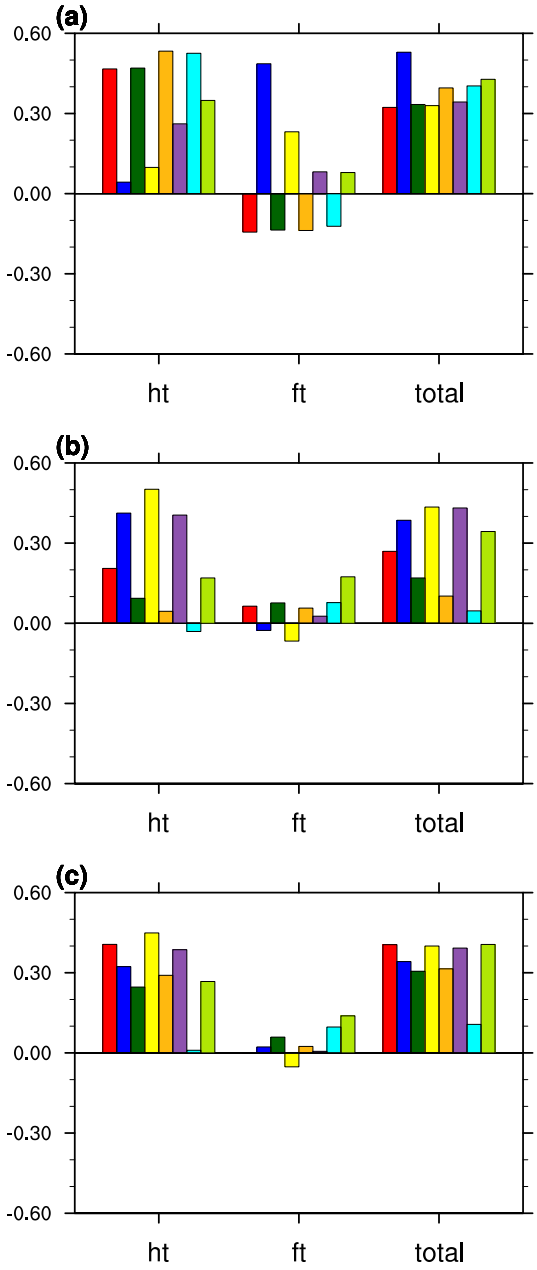

Figure 4.13: Net PV change along the 10-day trajectories for the (a) CTL, (b) NoAf, and (c) NoAfArab experiments. “ht", “ft" and “total" indicate the heating, the frictional and the total (heating + frictional) material PV tendencies, respectively. Different colors indicate different integration-starting locations, consistent with Fig. 4.11a and b.

the initial PV difference seen in the backward trajectories (Fig. 4.12a) and the stratification at those initial locations is of the same order of magnitude as the vorticity difference associated with the differences in starting latitudes in Fig. 4.14c. This allows us to conclude with some confidence that the positive PV anomaly over

the Arabian Sea primarily arises because of differences in the initial location, and hence planetary vorticity, of particles reaching this region in the two experiments. One caveat we want to emphasize here is that we find that the static stability at the beginning of the trajectories (which influences the value of the original PV) is somewhat higher than average values in tropical regions. This could result from either a model's artifact due to limitations in the convection scheme or from the fact that particles originate from a region (15^{o}S) where convection is not active and, therefore, characterized by a larger stability.

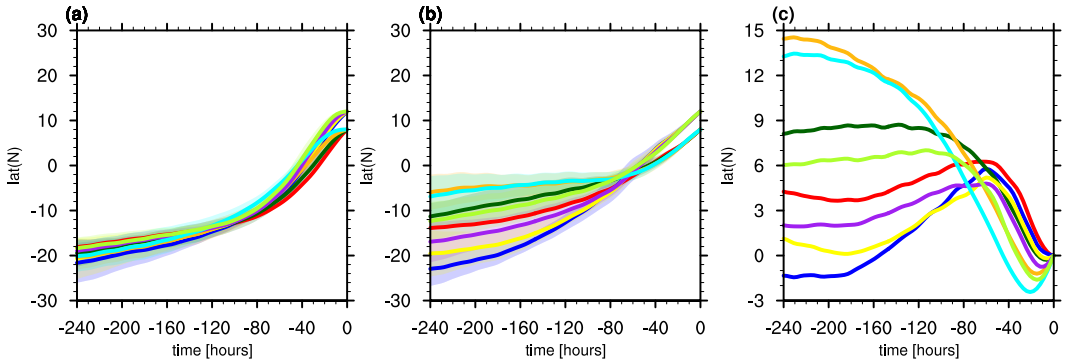

Figure 4.14: Evolution of latitude along the trajectories starting from the same locations as those in Fig. 4.11 for (a) CTL, (b) NoAf and (c) difference between the two (NoAf-CTL). In (a) and (b), the thick lines show the mean and the shading shows the spread (2 standard deviations) in the eight trajectories with eight different integration-starting times.

4.5 The Influence of the Arabian Topography

Although our main goal is to focus on the impact of the African topography on the SAM, the Arabian topography is located right to the west of the Indian subcontinent and can be thought of as providing an extension to the African topography. This prompts us to examine further changes in the SAM when the Arabian topography is also removed (Fig. 4.1c). In the simulation when both African and Arabian topography are removed (NoAfArab), the precipitation in the larger-scale SAM domain increases relative to the CTL experiment (Fig. 4.5a and c), but decreases slightly relative to the NoAf experiment, primarily in the northwestern portion of the Indian region (Fig. 4.15a). A moisture budget analysis (Eq. (4.1)) reveals that this precipitation decrease is associated with a reduction in the dynamic convergence term (Fig. 4.15).

While the PV anomaly over the Arabian Sea is stronger in the NoAfArab experiment than in the NoAf experiment (Figs. 4.9 and 4.16), the precipitation response has

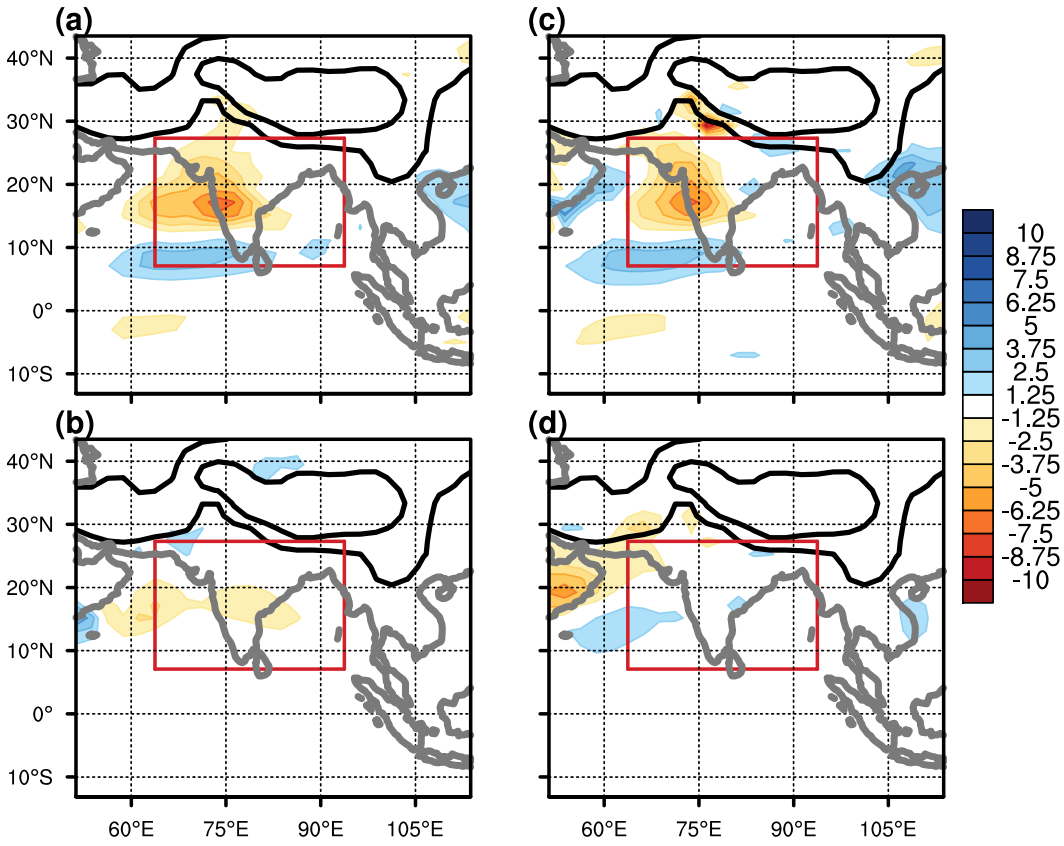

Figure 4.15: Same as Fig. 4.7a–d, but for the difference between the NoAfArab and NoAf experiments.

opposite sign (Fig. 4.15a). That is, the precipitation increase relative to the CTL run on the eastern flank of the cyclonic anomaly over the Arabian Sea is smaller when both the Arabian and African topography are removed than when the African topography is removed in isolation. This appears to be due to the fact that the southerly flow on the eastern flank of the stronger PV anomaly, associated with anomalous meridional convergence relative to the CTL experiment, does not increase in the NoAfArab experiment relative to the NoAf experiment. This can occur because PV is not only influenced by the absolute vorticity, but also by the atmospheric stability. Changes in the latter can induce changes in the PV field, without changes in the absolute vorticity. Additionally, changes in relative vorticity are not necessarily correlated to changes in the southerly flow on the eastern flank of the PV positive anomaly. Therefore, the small changes in PV between the NoAf and NoAfArab experiments are not easily related to wind circulation patterns, and associated precipitation changes, near the Indian region. This highlights the complexity of the circulation response to changes in topography in a full physics GCM.

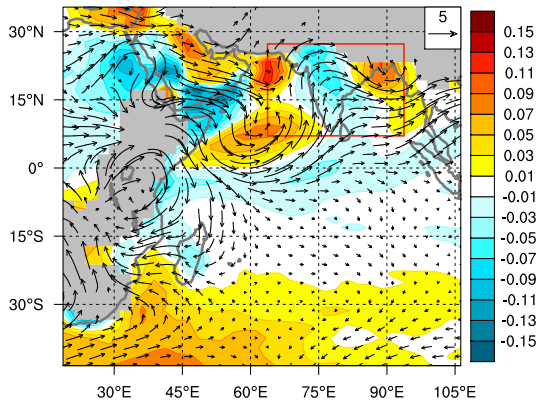

Figure 4.16: Same as Fig. 4.9a, but for the PV difference between the NoAfArab and CTL experiments.

Despite not necessarily providing a direct link to understanding precipitation changes, it is still of interest to analyze mechanisms behind the PV increase over the Arabian Sea when the Arabian topography is removed. Therefore, we compute the PV budget following particle trajectories. The backward trajectories are similar to the ones in the NoAf experiment (not shown). The difference in the initial particle location, which was critical in explaining differences between the NoAf and CTL experiments, does not play a significant role here. This means that removing the Arabian topography does not modify substantially the trajectories of particles that reach the Arabian Sea in the region of largest PV anomaly. This suggests that accumulated PV material tendencies have to be larger in the NoAfArab experiment than in the NoAf one, to explain the positive PV anomaly between the two experiments. This is confirmed in Fig. 4.13c, which also shows that the larger material PV modification arises from the larger heating term, rather than changes in the frictional term.

In summary, these results show how the Arabian topography has a relative small impact on the SAM precipitation response and only slightly modifies the response to the removal of the African topography. This might be due to the smaller height and range of this topographical feature, as well as its location: being further north than the African topography, the Arabian topography likely has a smaller interaction with the cross-equatorial flow.

4.6 Conclusions

The precise role that the African topography plays in the structure and intensity of the SAM cross-equatorial flow and the precipitation still remains debated. While it is widely accepted in the literature that the African topography helps to spatially

confine the cross-equatorial flow and to enhance the SAM precipitation, recent studies show how the SAM precipitation increases rather than decreasing in numerical experiments when the African topography is removed. Here, we perform similar GCM experiments with modified topography and we provide a more comprehensive and quantitative discussion of the impact of the topography on the monsoonal lower-level flow and precipitation.

In simulations with a full-physics GCM, when the African topography is removed, the SAM precipitation increases even if the cross-equatorial flow weakens. We find that in the absence of the blocking effect of the African topography, westerly winds strengthen over the eastern African coast. Previous studies attributed the precipitation increase in the absence of the African topography to the strengthening of the westerly winds, and associated moisture convergence, as the zonal flow approaches the Indian subcontinent. In our simulations, however, enhanced westerlies do not extend over the Arabian Sea, and stronger precipitation arises because of stronger meridional, rather than zonal, convergence. This enhanced meridional convergence is in turn associated with anomalous southerly flow on the eastern flank of a cyclonic wind, or positive PV, anomaly over the Arabian Sea.

PV budget analyses along particle trajectories are being conducted, to explain mechanisms giving rise to this cyclonic, or positive PV, anomaly. It is shown that particles over the Arabian Sea have higher PV in the NoAf experiment relative to those in the CTL experiment not because they experience more positive material PV tendencies along their paths, but rather because they tend to originate from higher latitudes, and therefore carry with them higher values of initial planetary vorticity. Weaker cross-equatorial flow and weaker blocking effect (i.e., stronger westerly wind) in the absence of the African topography allow for particles originating from near equatorial Africa or over the near equatorial SH Indian Ocean to reach the monsoon region. Because of the larger PV, the flow over the Arabian Sea has a stronger southerly component to the west of India, and associated with it, stronger moisture convergence and precipitation in the NoAf experiment.

We also conduct and discuss an experiment where the Arabian topography is removed in addition to the African topography. Despite inducing interesting and non-intuitive changes in the circulation and precipitation fields, the Arabian topography is found to have only a very modest influence on the monsoon, consistent with its smaller extent, height and northward position relative to the African topography.

In our simulations, we do not consider the ocean response to the circulation changes,

in that SSTs are kept fixed and the same in all experiments. The ocean-atmosphere coupling can have important impacts on the mechanisms here discussed. For instance, the reduction of the cross-equatorial flow as the African topography is removed would reduce upwelling and increase SSTs. Similarly, changes in wind strength could induce further SST changes through evaporation, which in turn would influence the precipitation response. These effects will be explored in future studies with experiments in a slab-ocean or fully coupled GCM. The sensitivity of our results to changes in model physics and horizontal resolution is also not explored in this study. However, similar experiments conducted with different GCMs (Chakraborty et al., 2002, 2006, 2009; Slingo et al., 2005) show responses in the SAM precipitation and circulation patterns that are in qualitative, if not quantitative, agreement with the ones reported here. This suggests that the large-scale features that are the focus of our study are not an artifact of the model physics and configuration, and have some generality.

Unlike more idealized work, which has attempted to consider the impact of topography and diabatic heating in isolation on the monsoonal flow, here we use a comprehensive GCM, where the distribution of diabatic heating is itself part of the response and dependent on the monsoonal circulation. Therefore, as the lower boundary is modified (here through changes in topography) the precipitation distribution can respond in ways not predicted by more idealized studies. As the topography is removed, changes in the resulting circulation will induce changes in the diabatic heating, which in turn will affect the PV of the monsoonal cross-equatorial flow and larger-scale circulation. While making causality harder to assess, this approach has the advantage of being energetically and dynamically consistent. In particular, it allows us to show how the Indian monsoon is significantly less sensitive to the presence of the African topography and a topographically confined Somali jet than what is commonly thought: in fact, while having a quantitative impact on the structure of the Somali jet, the removal of the African topography does not modify in any significant way any of the major features of the simulated SAM, such as its position, strength and seasonality.

In this respect, this work is consistent with emerging theories of monsoons, which view these tropical circulations as regional manifestations of the seasonal cycle of the tropical Hadley circulation (e.g., Bordoni and Schneider, 2008; Gadgil, 2003) rather than large-scale sea-breeze circulations driven by local forcing. By shedding insight into the response of the SAM to modified topography, and resulting flow –

precipitation interactions, this study might help to better constrain the influence of radiative and land surface forcing on the monsoon on different time scales.

Chapter 5

CONCLUSIONS

The oceanic Intertropical Convergence Zone (ITCZ) and its seasonal excursions into summertime tropical and subtropical land masses in association with monsoons are among the largest scale features of the tropical climate. Tropical and subtropical regions with increasing populations and rapidly growing economies heavily rely on rainfall and are extremely susceptible to climate change. Yet, what fundamentally controls the spatial and temporal distribution of tropical precipitation remains an open question and a major challenge in the climate sciences. This dissertation explores the dynamics of seasonally-migrating global and local convergence zones in both model simulations with different complexity and observations within the perspective of different theoretical frameworks.

We begin in Chapter 2 by exploring to what extent the energetic framework, which has been used extensively in the past decade for understanding the annual and zonal mean ITCZ position and shifts (e.g., Bischoff and Schneider, 2014; Donohoe et al., 2013; Frierson and Hwang, 2012; Kang et al., 2009, 2008), can also provide insight into ITCZ migrations on seasonal and shorter timescales in idealized aquaplanet simulations with different mixed layer depths. In all simulations, the ITCZ always trails the energy flux equator (EFE), with the lag increasing with increasing mixed layer depth. While the EFE evolves almost in phase with the insolation forcing and reflects the hemispheric asymmetry in atmospheric net energy input, the ITCZ is more strongly controlled by surface thermodynamics (e.g., temperature and moist static energy, MSE), which cannot evolve as rapidly.

One important consequence of the lead-lag relationship between the EFE and the ITCZ is that these two quantities can reside in opposite hemispheres, with ITCZ shifts during the seasonal cycle not being explained by shifts in the EFE and not being simply anti-correlated with the cross-equatorial energy transport. This happens as the winter cross-equatorial Hadley circulation retreating from the summer hemisphere develops negative gross moist stability, hence transporting energy in the direction of the lower branch. At these times, the winter cell is much weaker than it is when expanding into the summer hemisphere and develops a shallow return flow where the MSE reaches its minimum. The asymmetry in structure and GMS of the

winter cell in its expanding and retreating phases is essential for the existence of the lag between the EFE and the ITCZ and in turn appears to be related to an asymmetry in the near surface temperature evolution.

The lead-lag relationship between the EFE and the ITCZ seen in the idealized simulations might have the potential to provide the basis for predictions of seasonal ITCZ migrations. However, more work needs to be done to explain the sensitivity of the lag to different model physics and other processes that might play a quantitative role in the EFE-ITCZ relation in different ocean basins.

In Chapter 3, we use MERRA-2 reanalysis data to examine the relation between the ITCZ position, overturning circulation vertical structure, and the associated energetics in the observed climate system. We show that, similarly to what is seen in the idealized simulations discussed in Chapter 2, the EFE and the ITCZ are not collocated within the seasonal cycle and feature a high degree of zonal asymmetries.

In the zonal mean, while the EFE is in the two hemispheres for almost equal amounts of time, the ITCZ is located in the NH for a large portion of the seasonal cycle. Because the ITCZ evolves differently from an annual harmonic, the temporal relationship between the EFE and the ITCZ cannot simply be described as a lag. However, there exists a clear offset between these two quantities, which is particularly evident in boreal fall, during which time the EFE moves to the SH while the ITCZ remains north of the equator. At these times, the overturning circulation needs to transport energy northward across the equator, despite a northward displaced ascending branch. This is achieved through the development of a bottom heavy (and weak) southern Hadley cell, that transports MSE in the direction of its lower branch.

In the Eastern Pacific, as documented by previous studies, the ITCZ remains north of the equator almost throughout the year, with the exception of boreal spring, when a double ITCZ develops. The seasonal relationship between the EFE and the ITCZ in this sector is complicated by the appearance of a bifurcation in the EFE (that is, the existence of two nodes in the energy transport) during boreal fall and spring. Here we show that during these times the cross-equatorial cell, which has a shallow return flow persisting throughout the year (e.g., Back and Bretherton, 2006; Zhang et al., 2004), becomes even more bottom heavy, again corresponding to a negative GMS and energy transport in the direction of the lower-level flow. As argued by previous studies (e.g., Back and Bretherton, 2009a; Lindzen and Nigam, 1987; Sobel, 2007), the degree of bottom heaviness of the circulation seems to be controlled by the strength of the SST Laplacian below the ITCZ.

Finally, in Chapter 4, we focus on the summertime convergence zone associated with the South Asian monsoon and we explore associated changes in response to the removal of the African topography in a full physics GCM (AM2.1). Previous studies had in fact argued that the East African Highlands (EAHs) act as a wall to accelerate and spatially concentrate the Somali jet, hence potentially strengthening moisture transport and precipitation in the monsoon region (e.g., Anderson, 1976; Findlater, 1969; Halpern and Woiceshyn, 2001; Krishnamurti et al., 1976; Paegle and Geisler, 1986; Rodwell and Hoskins, 1995; Sashegyi and Geisler, 1987). In AM2.1, as the African topography is removed, the Somali jet indeed weakens as expected; the monsoonal precipitation over India however increases slightly. This precipitation increase is associated with the development of a cyclonic low-level wind anomaly over the Arabian Sea, and associated anomalous meridional moisture flux convergence over India. Potential vorticity (PV) budget analyses along particle trajectories show that this cyclonic anomaly does not arise from changes in PV material tendencies, but from changes in the originating latitudes of particles that reach India. More specifically, in the absence of the blocking effect by the African topography and with weaker cross-equatorial flow, air particles originate from higher latitudes with larger background planetary vorticity and hence larger PV.

BIBLIOGRAPHY

Adam, O., Bischoff, T., and Schneider, T. (2016a). Seasonal and Interannual Variations of the Energy Flux Equator and ITCZ. Part I: Zonally Averaged ITCZ Position. *J Climate*, 29(9):3219–3230.

Adam, O., Bischoff, T., and Schneider, T. (2016b). Seasonal and Interannual Variations of the Energy Flux Equator and ITCZ. Part II: Zonally Varying Shifts of the ITCZ. *J Climate*, 29(20):7281–7293.

Adler, R. F., Huffman, G. J., Chang, A., Ferraro, R., Xie, P.-P., Janowiak, J., Rudolf, B., Schneider, U., Curtis, S., Bolvin, D., Gruber, A., Susskind, J., Arkin, P., and Nelkin, E. (2003). The Version-2 Global Precipitation Climatology Project (GPCP) Monthly Precipitation Analysis (1979–Present). *J. Hydrometeor.*, 4(6):1147–1167.

An, Z., Kutzbach, J. E., Prell, W. L., and Porter, S. C. (2001). Evolution of Asian monsoons and phased uplift of the Himalaya–Tibetan plateau since Late Miocene times. *Nature*, 411:62–66.

Anderson, D. L. T. (1976). The low-level jet as a western boundary current. *Mon. Wea. Rev.*, 104(7):907–921.

Anderson, J., Balaji, V., Broccoli, A., Cooke, W., Delworth, T., Dixon, K., Donner, L., Dunne, K., Freidenreich, S., Garner, S., et al. (2004). The new GFDL global atmosphere and land model AM2–LM2: Evaluation with prescribed SST simulations. *J. Climate*, 17(24):4641–4673.

Arbuszewski, J. A., deMenocal, P. B., Cléroux, C., Bradtmiller, L., and Mix, A. (2013). Meridional shifts of the Atlantic intertropical convergence zone since the Last Glacial Maximum. *Nature Geoscience*, 6(11):959–962.

Back, L. E. and Bretherton, C. S. (2006). Geographic variability in the export of moist static energy and vertical motion profiles in the tropical Pacific. *Geophysical Research Letters*, 33(17):392.

Back, L. E. and Bretherton, C. S. (2009a). A Simple Model of Climatological Rainfall and Vertical Motion Patterns over the Tropical Oceans. *J Climate*, 22(23):6477–6497.

Back, L. E. and Bretherton, C. S. (2009b). On the Relationship between SST Gradients, Boundary Layer Winds, and Convergence over the Tropical Oceans. *J Climate*, 22(15):4182–4196.

Bischoff, T. and Schneider, T. (2014). Energetic Constraints on the Position of the Intertropical Convergence Zone. *J Climate*, 27(13):4937–4951.

Bischoff, T. and Schneider, T. (2016). The Equatorial Energy Balance, ITCZ Position, and Double-ITCZ Bifurcations. *J Climate*, 29(8):2997–3013.

Blanford, H. F. et al. (1884). Ii. on the connexion of the himalaya snowfall with dry winds and seasons of drought in india. *Proceedings of the Royal Society of London*, 37(232-234):3–22.

Boos, W. R. and Emanuel, K. A. (2009). Annual intensification of the Somali jet in a quasi-equilibrium framework: Observational composites. *Quart. J. Roy. Meteor. Soc.*, 135(639):319–335.

Boos, W. R. and Hurley, J. V. (2013). Thermodynamic bias in the multimodel mean boreal summer monsoon. *Journal of Climate*, 26(7):2279–2287.

Boos, W. R. and Kuang, Z. (2010). Dominant control of the south asian monsoon by orographic insulation versus plateau heating. *Nature*, 463(7278):218–222.

Boos, W. R. and Kuang, Z. (2013). Sensitivity of the South Asian monsoon to elevated and non-elevated heating. *Scientific Reports*.

Bordoni, S. and Schneider, T. (2008). Monsoons as eddy-mediated regime transitions of the tropical overturning circulation. *Nature Geoscience*, 1(8):515–519.

Bosilovich, M., Akella, S., Coy, L., Cullather, R., Draper, C., Gelaro, R., Kovach, R., Liu, Q., Molod, A., Norris, P., Wargan, K., Chao, W., Reichle, R., Takacs, L., Vikhliaev, Y., Bloom, S., Collow, A., Firth, S., Labow, G., Partyka, G., Pawson, S., Reale, O., Schubert, S. D., and Suarez, M. (2015). MERRA-2 : Initial Evaluation of the Climate. *NASA Tech. Rep. Ser. Glob. Model. Data Assim.*

Broccoli, A. J., Dahl, K. A., and Stouffer, R. J. (2006). Response of the ITCZ to Northern Hemisphere cooling. *Geophysical Research Letters*, 33(1):n/a–n/a.

Chakraborty, A., Nanjundiah, R. S., and Srinivasan, J. (2002). Role of Asian and African orography in Indian summer monsoon. *Geophys. Res. Lett.*, 29(20):1989.

Chakraborty, A., Nanjundiah, R. S., and Srinivasan, J. (2006). Theoretical aspects of the onset of Indian summer monsoon from perturbed orography simulations in a GCM. *Annales Geophysicae*, 24(8):2075–2089.

Chakraborty, A., Nanjundiah, R. S., and Srinivasan, J. (2009). Impact of African orography and the Indian summer monsoon on the low-level Somali jet. *Int. J. Climatol.*, 29(7):983–992.

Chen, J. and Bordoni, S. (2014). Orographic Effects of the Tibetan Plateau on the East Asian Summer Monsoon: An Energetic Perspective. *J Climate*, 27(8):3052–3072.

Chiang, J. C. H., Biasutti, M., and Battisti, D. S. (2003). Sensitivity of the Atlantic Intertropical Convergence Zone to Last Glacial Maximum boundary conditions. *Paleoceanography*, 18(4):n/a–n/a.

Chiang, J. C. H. and Friedman, A. R. (2012). Extratropical Cooling, Interhemispheric Thermal Gradients, and Tropical Climate Change. *Annual Review of Earth and Planetary Sciences*, 40(1):383–412.

Chou, C. and Neelin, J. D. (2003). Mechanisms Limiting the Northward Extent of the Northern Summer Monsoons over North America, Asia, and Africa*. *J Climate*, 16(3):406–425.

Chou, C., Neelin, J. D., and Su, H. (2001). Ocean−atmosphere−land feedbacks in an idealized monsoon. *Quarterly Journal of the Royal Meteorological Society*, 127(576):1869–1891.

Clement, A. C., Hall, A., and Broccoli, A. J. (2004). The importance of precessional signals in the tropical climate. *Climate Dyn.*, 22(4):327–341.

Cronin, T. W. and Emanuel, K. A. (2013). The climate time scale in the approach to radiative-convective equilibrium. *Journal of Advances in Modeling Earth Systems*, 5(4):843–849.

Donohoe, A., Marshall, J., Ferreira, D., Armour, K., and Mcgee, D. (2014). The Interannual Variability of Tropical Precipitation and Interhemispheric Energy Transport. *J Climate*, 27(9):3377–3392.

Donohoe, A., Marshall, J., Ferreira, D., and Mcgee, D. (2013). The Relationship between ITCZ Location and Cross-Equatorial Atmospheric Heat Transport: From the Seasonal Cycle to the Last Glacial Maximum. *J Climate*, 26(11):3597–3618.

Dwyer, J. G., Biasutti, M., and Sobel, A. H. (2012). Projected Changes in the Seasonal Cycle of Surface Temperature. *J Climate*, 25(18):6359–6374.

Emanuel, K. A. (1995). On Thermally Direct Circulations in Moist Atmospheres. *Journal of the Atmospheric Sciences*, 52(9):1529–1534.

Faulk, S., Mitchell, J., and Bordoni, S. (2017). Effects of Rotation Rate and Seasonal Forcing on the ITCZ Extent in Planetary Atmospheres. *Journal of the Atmospheric Sciences*, 74(3):665–678.

Feldl, N. and Bordoni, S. (2016). Characterizing the Hadley Circulation Response through Regional Climate Feedbacks. *J Climate*, 29(2):613–622.

Feldl, N., Bordoni, S., and Merlis, T. M. (2017). Coupled High-Latitude Climate Feedbacks and Their Impact on Atmospheric Heat Transport. *J Climate*, 30(1):189–201.

Findlater, J. (1969). A major low-level air current near the Indian Ocean during the northern summer. *Quart. J. Roy. Meteor. Soc.*, 95(404):362–380.

Flohn, H. (1957). Large-scale aspects of the “summer monsoon" in south and east Asia. *J. Meteor. Soc. Japan*, 75:180–186.

Frierson, D. M. W. (2007). The Dynamics of Idealized Convection Schemes and Their Effect on the Zonally Averaged Tropical Circulation. *Journal of the Atmospheric Sciences*, 64(6):1959–1976.

Frierson, D. M. W., HELD, I. M., and Zurita-Gotor, P. (2006). A Gray-Radiation Aquaplanet Moist GCM. Part I: Static Stability and Eddy Scale. *Journal of the Atmospheric Sciences*, 63(10):2548–2566.

Frierson, D. M. W., HELD, I. M., and Zurita-Gotor, P. (2007). A Gray-Radiation Aquaplanet Moist GCM. Part II: Energy Transports in Altered Climates. *Journal of the Atmospheric Sciences*, 64(5):1680–1693.

Frierson, D. M. W. and Hwang, Y.-T. (2012). Extratropical Influence on ITCZ Shifts in Slab Ocean Simulations of Global Warming. *J Climate*, 25(2):720–733.

Frierson, D. M. W., Hwang, Y.-T., Fučkar, N. S., Seager, R., Kang, S. M., Donohoe, A., Maroon, E. A., Liu, X., and Battisti, D. S. (2013). Contribution of ocean overturning circulation to tropical rainfall peak in the Northern Hemisphere. *Nature Geoscience*, 6(10):1–5.

Gadgil, S. (2003). The Indian monsoon and its variability. *Annu. Rev. Earth Planet. Sci.*, 31(1):429–467.

Green, B. and Marshall, J. (2017). Coupling of Trade Winds with Ocean Circulation Damps ITCZ Shifts. *J Climate*, 30(12):4395–4411.

Halpern, D. and Woiceshyn, P. M. (2001). Somali jet in the Arabian Sea, El Nino, and India rainfall. *J. Climate*, 14(3):434–441.

Haug, G. H. (2001). Southward Migration of the Intertropical Convergence Zone Through the Holocene. *Science*, 293(5533):1304–1308.

Hawcroft, M., Haywood, J. M., Collins, M., Jones, A., Jones, A. C., and Stephens, G. (2016). Southern Ocean albedo, inter-hemispheric energy transports and the double ITCZ: global impacts of biases in a coupled model. *Climate Dynamics*, 48(7-8):2279–2295.

Held, I. M. and Soden, B. J. (2006). Robust responses of the hydrological cycle to global warming. *J. Climate*, 19(21):5686–5699.

Hill, S. A., Ming, Y., and HELD, I. M. (2015). Mechanisms of Forced Tropical Meridional Energy Flux Change. *J Climate*, 28(5):1725–1742.

Hoskins, B. J. and Rodwell, M. J. (1995). A model of the Asian summer monsoon. Part I: The global scale. *J. Atmos. Sci.*, 52(9):1329–1340.

Hwang, Y.-T., Frierson, D. M. W., and Kang, S. M. (2013). Anthropogenic sulfate aerosol and the southward shift of tropical precipitation in the late 20th century. *Geophysical Research Letters*, 40(11):2845–2850.

Kang, S. M., Frierson, D. M. W., and HELD, I. M. (2009). The Tropical Response to Extratropical Thermal Forcing in an Idealized GCM: The Importance of Radiative Feedbacks and Convective Parameterization. *Journal of the Atmospheric Sciences*, 66(9):2812–2827.

Kang, S. M., HELD, I. M., Frierson, D. M. W., and Zhao, M. (2008). The Response of the ITCZ to Extratropical Thermal Forcing: Idealized Slab-Ocean Experiments with a GCM. *J Climate*, 21(14):3521–3532.

Kaspi, Y. and Schneider, T. (2013). The Role of Stationary Eddies in Shaping Midlatitude Storm Tracks. *Journal of the Atmospheric Sciences*, 70(8):2596–2613.

Krishnamurti, T. N., Molinari, J., and Pan, H. L. (1976). Numerical simulation of the Somali jet. *J. Atmos. Sci.*, 33(12):2350–2362.

Lea, D. W. (2003). Synchroneity of Tropical and High-Latitude Atlantic Temperatures over the Last Glacial Termination. *Science*, 301(5638):1361–1364.

Li, C. and Yanai, M. (1996). The onset and interannual variability of the Asian summer monsoon in relation to land–sea thermal contrast. *J. Climate*, 9(2):358–375.

Lin, J.-L. (2007). The Double-ITCZ Problem in IPCC AR4 Coupled GCMs: Ocean-Atmosphere Feedback Analysis. *J Climate*, 20(18):4497–4525.

Lindzen, R. S. and Hou, A. V. (1988). Hadley circulations for zonally averaged heating centered off the equator. *Journal of the Atmospheric Sciences*, 45(17):2416–2427.

Lindzen, R. S. and Nigam, S. (1987). On the Role of Sea Surface Temperature Gradients in Forcing Low-Level Winds and Convergence in the Tropics. *Journal of the Atmospheric Sciences*, 44(17):2418–2436.

Marshall, J., Donohoe, A., Ferreira, D., and McGee, D. (2013). The ocean's role in setting the mean position of the Inter-Tropical Convergence Zone. *Climate Dynamics*, 42(7-8):1967–1979.

Mcgee, D., Donohoe, A., Marshall, J., and Ferreira, D. (2014). Changes in ITCZ location and cross-equatorial heat transport at the Last Glacial Maximum, Heinrich Stadial 1, and the mid-Holocene. *Earth and Planetary Science Letters*, 390:69–79.

Meehl, G. A. (1994). Coupled land-ocean-atmosphere processes and South Asian monsoon variability. *Science*, 266(5183):263–267.

Merlis, T. M., Schneider, T., Bordoni, S., and Eisenman, I. (2012a). Hadley circulation response to orbital precession. Part I: Aquaplanets. *J. Climate, submitted.*

Merlis, T. M., Schneider, T., Bordoni, S., and Eisenman, I. (2012b). Hadley circulation response to orbital precession. Part II: Subtropical continent. *J Climate*.

Merlis, T. M., Schneider, T., Bordoni, S., and Eisenman, I. (2013). The Tropical Precipitation Response to Orbital Precession. *J Climate*, 26(6):2010–2021.

Molnar, P., Boos, W. R., and Battisti, D. S. (2010). Orographic Controls on Climate and Paleoclimate of Asia: Thermal and Mechanical Roles for the Tibetan Plateau. *Annual Review of Earth and Planetary Sciences*, 38(1):77–102.

Molnar, P., England, P., and Martinod, J. (1993). Mantle dynamics, uplift of the Tibetan Plateau, and the Indian Monsoon. *Reviews of Geophysics*, 31(4):357.

Neelin, J. D. (1997). *The Physics and Parameterization of Moist Atmospheric Convection*, chapter 17: Implications of Convective Quasi-Equilibrium for the Large-Scale Flow, pages 413–446. Kluwer Academic Publishers.

Neelin, J. D. (2007). *The Global Circulation of the Atmosphere*, chapter 10: Moist Dynamics of Tropical Convection Zones in Monsoons, Teleconnections, and Global Warming, pages 267–301. Princeton University Press.

Neelin, J. D. and Held, I. M. (1987). Modeling Tropical Convergence Based on the Moist Static Energy Budget. *Monthly Weather Review*, 115(1):3–12.

Neelin, J. D. and Zeng, N. (2000). A Quasi-Equilibrium Tropical Circulation Model—Formulation*. *Journal of the Atmospheric Sciences*, 57(11):1741–1766.

Nie, J., Boos, W. R., and Kuang, Z. (2010). Observational evaluation of a convective quasi-equilibrium view of monsoons. *J. Climate*, 23(16):4416–4428.

O'Gorman, P. A. and Schneider, T. (2008). The Hydrological Cycle over a Wide Range of Climates Simulated with an Idealized GCM. *Journal of Climate*, 21:3815–3832.

Paegle, J. and Geisler, J. E. (1986). The effect of East African topography on flow driven by zonally symmetric forcing. *J. Atmos. Sci.*, 43(17):1862–1872.

Pauluis, O. (2004). Boundary layer dynamics and cross-equatorial Hadley circulation. *Journal of the Atmospheric Sciences*, 61(10):1161–1173.

Philander, S. G. H., Gu, D., Lambert, G., Li, T., Halpern, D., Lau, N. C., and Pacanowski, R. C. (1996). Why the ITCZ Is Mostly North of the Equator. *J Climate*, 9(12):2958–2972.

Privé, N. C. and Plumb, R. A. (2007a). Monsoon dynamics with interactive forcing. Part I: Axisymmetric studies. *Journal of the Atmospheric Sciences*, 64(5):1417–1430.

Privé, N. C. and Plumb, R. A. (2007b). Monsoon dynamics with interactive forcing. Part II: Impact of eddies and asymmetric geometries. *J. Atmos. Sci.*, 64(5):1431–1442.

Raymond, D. J., Sessions, S. L., Sobel, A. H., and Fuchs, Ž. (2009). The Mechanics of Gross Moist Stability. *Journal of Advances in Modeling Earth Systems*, 1(3):n/a–n/a.

Rienecker, M. M., Suarez, M. J., Gelaro, R., Todling, R., Bacmeister, J., Liu, E., Bosilovich, M. G., Schubert, S. D., Takacs, L., Kim, G.-K., Bloom, S., Chen, J., Collins, D., Conaty, A., da Silva, A., Gu, W., Joiner, J., Koster, R. D., Lucchesi, R., Molod, A., Owens, T., Pawson, S., Pegion, P., Redder, C. R., Reichle, R., Robertson, F. R., Ruddick, A. G., Sienkiewicz, M., and Woollen, J. (2011). MERRA: NASA's Modern-Era Retrospective Analysis for Research and Applications. *J Climate*, 24(14):3624–3648.

Rodwell, M. J. and Hoskins, B. J. (1995). A model of the Asian summer monsoon. Part II: Cross-equatorial flow and PV behavior. *J. Atmos. Sci.*, 52(9):1341–1356.

Sashegyi, K. D. and Geisler, J. E. (1987). A linear model study of cross-equatorial flow forced by summer monsoon heat sources. *J. Atmos. Sci.*, 44(13):1706–1722.

Schneider, T. (2017). Feedback of Atmosphere-Ocean Coupling on Shifts of the Intertropical Convergence Zone. *Geophysical Research Letters*, 44(22):11,644–11,653.

Schneider, T., Bischoff, T., and Haug, G. H. (2014). Migrations and dynamics of the intertropical convergence zone. *Nature*, 513(7516):45.

Schneider, T. and Bordoni, S. (2008). Eddy-Mediated Regime Transitions in the Seasonal Cycle of a Hadley Circulation and Implications for Monsoon Dynamics. *Journal of the Atmospheric Sciences*, 65(3):915–934.

Seo, J., Kang, S. M., and Merlis, T. M. (2017). A model intercomparison of the tropical precipitation response to a CO 2doubling in aquaplanet simulations. *Geophysical Research Letters*, 44(2):993–1000.

Singh, M. S., Kuang, Z., and Tian, Y. (2017). Eddy Influences on the Strength of the Hadley Circulation: Dynamic and Thermodynamic Perspectives. *Journal of the Atmospheric Sciences*, 74(2):467–486.

Slingo, J., Spencer, H., Hoskins, B., Berrisford, P., and Black, E. (2005). The meteorology of the Western Indian Ocean, and the influence of the East African Highlands. *Phil. Trans. Roy. Soc. A*, 363(1826):25–42.

Smith, T. M., Reynolds, R. W., Livezey, R. E., and Stokes, D. C. (1996). Reconstruction of historical sea surface temperatures using empirical orthogonal functions. *J. Climate*, 9(6):1403–1420.

Sobel, A. H. (2007). *The Global Circulation of the Atmosphere*, chapter 8: Simple Models of Ensemble-Averaged Tropical Precipitation and Surface Wind, Given the Sea Surface Temperature, pages 219–251. Princeton University Press.

Sobel, A. H. and Bretherton, C. S. (2000). Modeling Tropical Precipitation in a Single Column. *J Climate*, 13(24):4378–4392.

Sobel, A. H. and Neelin, J. D. (2006). The boundary layer contribution to intertropical convergence zones in the quasi-equilibrium tropical circulation model framework. *Theor. Comput. Fluid Dyn.*, 20(5-6):323–350.

Sobel, A. H., Nilsson, J., and Polvani, L. M. (2001). The Weak Temperature Gradient Approximation and Balanced Tropical Moisture Waves*. *Journal of the Atmospheric Sciences*, 58(23):3650–3665.

Takahashi, K. and Battisti, D. S. (2007). Processes Controlling the Mean Tropical Pacific Precipitation Pattern. Part I: The Andes and the Eastern Pacific ITCZ. *J Climate*, 20(14):3434–3451.

Trenberth, K. E. (1991). Climate Diagnostics from Global Analyses: Conservation of Mass in ECMWF Analyses. *J Climate*, 4(7):707–722.

Trenberth, K. E. and Caron, J. M. (2001). Estimates of Meridional Atmosphere and Ocean Heat Transports. *J Climate*, 14(16):3433–3443.

Vellinga, M. and Wood, R. A. (2002). Global Climatic Impacts of a Collapse of the Atlantic Thermohaline Circulation. *Climatic Change*, 54(3):251–267.

Voigt, A., Biasutti, M., Scheff, J., Bader, J., Bordoni, S., Codron, F., Dixon, R. D., Jonas, J., Kang, S. M., Klingaman, N. P., Leung, R., Lu, J., Mapes, B., Maroon, E. A., McDermid, S., Park, J.-y., Roehrig, R., Rose, B. E. J., Russell, G. L., Seo, J., Toniazzo, T., Wei, H.-H., Yoshimori, M., and Vargas Zeppetello, L. R. (2016). The tropical rain belts with an annual cycle and a continent model intercomparison project: TRACMIP. *Journal of Advances in Modeling Earth Systems*, 8(4):1868–1891.

Waliser, D. E. and Gautier, C. (1993). A Satellite-derived Climatology of the ITCZ. *J Climate*, 6(11):2162–2174.

Waliser, D. E. and Somerville, R. C. J. (1994). Preferred Latitudes of the Intertropical Convergence Zone. *Journal of the Atmospheric Sciences*, 51(12):1619–1639.

Walker, C. C. and Schneider, T. (2005). Response of idealized Hadley circulations to seasonally varying heating. *Geophysical Research Letters*, 32(6):1522.

Walker, C. C. and Schneider, T. (2006). Eddy Influences on Hadley Circulations: Simulations with an Idealized GCM. *Journal of the Atmospheric Sciences*, 63(12):3333–3350.

Walker, J. M., Bordoni, S., and Schneider, T. (2015). Interannual variability in the large-scale dynamics of the South Asian summer monsoon. *J. Climate*, 28(9):3731–3750.

Webster, P. J. (1987). *Monsoons (eds Fein, J. S. and Stephens, P. L.)*. John Wiley : New York.

Wei, H.-H. and Bordoni, S. (2018). Energetic Constraints on the ITCZ Position in Idealized Simulations with a Seasonal Cycle. *Journal of Advances in Modeling Earth Systems*. in press.

Wu, G., Li, W., Guo, H., Liu, H., Xue, J., and Wang, Z. (1997). Sensible heat driven air-pump over the Tibetan Plateau and its impacts on the Asian Summer Monsoon. *Collections on the memory of Zhao Jiuzhang. Chinese Science Press, Beijing*, pages 116–126.

Wu, G., Liu, Y., He, B., Bao, Q., Duan, A., and Jin, F.-F. (2012). Thermal controls on the Asian summer monsoon. *Scientific reports*, 2.

Yeh, T., Lo, S., and Chu, P. (1957). On the heat balance and circulation structure in troposphere over Tibetan Plateau. *Acta Meteor. Sin.*, 28:108–121.

Yoshimori, M. and Broccoli, A. J. (2008). Equilibrium Response of an Atmosphere–Mixed Layer Ocean Model to Different Radiative Forcing Agents: Global and Zonal Mean Response. *J Climate*, 21(17):4399–4423.

Zhang, C. (2001). Double ITCZs. *Journal of Geophysical Research*, 106(D11):11785–11792.

Zhang, C., McGauley, M., and Bond, N. A. (2004). Shallow Meridional Circulation in the Tropical Eastern Pacific. *J Climate*, 17(1):133–139.

Zhang, R. and Delworth, T. L. (2005). Simulated Tropical Response to a Substantial Weakening of the Atlantic Thermohaline Circulation. *J Climate*, 18(12):1853–1860.